Mechanical Characterization of Solid Oxide Fuel Cells and Sealants

Jianping Wei

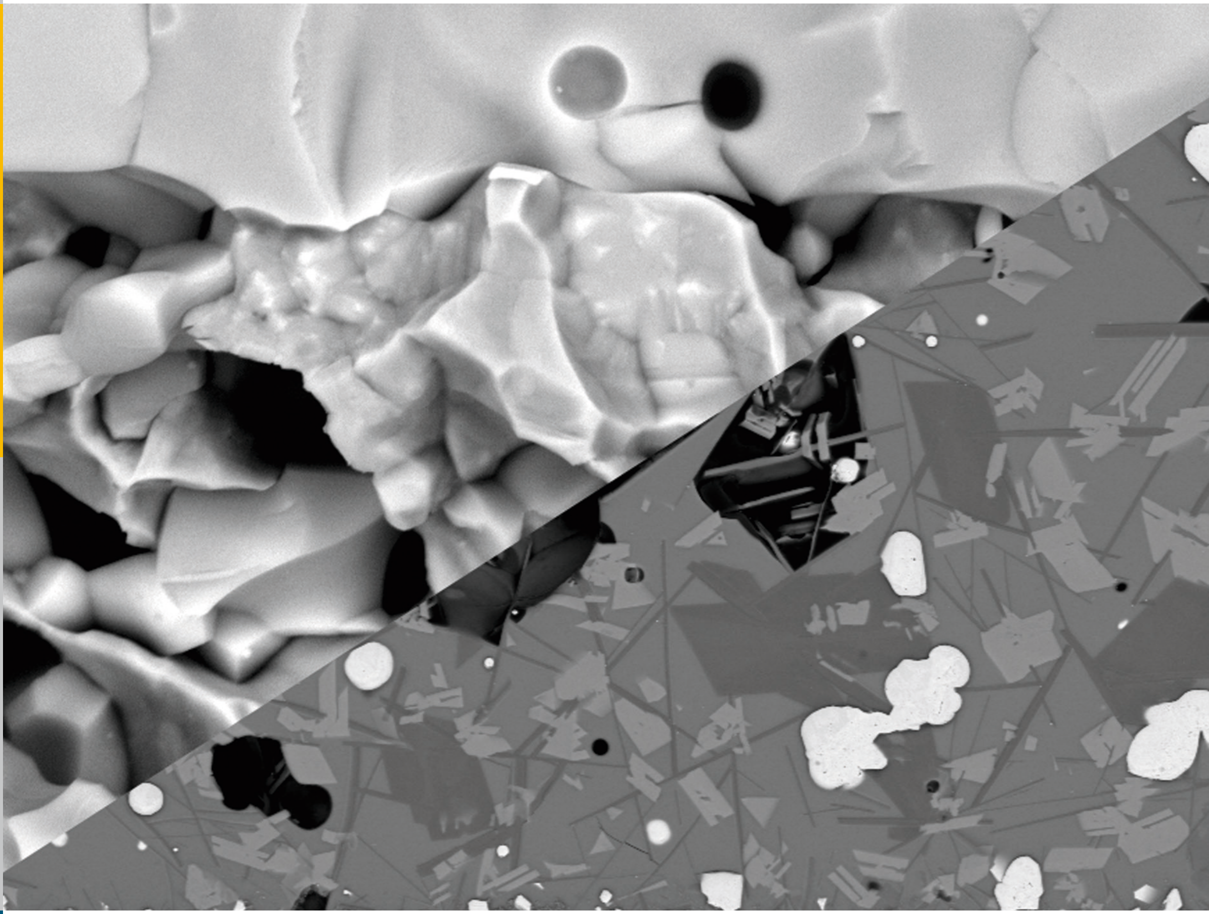

Member of the Helmholtz Association

Energie & Umwelt /
Energy & Environment
Band / Volume 391
ISBN 978-3-95806-266-5

JÜLICH
FORSCHUNGSZENTRUM

Schriften des Forschungszentrums Jülich
Reihe Energie & Umwelt / Energy & Environment Band / Volume 391

Forschungszentrum Jülich GmbH
Institute of Energy and Climate Research (IEK)
Microstructure and Properties of Materials (IEK-2)

Mechanical Characterization of Solid Oxide Fuel Cells and Sealants

Jianping Wei

Schriften des Forschungszentrums Jülich
Reihe Energie & Umwelt / Energy & Environment Band / Volume 391

ISSN 1866-1793 ISBN 978-3-95806-266-5

Bibliographic information published by the Deutsche Nationalbibliothek.
The Deutsche Nationalbibliothek lists this publication in the Deutsche Nationalbibliografie; detailed bibliographic data are available in the Internet at http://dnb.d-nb.de.

Publisher and Distributor: Forschungszentrum Jülich GmbH
Zentralbibliothek
52425 Jülich
Tel: +49 2461 61-5368
Fax: +49 2461 61-6103
Email: zb-publikation@fz-juelich.de
www.fz-juelich.de/zb

Cover Design: Grafische Medien, Forschungszentrum Jülich GmbH

Printer: Grafische Medien, Forschungszentrum Jülich GmbH

Schriften des Forschungszentrums Jülich
Reihe Energie & Umwelt / Energy & Environment, Band / Volume 391

D 82 (Diss. RWTH Aachen University, 2016)

ISSN 1866-1793
ISBN 978-3-95806-266-5

Abstract

Solid oxide fuel cells (SOFCs) have a high application potential due to the evolved demands in a global energy network. Characterization of thermo-mechanical aspects, in particular elastic, fracture and creep behavior of sealants and anode substrates, is essential to warrant reliable production and operation of planar SOFCs. In this respect, several mechanical parameters have been determined and analyzed to get insight into the mechanical behavior and possible issues for joining, thermal cycling and long term reliability of SOFC stacks and systems.

For anode substrates, facture toughness and creep behavior as major mechanical aspects were studied. In this respect, the room and elevated temperature fracture toughness of two typical anode substrate variants (NiO-3YSZ and NiO-8YSZ) were characterized in oxidized and reduced state, some selected tests were concluded for a re-oxidized state. Elevated temperature creep studies concentrated on Ni-8YSZ composites with different porosities, where different loading configurations have been compared to assess effects of compressive and tensile stresses. The interpretation and analysis of the data were based on analytical and finite element analysis.

Leakage of sealants will lead to a malfunction of the entire system, hence the structural integrity of sealants is crucial for a reliable operation of SOFC stacks and systems. In particular, Ag particle and YSZ fiber reinforced sealants, based on a glass matrix material developed in Jülich, were studied in stack operation relevant as-sintered and annealed state. Sealants supplied by Ceramics and Glass Institute (CSIC, Madrid, Spain) were also characterized and compared. Work concentrated on characterization of fracture stress at elevated temperatures on specimens mainly in a head-to-head geometry and complementary torsion tests to investigate the shear strength. The results of mechanical analysis were supported by advanced microstructural characterization and fractography to gain insight into annealing and filler reinforcement effects.

Kurzfassung

Hochtemperaturbrennstoffzellen (SOFCs) haben großes Anwendungspotential aufgrund der sich weiterentwickelnden Ansprüche in einem globalen Energienetzwerk. Die Charakterisierung thermomechanischer Aspekte, insbesondere des elastischen-, Versagens- und Kriechverhaltens von Dichtungsmaterialien und Anodensubstraten, ist wesentlich zur Gewährleistung der Zuverlässigkeit von Produktion und Betrieb planarer SOFCs. In dieser Hinsicht wurden unterschiedliche mechanische Parameter ermittelt und analysiert, um Einsicht in das mechanische Verhalten und mögliche Probleme hinsichtlich Zuverlässigkeit bei Fügung, thermischem Zyklieren und Langzeitbetrieb zu gewinnen.

Für Anodensubstrate wurden Bruchzähigkeit und Kriechverhalten als wichtigste mechanische Aspekte studiert. Dabei wurde Raum- und Hochtemperatur-Risszähigkeiten von zwei Anodensubstratvarianten (NiO-3YSZ und NiO-8YSZ) sowohl im oxidiertem als auch reduziertem Zustand charakterisiert. Zusätzliche erfolgten einige ausgewählte Tests um re-oxidierten Zustand. Hochtemperatur Kriechstudien konzentrierten sich auf Ni-8YSZ Komposite unterschiedlicher Porosität, wobei verschiedene Belastungskonfigurationen verglichen wurden, um den Effekt von Druck- und Zugspannungen zu bestimmen. Die Interpretation und Analyse der Daten basierte auf analytischen und Finite-Elemente- Analysen.

Leckage der Dichtungsmaterialien führt zur Fehlfunktion des gesamten Systems, daher ist die strukturelle Integrität der Dichtung kritisch für den zuverlässigen Betrieb von Brennstoffzellen-Stapeln und Systemen. Es erfolgten daher Untersuchungen an Ag Teilchen- und YSZ Faser-verstärkten Dichtungsmaterialien, die auf einem in Jülich entwickelten Glass-Matrix Material basierten, im für SOFC Stapel relevantem Fügezustand und ausgelagertem Zustand. Zusätzlich erfolgten Charakterisierungen und Vergleiche mit Dichtungsmaterial welches vom Ceramics and Glass Institute (CSIC, Madrid, Spain) zur Verfügung gestellt wurden. Die Arbeiten konzentrierten sich dabei auf Bruchspanngen bei unterschiedlichen Temperauren für stirnseitig gefügte Proben und komplementäre Torsionstests zur Untersuchung der Scherfestigkeit. Die Resultate der mechanischen Analysen wurden durch vertiefte Mikrostrukturuntersuchungen und Fraktographie unterstützt um das Verständnis von Auslagerungs- und Verstärkungsmechanismen zu fördern.

List of related publications and presentations

Part of the results presented in this thesis has already been published and submitted in the following articles and the following conferences:

1. J. Wei, G. Pećanac, J. Malzbender, Review of mechanical characterization methods for ceramics used in energy technologies, Ceramics International, 40 (2014) 15371-15380.

2. J. Wei, G. Pećanac, J. Malzbender, Mechanical behavior of silver reinforced glass–ceramic sealants for solid oxide fuel cells, Ceramics International, 41 (2015) 15122-15127.

3. G. Pećanac, J. Wei, J. Malzbender, Fracture toughness of SOFC anode substrates determined by a double-torsion technique, Journal of Power Sources, 327 (2016) 629-637.

4. T. Osipova, J. Wei, G. Pećanac, J. Malzbender, Room and elevated temperature shear strength of sealants for solid oxide fuel cells, Ceramics International, 42 (2016) 12932-12936.

5. J. Wei, J. Malzbender, Steady state creep of Ni-8YSZ substrates for application in solid oxide fuel and electrolysis cells, Journal of Power Sources, 360(2017) 1-10.

6. S. Rodríguez-López, J. Wei, K. C. Laurenti, I. Mathias, V. M. Justo, F. C. Serbena, C. Baudín, J. Malzbender, M. J. Pascual, Mechanical properties of solid oxide fuel cell glass-ceramic sealants in the system BaO/SrO-MgO-B2O3-SiO2, Journal of the European Ceramic Society, 37 (2017) 3579-3594.

7. J. Wei, G. Pećanac, et al., Proc. 12th Euro. SOFC & SOE Forum, Luzern, B0609, 2016.

8. J. Wei, G. Pećanac, et al., Oral presentation: Mechanical characterization of the SOFC failure-relevant ceramic components, 14th Conference of the European Ceramic Society, Spain, 2015

9. J. Wei, G. Pećanac, J. Malzbender, Poster: Thermo-mechanical properties of SOFC sealants and cells, 39th Int. Conf & Expo on Advanced Ceramics & Composites (ICACC 2015), Daytona, US.

10. J. Wei, G. Pećanac, J. Malzbender, Poster: Mechanical properties of sealants and cells, 12th Euro SOFC & SOE Forum, Luzern, A1413, 201

Content

1. Introduction

Continuously increasing population and industrial growth has increased the consumption and demand of energy. The total world's energy consumption showed a steep increment within the last 40 years [1]. Fossil fuels are expected to remain the main energy sources in the forthcoming decades. However, their combustion is widely recognized as critical, since it contributes strongly to global air pollution and global warming [2]. Clean, efficient and environmental-friendly energy source are therefore desired to be investigated by engineers and scientists.

In response to the critical need for a cleaner and efficient energy technology, fuel cells are considered as one of the most effective solutions to energy and environment problems that we face today [3]. A fuel cell is an energy conversion device that converts the chemical energy of a fuel gas directly to electrical energy [4, 5]. In this respect solid oxide fuel cells (SOFCs) have recently emerged to be a promising technology due to their reliable performance and optional wide applications in full-scale industrial and large-scale electricity-generating stations. Small SOFC based systems might be even used in mobile applications [3]. A SOFCs system utilizes a solid ceramic as electrolyte and operates at rather high temperatures (600-1000°C). They make it possible to supply clean energy with high electrical efficiencies of 45-50% and, hence, obvious significant environmental benefits [6, 7].

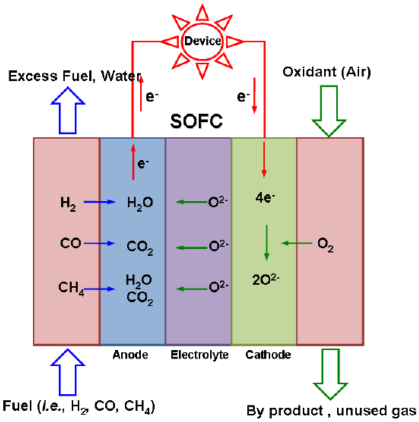

Figure 1-1: Operating principle of a SOFC [8].

The operating principle is illustrated in *Figure* ***1-1***. Fuel flows on the anode side of the SOFC, and air on cathode side. The oxygen from the air is ionized, which allows it to permeate the electrolyte membrane. Although in principle a SOFC has a very simple structures, it is still a challenges with respect to structural design and mechanical stability. After long periods of SOFC layer development the main focus concentrates nowadays on planar and tubular designs (*Figure* ***1-2***) [9]. Each of these designs has its specific benefits and drawbacks. Tubular design demonstrated good mechanical strength and sealing convenience, while the planar design offers a higher power density and lower manufacturing costs and therefore attracts increasing interests of industry [10-12].

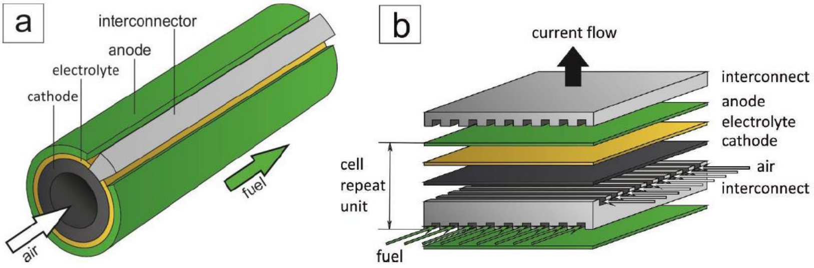

Figure 1-2: a) Tubular design and b) planar SOFC design [9].

The planar-designed SOFCs can be distinguished into the electrolyte-supported and the electrode-supported concept. The former generally uses a rather thick electrolyte (100-200 µm) as mechanical supporting part of the cell. Due to the relatively high ohmic resistance of the thick electrolyte, the typical operating temperatures of this concept are 850-1000°C [9]. Since electrolyte resistance is the most significant obstacle to reducing the operation temperature, a thinner electrolyte is preferred. Then the function of mechanical stabilization is shifted to one of the electrodes. In this approach, the anode is mostly favored due to its good electrical conductivity, hence, the ohmic resistance does not depend on its thickness [13]. The main component of anode-supported SOFC is a multilayered cell consisting of thin electrolyte and electrode layers supported by a thick porous anode substrate.

Since the single cell can only generate a limited amount of electricity, metallic interconnectors are normally used to connect single cells into a series [14]. A nickel mesh is typically inserted as the anode current collector [15]. To prevent the gases from mixing and to provide electrical insulation as well as bonding, a gas-tight sealing is essential along the edges of cell layers and interconnect layers as well as between individual cells [16]. *Figure **1-3*** illustrates the anode-supported planar SOFC design developed at Forschungzentrum Jülich (Jülich) [15]. Mechanical, chemical and thermal stability still are the main challenges and issues which affect SOFC development.

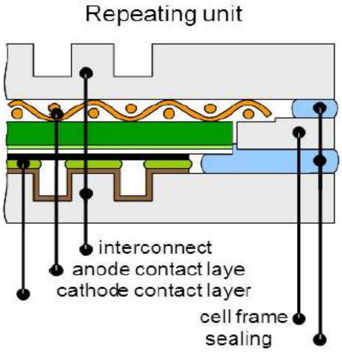

Figure 1-3: Schematic drawing of a repeating unit of a planar SOFC with a rigid glass-ceramic sealant [15].

2. Scope of the work

The work concentrates on thermo-mechanical aspects, in particular characterization of elastic, fracture and creep behavior of sealants and anode substrates for application in planar SOFCs, which should provide mechanical stability under typical operation conditions. Several mechanical parameters have been determined and analyzed to get insight into the mechanical behavior and possible issues for the joining sealing, thermal cycling and long term reliability of SOFC stacks and systems.

The work was carried out within the project "Production and Reliability Oriented SOFC Cell and Stack Design (PROSOFC)", supported financially by European Union in the 7th Framework Programme. In order to fulfil the tasks within the project, that have been identified in the consortium as critical for the reliability, different types of sealants and anode substrates have been investigated and compared within this work.

The mechanical stability of the anode substrate is obviously also crucial for reliable operation of SOFCs. Contrary to the sealant materials, where the strength was investigated as parameter for the comparison with SOFC stack stress simulations, permitting an assessment of failure probabilities, the fracture toughness was selected as relevant parameter for the anode substrates, since here the aim was to compare different materials, their advantages and disadvantages and associated mechanisms under different conditions and temperatures, without being affected by the complexity of scatter of experimental data related to Weibull distribution of fracture stresses.

In particular, facture toughness and creep behavior as the major mechanical aspects were studied. In this work, typical anode substrate materials (NiO-3YSZ supplied by the project partner TOFC and NiO-8YSZ produced in Jülich) were analyzed in as-produced, oxidized state, in reduced state and some selected tests for the re-oxidized state, in terms of their fracture toughness at room temperature and the currently typical stack operation temperature of 800°C. Creep of porous Ni-YSZ composite has been investigated under 4 % H_2/Ar atmosphere at different temperatures in the range of 800 to 900°C. Different loading configurations such as compression, four-point bending and ring-on-ring bending have been used to assess the effect of compressive and tensile stresses onto the materials creep. Ni-YSZ materials with different porosities and

Ni/YSZ ratios were tested in order to investigate material composition and porosity effects. The interpretation and analysis of the data was based on analytical and finite element analysis. The results were systematically compared and discussed with the aid of microstructural investigations.

Since leakage of sealants might lead to a malfunction of the entire system, the structural integrity of sealants is crucial for a reliable operation of SOFC stacks and systems. As application relevant parameters, fracture properties and elevated temperature deformation need to be assessed, particularly for partially crystallized glass-ceramic sealants that might suffer from instability issues at operation relevant temperatures due to viscoelastic deformation of the residual glass phase. Specimens in stack typical as-joined and annealed state, representative for stack operation, were studied. In this work, reinforced sealants, based on the glass matrix material "H" developed in Jülich, which is composed of the BaO-CaO-SiO_2 ternary system, with Ag particles reinforcement and YSZ fiber reinforcement, were characterized. Bending tests were carried out at room temperature and typical stack operation temperatures on specimen in a head-to-head geometry in as-sintered and annealed state, yielding average fracture stresses. Torsion tests were used to investigate shear strength. The results of mechanical analyses were supported by advanced microstructural characterization to gain insight into annealing and filler reinforcement effects. The results are further compared and discussed with respect to literature data and their relevance for the application in SOFCs operated at different temperatures in the range of 600 to 800°C, considering typical current but also envisaged future lower stack operation temperatures. Complementary fractographic analysis aided the interpretation of mechanical strength.

3. Literature review

3.1. Production of cells

The utilization of SOFCs systems for residential power supply and auxiliary power units still faces problems related to manufacturing costs of almost all system components. In recent years, the aim of reaching an industrialization state was the focus of the works of Risoe DTU, Topsoe Fuel Cells (TOFC), SOFCpower, Jülich and others [17-19]. In the last 15 years, Jülich has improved its anode-supported planar design. The development focused on material optimization issues, material combinations, microstructure and film thickness and especially manufacturing of cells (scales, reproducibility, etc.). For manufacturing of the porous anode substrate, warm pressing and tape casting have been used [20]. The typical procedure for manufacturing anode-supported SOFCs using warm pressing at Jülich is shown in *Figure* ***3-1***. The procedure starts with the preparation of the anode substrate powder. The material is a mixture of NiO and 8YSZ (with 8% yttria-stabilized zirconia), which is produced with a special coat-mix® powder and followed with the binder suspension [20]. The final powder is pressed at a low pressure at around 80°C. The substrate (~1000 or 1500 µm) is then pre-sintered (>1200°C) to remove the binder and prepare for the following coating steps. The anode material and electrolyte are coated by vacuum slip casting (VSC) and then co-sintered at 1400°C. After the sintering step, the half-cells are cut into the desired shape with a laser and the cathode (a La-based manganite) is subsequently coated by screen printing. With the final cathode sintering step at ~1100°C, the cell is fabrication is completed.

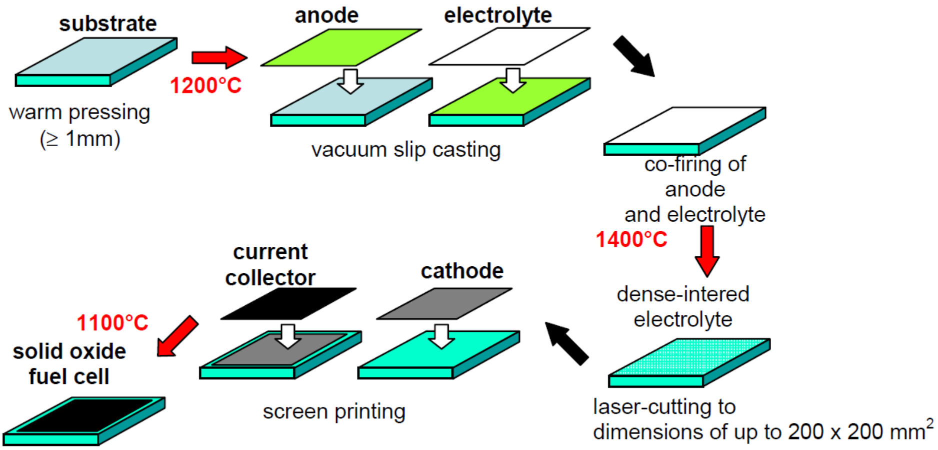

Figure 3-1: Manufacturing steps for ASCs according to Jülich technology up to 2005 [17].

However, cells manufactured with this lab-scale method always need a high proportion of manual work and hence the method is not appropriate for the industry application. To transfer the manufacturing procedure easily to industry, tape casting has been implemented to substitute warm pressing and screen printing replaced the VSC method. Tape casting is a very cost-effective process due to its high efficiency. A large amount of substrates can be produced in a short time. This technology is already well-established and well applied in industry [21]. The mixture of NiO and 8YSZ power with an alcoholic solvent and a dispersant is prepared as the slip. The slip is casted on a plastic tape, after drying and removing the plastic tape, the substrate tape is prepared completely with a thickness between 300 and ~500 µm [22]. The thickness of the anode substrate can be reduced by the tape casting technique. Sometimes a diffusion barrier layer (CGO) is needed to avoid the reaction between the cathode and electrolyte depending on the applied cathode material [23].

In order to further optimize cell manufacturing and reduce the number of sintering steps, a novel technique so-called sequential tape casting has been developed at Jülich [22]. The main difference between this novel tape casting and classical tape casting is that the electrolyte is produced first via tape casting instead of the anode substrate. Anode function layer and substrate are then tape casted onto the electrolyte layer. The differences between the classical manufacturing technology to produce anode-supported SOFCs with an LSFC cathode and the novel route are illustrated in *Figure **3**-**2***. The sequential tape casting simplified the production into two manufacturing technologies and only three sintering steps.

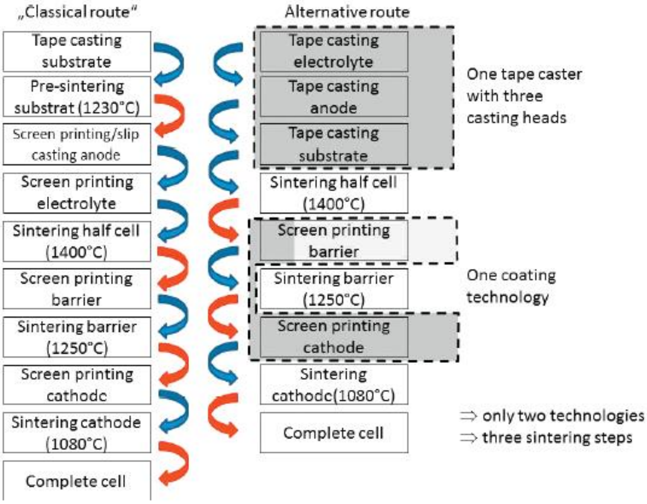

Figure 3-2: Schematic overview and comparison of the traditional and novel manufacturing route [22].

3.2. Anode materials

3.2.1. Working principle

The most common anode material is a porous Ni-YSZ cermet due to its good electro-catalytic properties along with the low cost. These anodes are typically prepared by mixing NiO with YSZ usually with an additional pore former [24]. In order to simplify the production procedure, the anode is normally produced in an oxidized state by warm pressing or tape casting [20]. Once it is exposed to hydrogen gas, the NiO is reduced to Ni. The Ni metal phase provides the electronic conductivity and catalytic activity [25]. To achieve a high efficiency and sufficient conductivity (e.g. 1000 S cm^{-1}), a porous Ni cermet has to be created. An oxidized state with usually a porosity of around 13 vol% Ni leads to the necessary porosity of 30 vol% in the reduced state [6, 26]. The gas diffuses through the pores and reacts chemically at the triple phase boundaries (TPB) of the electrochemically active anode layer which has usually the same composition as the anode substrate but a lower porosity, see *Figure **3-3*** [27].

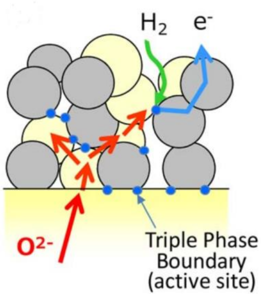

Figure 3-3: Anode reaction process in a SOFC [27].

However, the good electronic and ionic conductivity also depend on the geometry of the anode, i.e. the required electronic conductivity can vary from 1 to 100 S cm^{-1} and the ionic conductivity should be greater than 0.1 S cm^{-1} [28, 29]. The electrical conductivity of Ni-YSZ cermet strongly depends on its Ni content. To achieve a higher electrical conductivity, the Ni content needs to be optimized. The conductivity of the cermet as a function of Ni content is an S-shaped (*Figure **3-4***) curve as predicted by percolation theory. The percolation threshold for conductivity is located at a Ni content of ~30 vol% [30, 31]. The porosity affects the performance, and the optimal porosity for the electrochemical operation was found to be around 40% [32].

Hydrocarbon fuels (e.g. CH_4) are considered as the main choices to be used as SOFC fuels due to their world wide availability [33]. In fact, Ni is also a particularly good catalyst for decomposing CH_4 [34].

Continuing efforts to improve performance and reliability of SOFCs require further development of materials [14], especially in terms of mechanical aspects in particular with respect to the substrate in the anode-supported cell design [35, 36]. The anode-supported Jülich SOFC design consists of a thin (10~30 μm) anode functional layer adjacent to the electrolyte and a thick anode substrate (500~1000 μm) [37]. To achieve a sufficient operational performance, the anode of a SOFC has to meet a number of stringent criteria, such as catalytic activity towards the electrochemical oxidation of the desired fuel, good electronic conductivity (continuous Ni-phase), small mismatch in the real expansion coefficient, high permeability for the fuel gas and reaction products (well-sized and connected porous structure) and robustness if used as a mechanical support [24, 36, 38].

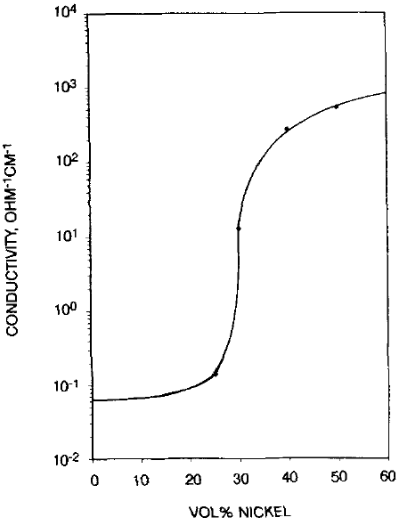

Figure 3-4: Conductivity of Ni-YSZ cermet as a function of Ni content [30].

As outlined above, a higher Ni content leads to a good conductivity, but on expense of stability due to thermal expansion coefficient mismatch with YSZ cermet [39]. Ni has a higher thermal expansion coefficient than YSZ, which causes the a thermal expansion mismatch between anode and YSZ electrolyte ($\sim 10.5 \cdot 10^{-6}$ K^{-1}) [40]. *Figure **3-5*** shows the linear relationship between the thermal expansion coefficients of Ni-YSZ cermet and increasing Ni content [41]. The mismatch in thermal expansion coefficients results in stresses, which can cause cracking or delamination during fabrication and operation [41]. These stresses can be released through creep deformation, which however also threatens the stability of the SOFCs. In this work, the effects of the anode composition on the mechanical properties, especially the creep behavior, was investigated.

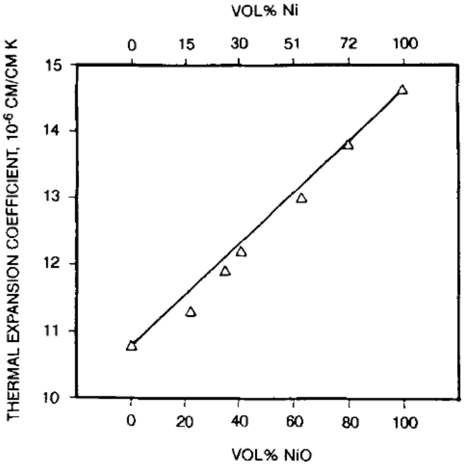

Figure 3-5: Thermal expansion coefficient of cermet anode as a function of NiO / Ni content [41].

One of the main parameters defining the actual conductivity requirement is porosity, which controls the gas transport [32, 42], however, although high porosity increases the conductivity, it can reduce the mechanical robustness.

3.2.2.Anode failures

The failure modes of SOFCs are complex and influenced by a number of factors. The origin of the failures are thermal or chemical stresses which arise during manufacturing and operation [43]. The formation of damage in SOFCs is summarized in *Figure **3-6***.

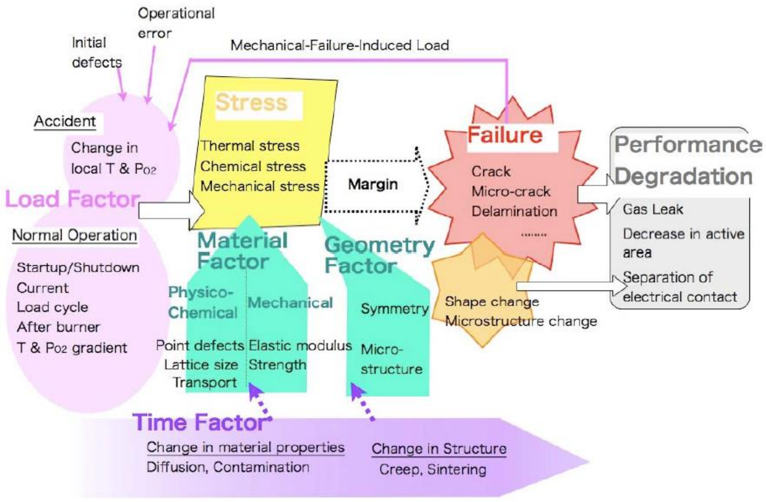

Figure 3-6: A generalized scheme of formation of failures in SOFCs [43].

The internal stresses within the cell layers are mainly a result of thermal gradients, electrochemical reactions and mismatches of material behaviors (thermal expansion coefficient, etc.) under changing environments [44]. These stresses can lead to fracture, deformation and delamination of the cell layers. For example, the thermal expansion coefficient of Ni-8YSZ anode with 65% wt. Ni is around $13.1 \cdot 10^{-6}$ K^{-1} from RT to 800°C, while the value of dense 8YSZ is around 10.5 10^{-6} K^{-1} [40, 41]. This thermal expansion difference results in residual stress in anode and electrolyte layers and leads to creep deformation at operation temperatures, which threatens the long-term reliability of SOFCs. Additional stress will be induced by the constraints imposed by the sealants and interconnect due to differences in thermal expansion, thermal gradients and simply mechanical loads.

Another reason that could cause stresses is the volume change due to the re-oxidation. Re-oxidation may occur at high temperature due to sealant damage causing a lack of fuel gas. The rapid oxidation causes a volume expansion of Ni particles in the YSZ matrix, which leads a volume increase of the anode compared to the initial oxidized state [45, 46]. Associated tensile stress/strain induced in the electrolyte layer leads to cracking as illustrated in *Figure **3-7*** [47].

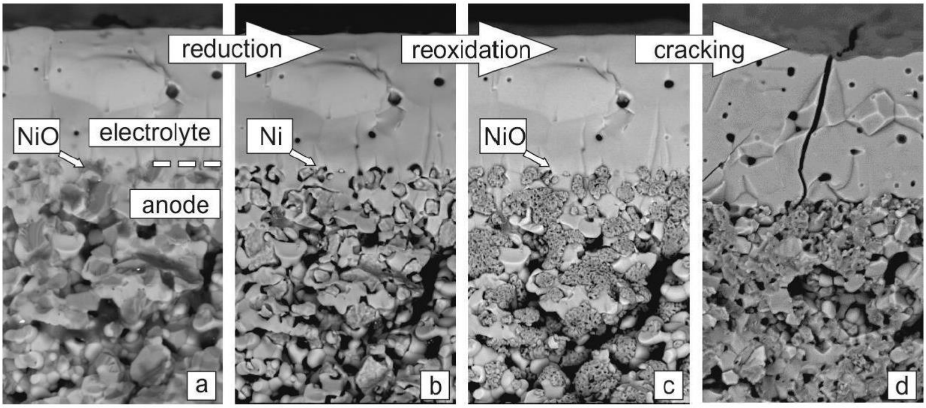

Figure 3-7: SOFC half-cell: (a) sintered in air (oxidized state); (b) reduced state; (c) re-oxidized state; (d) cracked electrolyte layer after re-oxidation [47].

3.3. Sealants

3.3.1. State of sealants for SOFC application

There has been an increasing amount of work on sealant materials searching for enhanced properties leading to a large number of research works in recent years [48]. Today, efforts concentrate on improving performance under the rather extreme operation relevant conditions, where sealants need to be designed for high temperatures and high-stress applications [16, 49]. Joining dissimilar materials represents a great challenge due the differences in physical properties, such as melting points and thermal expansion coefficients (CTEs), undesirable interactions, robustness problems, etc. [50]. The understanding of materials, microstructure and mechanical properties of bonded or welded joints leads to the necessity to reassess joining techniques.

With the fast development of electrochemical devices (i.e. SOFCs) and high-temperature separation membrane reactors, various sealants have been developed for high-temperature applications [51, 52]. The high operating temperature necessary for solid-state electrochemical operation (650°C - 1000°C) considerably limits the variety of sealing options; in principle organic or polymer seal cannot be employed, while inorganic materials with high melting points can be easily and widely used at high temperature above 600°C [53]. An overview of conventional high-temperature seals is given in *Figure **3-8*** [15].

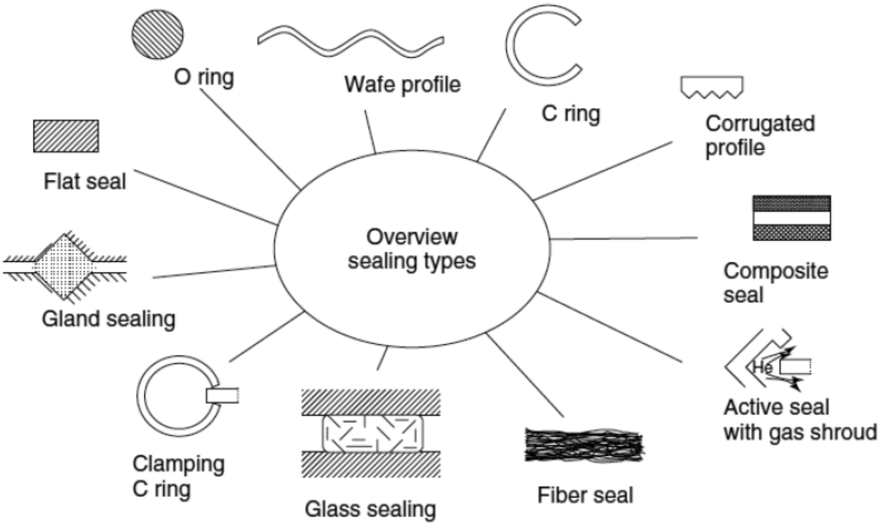

Figure 3-8: An overview of the current sealing types for high-temperature applications [15].

Choosing a sealant material for those high temperature applications can therefore be a challenging task. Several requirements need to be satisfied in order to achieve a successful combination. The basic requirements for materials to be used as sealant in SOFCs can be summarized as follows [8, 54-56]:

- Chemical stability at the operation temperatures in oxidizing and reducing atmospheres (i.e. air, H_2)
- Chemical compatibility with the adjoining SOFC components (i.e. no poison)
- Gas stream separation (hermetic seal)
- Electrical insulation
- Matching coefficient of thermal expansion with the joining components (~10-12 $\cdot$ 10^{-6}/K)
- Long-term mechanical reliability during high temperature operation and thermal cycles

In the last decade, various papers and review articles have been published reporting significant research and development progress for sealants [57-59]. The options for sealing and joining in planar SOFCs can be broadly classified into three types: rigid bonded seals, compressive seals, and compliant bonded seals [58]. Each represents advantages and limitations.

Rigid bonded seals

In rigid bonded sealing, the sealant forms a joint without deformation. Since the final joint is brittle, it is susceptible to fracture when exposed to tensile stresses encountered during non-equilibrium thermal events or due to thermal expansion mismatches between the sealant and adjacent substrates [60, 61]. Glass and glass-ceramic sealants are considered as good candidate materials for the SOFCs application due to their chemical stability on the reducing and oxidizing atmosphere, they are generally inexpensive, tailoring performance depending on composition design is possible and a flexible fabrication process is applicable [62, 63].

They are characterized by a glass transition temperature (T_g). For the initial stage of the joining process, sufficient flow of the sealant is essential, then the glass should partially or fully crystallize to form a rigid and bonded seal [63, 64]. Crystallization is considered to have a positive effect on withstanding thermal stress [65].

Various glass-forming systems have been studied for SOFCs sealant application. Previous work has shown that phosphate and borate glasses are not sufficiently stable in the humidified fuel gas environment due to corrosion effects [12, 54]. Silica with various modifiers added to increase CTE and improve adhesion and joint strength has shown the best performance. The use of alkaline-earths to form systems such as $BaO-CaO-SiO_2$ and $BaO-Al_2O_3-SiO_2$ can yield glass-ceramics with higher chemical resistance and less reactivity with other stack components [66, 67]. To achieve the proper balance of material properties, the key parameters, including T_g, CTEs, wetting behavior, and bulk strength must be simultaneously controlled. One of the effective methods is to tailor the initial glass and the heating schedule employed during the joining [56, 58]. The compositional modifiers listed in table are commonly added to alter the initial bulk properties of the glass-ceramic sealants [58].

Table 3-1: Common compositional modifier for silicate-based glass-ceramic sealants [58].

Modifier	Function
Al_2O_3	Allows control over viscosity through the rate of crystallization
B_2O_3	Reduces T_g, and viscosity and improves wetting
BaO	Reduces T_g, and raises CTE in the glass-ceramic
CaO	Reduces T_g, and raises CTE in the glass-ceramic
MgO	Reduces T_g, and raises CTE in the glass-ceramic
La_2O_3	Used as a viscosity modifier and long-term CTE stabilizer
GuO	Improves surface adherence
MgO	Improves surface adherence

Compliant bonded seals

Compliant bonded seals can, unlike rigid bonded sealants, be plastically deformed, forming a joint at or above room temperature. Due to this compliant deformation, the thermal expansion mismatch stress and residual stress can be mitigated and seal-healing is possible [68]. However, potential issues exist such as electrical instability, poor oxidation resistance and undesired reaction with other components of the SOFC stack [15, 69].

Compliant bonded sealants are mostly metal-based materials, which easily cause electrical conductivity or non-uniform composition distribution under the electrical field [58]. For example, Alkalis, i.e. sodium and potassium, are commonly added to the glass to lower the melting temperatures. However, it is possible that the alkalis may accumulate near the electrode due to the mobile ions moving under an external electrical filed, which results in a non-uniformed distribution in the bulk glass matrix. The higher concentration of alkalis can reduce the glass viscosity and hence enhance corrosion along the interfaces [70].

Compressive seals

Deformable materials can be employed as seals that do not bond to the SOFC components but serve as gaskets instead. External forces are applied to components and cause sealing. The sealing surface can slide along its counterpart without a disruption in hermeticity and the individual stack components can expand freely without necessity of CTE matching [58]. This offers possibility for stack repair by releasing the compressive load, disassembling the stack and replacing the damaged components. However, compressive seals require a maintenance of the necessary level of compressive load, which introduces a complexity in stack design, including load relaxation due to creep, increased weight and thermal mass [58, 59].

Metal gaskets have been studied for compressive sealing. For example, gold and silver as non-oxidizing noble metals can form hermetic sealing at pressure of ~ 25 MPa [71, 72]. Oxidation-resistant alloys such as stainless steel and nickel-based superalloys are also considered as candidate for the compressive sealing [73]. An alternative to metal-based gaskets is the use of mica-based materials, which are well known for their high resistivity and uniform dielectric constant. Simner and Stevenson [74] have investigated forms of mica, including muscovite paper, muscovite single-crystal sheets and phlogopite paper, where the cleaved muscovite sheet showed the lowest leakage rates. Chou et al. [75-77] reported improvements of these mica-based seals by infiltrating the mica particulates with a wetting or melting-forming agent such as $Bi(NO_3)$ or H_3BO_3.

3.3.2. Reinforcement of glass-ceramic sealants

In order to improve the mechanical properties of sealants, adding fillers as reinforcement is considered to be an effective method [51]. The Ashby material selection method provides an appropriate tool and basic clue to optimize the choice of the filler material for a specific application. An Ashby chart illustrating the relationship between strength and toughness of different materials is shown in *Figure **3-9*** [78]. The fracture properties of the chosen materials should fit the requirement of application as a sealant. The chart guides selection of materials to meet the design criteria for facture stress and toughness. Nevertheless, to identify proper classes of materials for a specific application, the relationships of elastic modulus, thermal expansion and thermal conductivity needs also to be carefully considered. Two types of fillers are widely used, i.e. ductile or brittle material with high fracture toughness and elastic modulus. The mechanism of sealant enhancement can generally be described as follows.

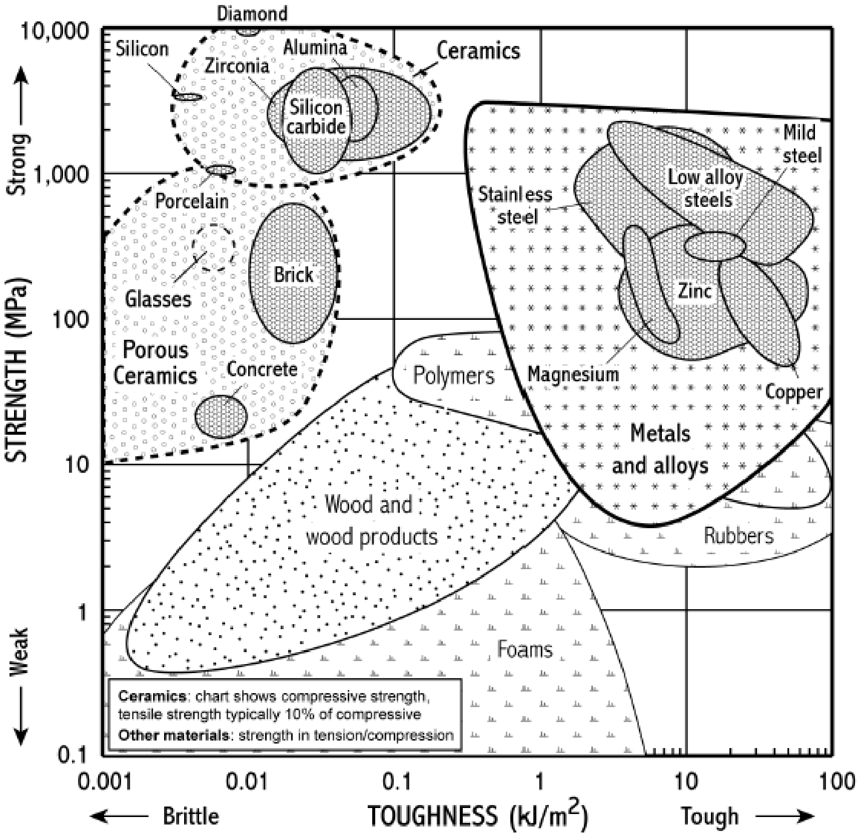

Figure 3-9: Ashby chart of strength vs. toughness of materials [78].

Plenty of studies have been focused on ductile metal particles due to the wide variety of choices and accessibility [79]. Ductile metallic particles can absorb fracture energy and increase the strength of the composite by bridging the crack [79], if the particles are well-bonded to the matrix and the crack will pass through the particles [80]. Theoretically, the toughening effect should increase with the volume fraction of metallic particles, while excessive adding of metallic particles might cause the interconnection of particles and lead to problems related to loosing electrical insulation and corrosion resistance. Therefore finding limitations and controlling the amount and distribution of reinforcement fillers are also key points for the application. Greven

[78] reported on the influence of different amounts of Ni particles on the reinforcement of a Barium-Calcium-Silicate glass matrix. An increased amount of Ni particles in the composite provoked oxidation and increased the porosity, where 50 wt.% reinforcement led to full oxidation after joining. Although the selected fillers should be chemically stable and not lead to reactions with glass matrix, Cu revealed a strong reaction with Barium-Calcium-Silicate based glass matrix.

Ceramic fillers such as brittle filler materials have also been widely studied [81]. The mechanism of enhancing the toughness is mainly related to crack deflection effects. Deflection toughening arises whenever interactions between the advancing crack front and particle cause a deviation of the crack front from planarity. The stress-intensity factor in front of the crack tip can be reduced effectively by this interaction. Barium-Calcium-Silicate based glass matrix with YSZ particle reinforcement called H-P was characterized systematically in [65]. The strength of H-P was reported to be 22 ± 2 MPa at room temperature and decreased with increasing temperature. A RT fracture toughness of 0.9 ± 0.2 $\mathrm{MPa \cdot m^{1/2}}$ was obtained from indentation tests [82, 83] .

The use of ceramic filler materials in an established glass sealant matrix leads to new glass-ceramic composites that require detailed investigation, including consideration of the influence of filler materials on strength of the joint and non-elastic deformation at joining temperatures [84]. Several studies [51, 83, 84] indicated remarkable development. Jülich has developed and improved glass and glass-ceramic sealants to fulfill the requirements of planar SOFC stacks [85]. Glass H as one of the glasses developed at Jülich showed remarkable joining properties and has been used in stacks [9, 84]. However, the insufficient strength of this glass limits the application under operation relevant conditions. Therefore, the study focused on reinforcing the glass H matrix using various fillers.

3.3.3. Failure of sealants in SOFC stacks

Hermetic sealing is a key requirement for the operation of SOFC stacks in a system environment. The seals have to withstand high temperatures combined with oxidizing and reducing atmospheres as well as the mechanical stress caused by temperature gradients during operation and thermal cycling [84]. FEM simulation verified high local stresses in the sealants (*Figure* ***3-10***). The location of the highest principal stress corresponded with the location of leakages [84].

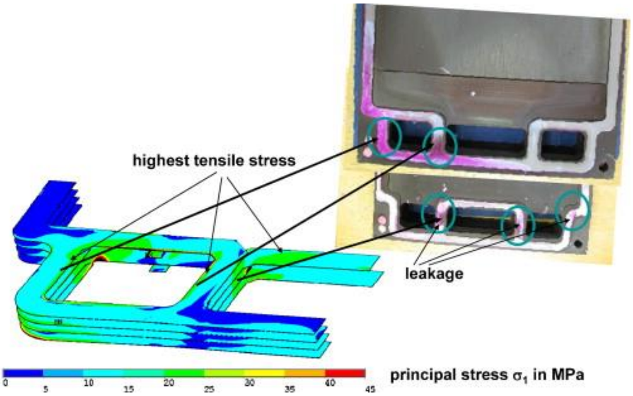

Figure 3-10: FEM simulation of principal stress distribution with localized leakages [84].

The highest tensile stresses normally arise at room temperature due to CTE mismatch. Glasses and glass-ceramic materials are well-known to be easily destroyed under tensile stresses [51]. Defects can act as pre-cracks and propagate rapidly under tensile stress. The characterization of the mechanical behavior based on the tensile / bending strength is used [86]. The strengths of various sealant materials at room and elevated temperatures have been reported in [49, 82]. However, it has been shown that sealants under operation relevant conditions are not only exposed to tensile but also shear stresses [87]. Previous work concentrated mainly on the shear strength assessed via torsional testing at room temperature [55, 88], in fact, the current work extents this to elevated temperature testing via an in-house developed set-up.

3.4. Mechanical characteristics

Ceramic materials are widely used as components in SOFCs and also as oxygen transport membranes, due to their favorable transport properties and chemical stability [89]. The basic problems such as reliability and robustness [90] are always issues for brittle ceramic materials, which emphasizes the need to understand and characterize necessary mechanical parameters. In the following sections, basic principles and theoretical backgrounds of the mechanical investigations performed within the present study are introduced, and the use and limitations of different mechanical testing methods for ceramics is discussed.

3.4.1. Elastic behavior

The elastic modulus defines the elastic behavior of a material, which makes it a key input parameter for analytical and numerical calculations that link stresses and strains. The elastic modulus E describes the resistance to elastic deformation of an isotropic material when it is loaded uniaxially. It is defined by Hooke's law as the ratio of stress to strain during elastic loading:

$$\boldsymbol{E = \frac{\sigma}{\varepsilon}} \tag{3-1}$$

where σ is the stress and ε is the strain.

3.4.1.1. Techniques for elastic modulus determination

Elastic modulus can be determined using different methods. For brittle ceramic materials, indentation as non-destructive method as well as bending test and impulse excitation technique are commonly used [86].

1) Micro-indentation test

In indentation testing, the elastic modulus can be determined from the load-depth curve [91]. Indentation with a Vickers tip is the most common test, other indenter tips like Berkovich, Rockwell, Knoop or Shore are also widely used [92]. The elastic modulus is calculated from the unloading curve, which represents elastic response of the material [93, 94]. The general advantage of the indentation test is that it is a fast serial test and only a small specimen volume is required, so it can be considered as a macroscopically non-destructive test. The disadvantage is that the properties are representative only for the location where the test is carried out. Especially for highly porous materials the scatter can be very large.

2) Bending test

The bending test is a widespread method for analyzing materials' behavior especially for ceramics where tensile testing is not an option [95]. The alignment is easily achieved and specimens with simple geometric shapes can be used. The elastic modulus is usually determined from the load-displacement curve obtained in either a three-or four-point bending test for bar-type specimens (*Figure **3-11**.* (*a), (b)*) or for plates via ring-on-ring, ball-on-ring or ball-on-three balls test (*Figure **3-11**.* (*c*) – *(e)*) [96]. The testing of plates has become very common since advanced materials processing often relies on tape casting techniques [22], yielding plate type specimens in either dense or porous state. The latter are representative for the porous substrate and used in SOFCs or membrane designs [97]. For tubular geometries, which are still occasionally used as SOFC, testing methods such as O-ring, C-ring (*Figure **3-11**.* (*g*)*, (h*) [98] or four-point bending of semi-cylindrical specimens [99] can be applied (*Figure **3-11**.* (*f*)). The initial part of the load-displacement curve can be affected by contact problems related to roughness or biased by surface waviness. Hence, sometimes a grinding or polishing process is advantageous for plates or bars to yield materials representative curves which lead to a more precise determination of elastic modulus [100].

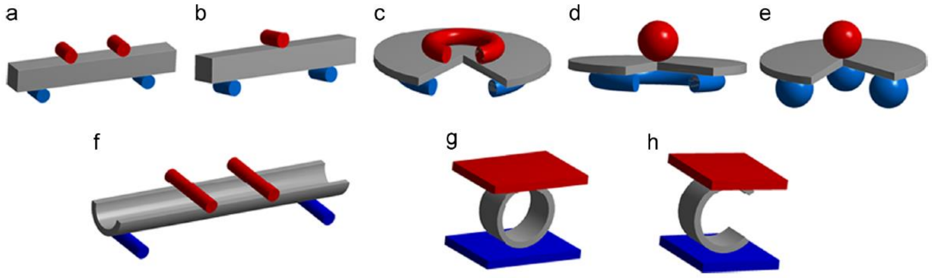

Figure 3-11: Different methods to test elastic modulus and strength in bending: (a) four-point bending, (b) three-point bending, (c) ring-on-ring, (d) ball-on-ring, (e) ball-on-three balls, (f) four-point bending of semi-cylindrical specimens, (g) O-ring, and (h) C-ring [86].

3) Impulse excitation test

An advanced method to determine the elastic modulus for certain specimen geometries is the impulse excitation method, where the specimens’ resonance induced by a mechanical impulse is detected acoustically [86]. *Figure **3-12*** is a simple schematic of the impulse excitation technique, where a slight impact is induced at a side of the solid specimen.

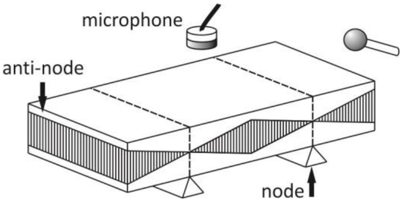

Figure 3-12: A schematic of the impulse excitation technique.

The resonance frequency is then used to calculate the elastic modulus. The value of the elastic modulus can be determined via [101]:

$$E = 0.9465 \cdot \frac{m \cdot f_f^2 \cdot t^3}{b \cdot h^3} \cdot T \cdot \left(\frac{h}{l}\right) \tag{3-2}$$

where m is the mass, f_f the resonant frequency, l the length, b the width, h the height and $T(h/l)$ a geometry correction factor.

The method appears to have a higher accuracy than the four-point bending test [102]. Moreover, it is less time consuming when testing elastic modulus as a function of temperature. Experiments at elevated temperatures and under different atmospheres are possible with suitable set-ups. For example SOFC half-cell materials have been tested up to the typical operation temperatures under oxidized (NiO-YSZ) and reduced conditions (Ni-YSZ) [103].

In addition to the elastic modulus, this method can be also used to determine Poisson´s ratio [40] and the damping coefficient, latter being determined from the decay of the resonance frequency. This parameter gives information on the occurrence of non-elastic mechanisms (phase changes, viscous deformation or creep) and processes (atomic defect interactions) [104].

Problems arise in the case of materials that possess a large damping coefficient where the signal decays too fast and the limits of the experimental analysis can be reached. Furthermore, extremely thin (light) specimens can cause experimental problems due to a displacement of the sample during testing.

3.4.1.2. Porosity influence on elastic modulus

As well known, porosity influences the elastic modulus of materials. Many studies exist on the effective elastic moduli of porous solids treating them as two-phase materials, with the second phase being a void, and several empirical equations have been derived for describing the effective elastic moduli as a function of porosity [105]. The linear relation, equation (3-3) in *Table **3-2***, was first used by Fryxell and Chandler [106]. The exponential relation, equation (3-4), has been used frequently and was initially proposed by Spriggs [107]. Hasselman [108] suggested a non-linear relation , equation (3-5), which considered the voids as a dispersed phase.

Some theoretical expressions have been obtained from more fundamental analytical models, which encompass the effect of shape, volume, distribution and interaction of pores on the elastic constants [109-111]. However, analytical procedures considering the two-phases as continuum materials are not directly applicable in cases where the second phase is a void. Ramakrishnan and Arunachalam [112, 113], equation (3-6), developed a theoretical approach for determining the effective moduli of porous solids with randomly distributed pores on the basis of the composite sphere method (CSM). Phani and Niyogi [114] proposed on the same basis equation (3-7).

Table 3-2: The relations between porosity and elastic modulus.

Equations	
$E = E_0(1-mP)$	(3-3)
$E = E_0 \exp\left(-bP\right)$	(3-4)
$E = E_0(1+\frac{AP}{1-(A+1)P})$	(3-5)
$E = E_0 \frac{(1-P)^2}{1+k_E P}$	(3-6)
$E = E_0(1-aP)^n$	(3-7)

The pores not only affect the elastic behavior of the materials, but also influence other mechanical properties such as fracture strength, fracture toughness, creep, etc.

3.4.2. Fracture strength

Due to the importance of giving a loading/stress limit for application, fracture strength is one of the most commonly cited properties for ceramic materials. In the SOFC system, a high mechanical reliability is needed [115]. Strength characterization is necessary to validate and optimize the quality of the production of cells [116]. A number of techniques and methodologies have been developed for the measurement of fracture strengths. Compressive strength of ceramics is generally higher than their tensile strengths; most of these techniques equate the fracture strength to the maximum tensile stress at fracture.

For bar-shaped specimens, three-and four-point bending tests (*Figure **3-11*** (*a, b)*) are the effective methods to determine the fracture strength, however, a careful preparation of the edges and surfaces is required to gain the material's representative properties [117]. Advanced set-ups can permit the measurement of entire specimen series even at elevated temperatures [116]. During the tests, some modified specimen geometries, such as head-to-head specimen of sealant, are widely used to mimic the real operation environment in SOFC stack, which provide more information [118]. Ring-on-ring, ball-on-ring, ball-on-3-balls or pressure-on-ring set-ups (*Figure **3-11*** (*c – h)*) are widely used on plate-shaped specimens. Due to the thin plate-sharped SOFC cell layers, these testing methods show clear advantages. Here the highest stress occurs within the central part of the specimen and the edges are under very low and negligible stress, which release the requirement of the edge preparation. Layered composite plates can show curvature effects. In the case of wavy specimens, the ball-on-three ball method was shown to be advantageous [117].

To mimic the real case in the SOFC stack, a joined specimen so called head-to-head specimen has been successfully used to determine the fracture stress in Jülich [82, 118]. *Figure **3-13*** shows a schematic of the bending test on head-to-head specimen. A complementary statistical Weibull analysis yields the characteristic fracture strength and the Weibull modulus, which gives information on the fracture stress distribution. Characteristic strength and Weibull modulus can be used to determine and predict the failure probability for a given stress state [119].

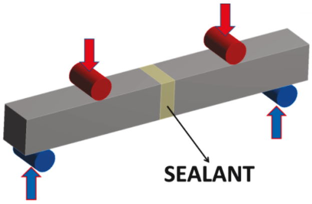

Figure 3-13: Head-to-head specimen loaded in a 4-point bending test.

The sealant material in an SOFC stack is exposed to tensile and shear stresses [120]. Hence, the characterization of shear strength is an issue and several mechanical tests have been developed and used, but few standard tests are available and universally accepted. The asymmetrical four point flexural test (ASTM C 1469-10, as shown in *Figure* ***3-14*** (*a*)) [121] is recommended to measure shear strength of ceramic butt joints, however, there are some serious shortcomings of these testing methods, such as difficult sample preparation or a minimal displacement and difficult avoidance of misalignments in the test set-up. Commonly adopted test methods like single lap shear test (*Figure* ***3-14*** (*b)*) do not measure shear strength properly: they give "apparent shear" resulting from a mixed state of stress included shear, bending, and tensile stresses [122]. FE simulation indicates that the stress distribution in the middle of the joint also combines a shear stress and a traction normal stress [122]. A lap based test (ISO13124 standard) with a cross-bonded specimen faces a similar issue, which can therefore only provide an apparent shear strength, as shown in *Figure* ***3-14***. (*c)* [123].

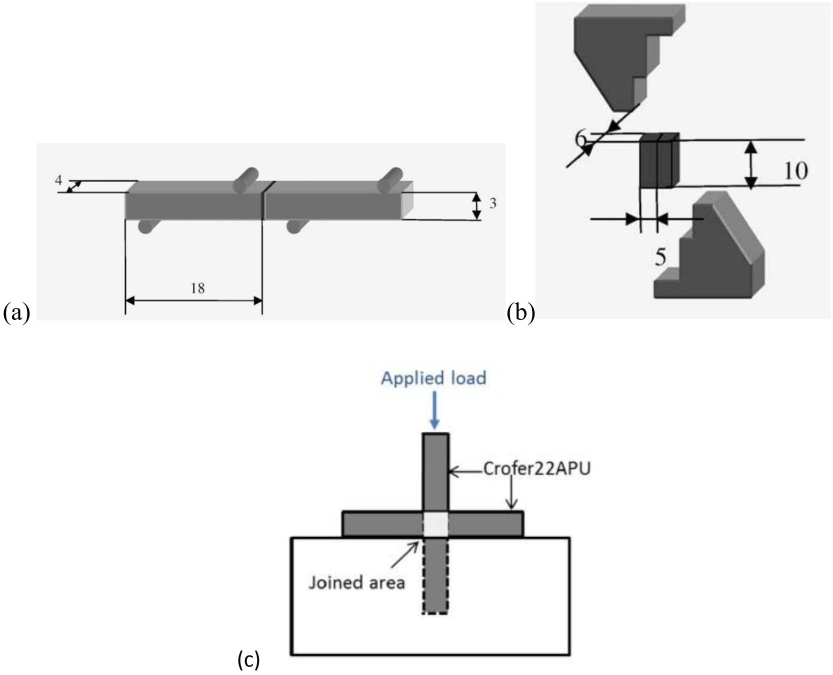

Figure 3-14: Shear testing methods (dimension mm): (a) asymmetrical four-point bending test; (b) single-lap test in compression (SL)(c) cross-bonded test (ISO13124 standard) [122, 123].

Schwickert [124] reported on sealant-metal joints to measure the shear stress. The tests were performed in cooperation with the IWM in Freiburg, Germany. The simple shear test specimen is shown in *Figure* ***3-15*** (*a)*, however, again loading in a combined bending – shear mode can be expected.

While not only the shear stress can be determined during the shear test, shear modulus, internal stress and viscosity have been also determined on Jülich sealant using a symmetric shear test at SOFC operation temperature.[125]. A schematic drawing of the symmetric shear test specimen is shown in *Figure* ***3-15*** (*b)*.

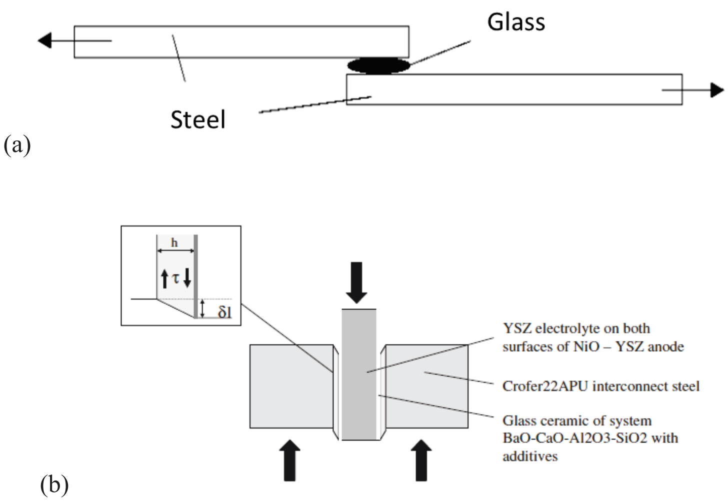

Figure 3-15: Schematic drawing of (a) sealant-metal jointed shear test specimen [124];(b) the symmetric shear test [125].

A torsion test is considered as an effective way to measure the shear strength [87]. Ferraris et al. [123] proposed some modifications of the torsion test and aiming at a measurement of the pure shear strength of the joints [121]. A modified hourglass shaped configuration has been designed. The configuration is shown in *Figure **3-16***. It has been successfully used on SiC and glass-ceramic materials [121, 123]. However, since their torsion set-up was limited to RT, a new torsion set-up has been developed at Jülich, which aims at a measurement of the shear strenght of sealants also at high temperatures. In the current work some typical SOFC sealants were tested at RT and elevated temperatures.

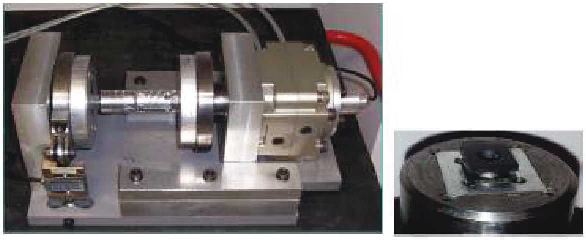

Figure 3-16: Experimental set-up and specimen for torsion test [122].

3.4.3. Fracture toughness

Ceramic and ceramic composites can have a rather high strength but also a quite low crack resistance at the same time [126]. The crack resistance, which is proportional to the fracture toughness, is critical for ceramic components as used as cell in SOFCs operating under extreme mechanical and thermal loads. Hence, fracture toughness is an important property of advance ceramics and is one measure of brittleness and crack resistance [127].

A crack can be loaded three ways, termed mode I, II, III as illustrating in *Figure **3-17***. Mode I is an opening mode, while mode П and mode Ш are in-plane and out-of-plane shear mode, respectively [128].

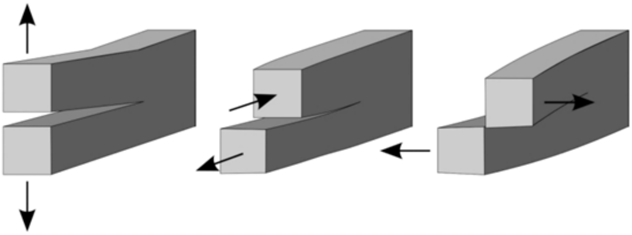

Figure 3-17: Three different fracture modes: (a) Mode I (opening mode), (b) Mode II (in-plate shearing), (c) Mode III (out-of-plate shearing).

The stress intensity around a crack can be generally expressed in terms of equation (3-8) [127]. When the stress intensity, K_I, reaches a critical value, the so-called fracture toughness, K_{IC}, the crack propagates and fracture appears. K_{IC} is related to the energy release during crack growth, which is expressed in equation (3-9) [128]. The critical stress intensity for mode I is most widely used and termed fracture toughness [129], which is related to the flaw/crack size and the fracture energy, respectively:

$$\boldsymbol{K_I = Y \sigma \sqrt{c}} \tag{3-8}$$

$$\boldsymbol{K_{Ic} = \sqrt{E\,G_c}} \tag{3-9}$$

where Y is the shape factor, c the flaw depth and G_c is the release rate of critical energy. The crack extension is usually depicted on a V- K_{IC} graph as shown in *Figure **3-18***, where V is crack velocity. Region I and II behavior are controlled by the environment, whereas region III crack extension is intrinsic to the material [127, 130].

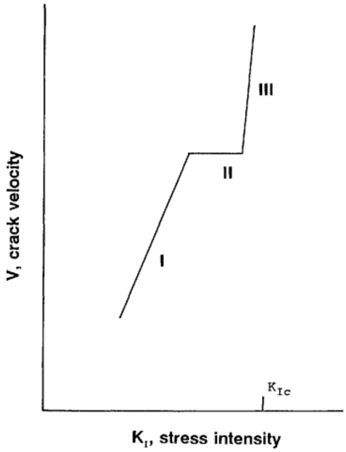

Figure 3-18: Crack growth can be differentiated into three regions. Environmentally-assisted crack growth occurs at stress intensities less than K_{IC} [127].

Different testing methods have been developed and optimized to determine fracture toughness of ceramics [86]. Indentation testing is one of the methods that might be used to determine fracture toughness. In this test fracture toughness can be determined from the length of cracks, which might propagate from the vertices of the indents. Crack initiation depends on the applied load and the materials' fracture toughness [131]. The advantages of this test are that only a small specimen size is required and the easy experimental routine, requiring only a measurement of the crack length after the test. This technique found widespread use for the analysis of ceramics used in SOFC anodes, ceramic membrane materials and sealants [132-136]. However, this testing method reveals an apparent disadvantage, which the crack path could be terminated and blurred by pores in the materials. Hence, it can be very difficult to determine the crack length precisely.

Bending tests as an alternative method are also widely used to investigate the fracture toughness [86]. They avoid the shortage of indentation on porous materials and also obtain a more representative property for the materials [86]. For plate-shaped specimens like SOFC cell layers, the double torsion (DT) test is as an effective means, which requires the edge of a notched plate specimen to be loaded in a bending mode. The fracture toughness can be determined from a controlled crack propagation load as exemplified for SOFC materials in [137]. Similarly, a double cantilever beam (DCB) test is another testing method which is suitable for testing of notched plate-shaped specimens or thin solid films. The sample is also loaded via pure bending moments [138]. The methods can be used for elevated temperature testing. Schematics of both methods are shown in *Figure **3-19***.

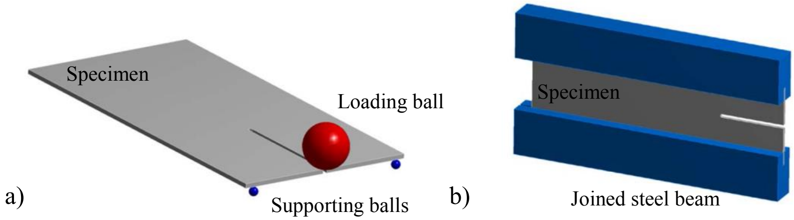

Figure 3-19: Schematic of a) double torsion and b) double cantilever beam test [86].

Recently, a new testing method, so called slender cantilever beam (SCB) test, is proposed by Vandeperre, Wang and Atkinson [139]. It can be used for measuring the stiffness and toughness of thin specimens using the high load and displacement resolution of a nano-or micro-indenter. A notched cantilever beam is clamped on the sample holder with isocynate adhesive as shown in *Figure **3-20***. A spherical sapphire indenter tip with a diameter of 500 µm is used for applying the load to the cantilever beam on the center line of its upper face. This testing method is advantageous for thin plate specimen and doesn’t need a specially designed set-up; the load can be applied by indentation with high resolution. However, similar as in the case of DT specimens, the specimens need to be pre-notched before the test.

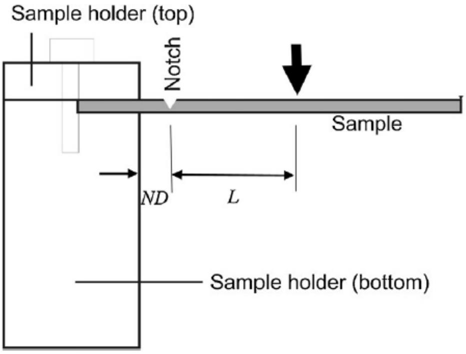

Figure 3-20: Schematic of the sample clamping arrangement of the slender cantilever beam test [139].

3.4.4. Creep

Creep is one of the most critical parameters determining the integrity of components exposed to elevated temperatures, such as SOFCs [140]. At sufficient high temperature, plastic deformation can occur even when the stress is lower than the yield stress. This time-dependent deformation is known as creep [141]. As a consequence of such deformation, unacceptable dimensional changes and distortions, as well as rupture can occur [142]. During constant loading, the strain varies as a function of time, which is illustrated in *Figure* ***3-21***. This behavior is generally divided into three regions: primary, secondary (steady-state) and tertiary creep. The steady-state creep often dominates the creep behavior. In this region, the strain rate is constant and a balance appears to occurs between hardening and softening processes in this region [143].

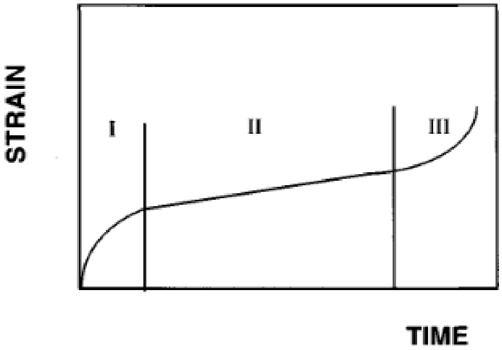

Figure 3-21: Three stages of creep: I primary, П secondary (steady-state), and Ш tertiary [143].

(1) Creep mechanisms

The mechanisms involved in creep need to be identified and analyzed, especially the mechanisms involved in steady-state creep. For ceramics' creep, three main creep mechanisms are proposed: diffusion creep, dislocation creep and grain-boundary sliding [143].

Diffusional creep occurs by transport of vacancies and atoms via diffusion. Like all diffusional processes, it is driven by a gradient of free energy, created in this case by the applied stress [141]. Under the action of an applied stress the equilibrium number of vacancies is shifted. Thus, the temperature is high enough, the vacancies along with a counter flow of atoms will move towards regions under the applied stress. When the diffusion paths are predominantly through the grains themselves, this lattice diffusion mechanism is termed as Nabarro-Herring creep [144]. When the diffusion paths are through the grain boundaries, it is termed Coble creep [145]. The former mechanism is favored at higher temperatures, while the latter is preferred at lower temperatures. The diffusion paths are illustrated schematically in *Figure* ***3-22***. The stress-induced lattice diffusion and the strain produced by this diffusion process in a single crystal are displayed in the first figure, which schematically describes Nabarro-Herring creep. In polycrystalline materials such as Ni-8YSZ, diffusional creep may also occur by diffusion through the grain boundaries. The possible diffusion path is represented in the second figure.

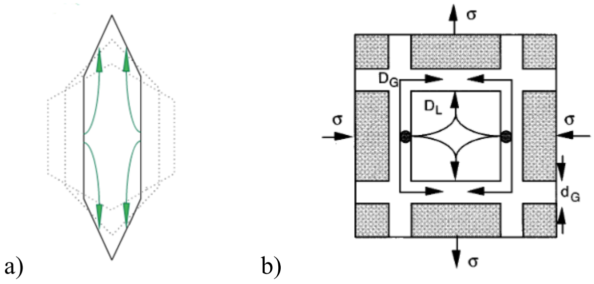

Figure 3-22: Diffusional creep mechanism: (a) Nabarro-Herring creep; (b) Coble creep[146].

Besides purely diffusional mechanisms, steady-state creep in polycrystalline materials can also involve dislocation creep. Dislocation creep is a mechanism involving motion of dislocations. Climb and/or glide of dislocations controls the creep strain rate [147]. This mechanism of creep tends to dominate at higher applied stresses [148].

A third kind of creep mechanism involves grain boundary sliding. This mechanism dominates the creep process for some ceramics containing glassy phases. The softening of these phases at high temperature allows creep to occur by grain boundary sliding, actually, the glass viscosity controls the creep rate in this case [143].

Because creep mechanisms depend on stress, temperature and different creep mechanisms may dominate in different cases, such as different temperatures and stress regions. Forst and Ashby compiled the information into a deformation mechanism map [148], as shown schematically in *Figure **3**-**23***. Besides stress and temperature, the grain size effect needs to be considered as well. Generally, smaller grains cause faster creep due to the associated shorter diffusion paths [143].

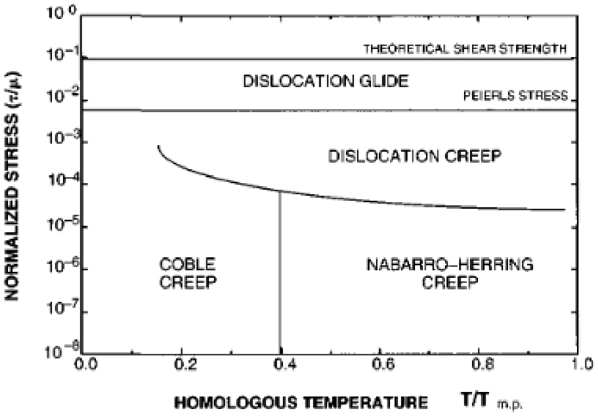

Figure 3-23 : Creep deformation map for a polycrystalline material [148].

To quantify the creep rate and identify the predominant creep mechanism, a single equation was suggested as a power law or an exponential function of stress. Norton and Bailey [149] proposed the relationship:

$$\dot{\varepsilon} = A \cdot \sigma^n \tag{3-10}$$

where A and n are stress-independent constants. Since all mechanisms of steady-state creep are in some way dependent on diffusion and thermally activated process, the temperature dependence of the creep rate can be expressed as Arrhenius law [150] [151]:

$$\dot{\varepsilon} = A \cdot \sigma^n \cdot exp(-\frac{Q}{RT}) \tag{3-11}$$

where R is the universal gas constant, Q a characteristic activation energy.

The stress exponent n depends on the actual operating creep mechanism. For diffusion creep its value is approximately 1, while for dislocation creep it is usually in the range 3-8. The typical n values and their related diffusion mechanisms are listed in *Table **3-3***. Although n and Q are expected to be constant for one material, changes of the creep mechanism might occur and lead to discontinuities in the $\varepsilon - \sigma$ or $\varepsilon - 1/T$ curve [152].

Table 3-3: Creep exponents and diffusion paths for various creep mechanisms [143].

Creep mechanism	*n*	Diffusion path
Dislocation creep mechanisms		
Dislocation glide climb, climb controlled	4-5	Lattice
Dislocation glide climb, glide controlled	3	Lattice
Dislocation of dislocation loops	4	Lattice
Dislocation climb without glide	3	Lattice
Dislocation climb by pipe diffusion	5	Dislocation core
Diffusion creep mechanisms		
Vacancy flow through grains	1	Lattice
Vacancy flow through boundaries	1	Grain boundary
Interface reaction control	2	Lattice/ Grain boundary
Grain boundary sliding mechanisms		
Sliding with liquid	1	Liquid
Sliding without liquid (diffusion control)	1	Lattice/grain boundary

(2) Bending tests

Cell materials for SOFCs are nowadays normally produced by tape-casting to obtain thin layers. This shape of the materials makes it difficult to carry out compressive or tensile creep test. Hence, flexure bending tests, such as four-bending test are considered as an effective method to study the creep of ceramics [153]. They are easy to perform and avoid problems of alignment and fixing for the brittle materials. However, creep deformation can be different in tension and compression leading to problems in deriving creep data of ceramics from bending tests.

Hollenberg *et al.* [154] derived a relationship between creep strain and loading-point deflection for steady-state creep with the assumption that the neutral axis passed through the centre of cross-sectional area of the specimen. Snowden and Mehrtens [155] modified the expression related to the center deflection of specimen, which made the data analysis and experiment measurement more simple and convenient. *Figure* ***3-24*** shows the geometry of the partly circular bending.

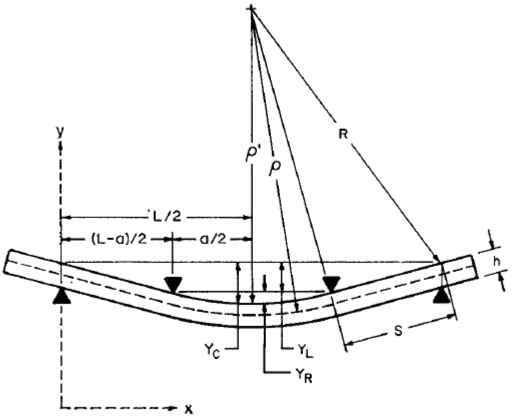

Figure 3-24: Schematic of the partly circular bent beam [156].

The strain ε_c at the center of beam and the relation between the strain ε_m in the outer beam and the load-point deflection, respectively, can be expressed as [154, 156] :

$$\varepsilon_c = \frac{-h}{\left(\frac{n}{n+2}\right)\left(\frac{L-a}{2}\right)^2 - \frac{L^2}{4}} \cdot y_c \tag{3-12}$$

$$\varepsilon_m = \frac{2h\,(n+2)}{(L-a)[L+a(n+1)]} \cdot y_L \tag{3-13}$$

where y_c , y_L are the deflection of beam center and deflection of the loading point, respectively; h is the thickness of the specimen; L the distance between the outer supports and a is the inner span.

Equation (3-10) is symmetric with respect to the sign of the applied stress, implying the creep behavior should be the same in uniaxial tension or compression [143]. This has been confirmed for several single-phase materials, it is not always true in the case of two-phases or multi-phase materials [157]. Lange [158] showed that polycrystalline materials, such as Si_3N_4, exhibit a much greater rate of deformation in tension than in compression. Therefore the assumption in analyzing bending test data with respect to the location of the neutral axis of the specimen might not always be correct and can shift slightly during the test. However, it will be very difficult to ascertain the neutral axis accurately [157]. Although this inaccuracy aspect exists, the bending test still provides valuable information for the real applications, especially for the SOFC in the complex stress field of the stack environment.

3) Porosity and multi-phase effects

Since ceramic and ceramic composites are considered for high-temperature applications, optimal mechanical properties, such as creep resistance, are crucial. The creep resistance of ceramics materials can be enhanced considerably by the addition of second phases [146, 159]. It was assumed that a duplex microstructure can be simplified to iso-strain and iso-stress models (*Figure **3-25***), where the strain and strain rates are the same for each phase or where the stress is the same in each phase, respectively [159]. However, these ideal models don't fit properly for all materials. Wilkinson introduced more models for creep in multi-phase ceramic such as the Rheological model [146].

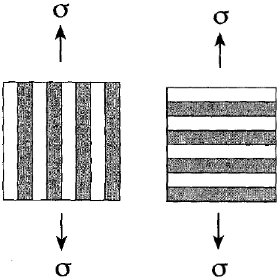

Figure 3-25: The idealized composites microstructure: (a) iso-strain and b) iso-stress orientations [159].

Previous researchers proposed few models to analyze the creep behavior of porous materials. Rice [160] proposed a model based on minimum solid area. All pore structures are considered to be able to be obtained by varying degrees of bounding of various particles and packings. This model is based on regularly stacked spherical particles by point contact, therefore it limits the porosity of model which has to be smaller to 50%. Gibson and Ashby [161] performed an analysis based on cellular solids. They considered the solid material as cell with walls (*Figure*

3-26). When loaded at elevated temperature, the inclined cell walls were deformed via creep bending. Their equation for the creep of open-cell foams can be expressed as [161]:

$$\dot{\varepsilon} = \frac{0.6}{(n+2)}\left(\frac{1.7(2n+1)}{n}\right)^{n} P^{-(3n+1)/2}\, A\, \sigma^{n} exp(-\frac{Q}{RT}) \tag{3-14}$$

where P is the porosity and n the stress exponent.

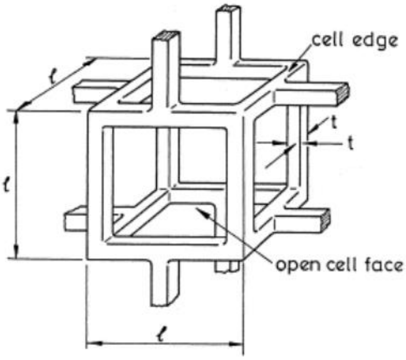

Figure 3-26 : An open-cell foam in the Gibson and Ashby model [161].

Mueller et al. [162] assumed a linear relationship of the elastic moduli between the foam and dense material based on microcellular model. With this linear relationship of the elastic moduli, the creep rate of a foam was linked to the porosity [44]. The creep rate according to this model can be expressed as a function of porosity [162] as:

$$\dot{\varepsilon} = F^{-(1+n)/2} \cdot (1-P)^{(1-n)/2} \cdot A\sigma^{n} exp(-\frac{Q}{RT}) \tag{3-15}$$

$$F = {}^{E}/_{E_0} = f(P) \tag{3-17}$$

where F is the function of porosity, which is related to the elastic modulus of porous (E) and dense (E_0) material.

Focusing onto porous SOFC anode material, Kwok et al. [163] derived two analytical models for the creep rate of porous bodies by extending the Hashin-Shtrikman bound and Ramakrishnan-Arunchalam model. Hashin-Shtrikman [109] analyzed the bounds between two different phases in a porous materials, while the Ramakrishnan-Arunchalam model [112] assumed the hollow spheres as the structure of porous materials. The joined Hashin-Shtrikman / Ramakrishnan-Arunchalam creep respectively model can be expressed as follows:

$$\dot{\varepsilon} = (\frac{12}{12 + 11\,P})^{-(n+1)/2}\,(1 - P)^{-n}\,A\sigma^{n}exp(-\frac{Q}{RT}) \tag{3-17}$$

$$\dot{\varepsilon} = (\frac{2}{2 +\,P})^{-(n+1)/2}\,(1 - P)^{-(3n+1)/2}\,A\sigma^{n}exp(-\frac{Q}{RT}) \tag{3-18}$$

3.4.5. Mechanical properties of anode-relevant materials

3.4.5.1. Elastic properties

The elastic moduli of cell layers are also considered as important parameters for analysis and simulations of stress states. Literature data for elastic moduli of typical cell layer materials are summarized in *Table **3-4***.

Table 3-4: Elastic moduli of typical SOFC materials.

Layers	Material	Porosity (%)	Test method	Elastic modulus (GPa)			Ref.
				RT	600°C	800°C	
Electrolyte	8YSZ	~ 0%	Impulse excitation	190		157	[164]
	8YSZ	~2%		205			[165]
	3YSZ	~0%		190	113		[166]
	YSZ	~0%	Nano-indentation	224			[167]
Anode support	NiO-3YSZ	~11%	Impulse excitation	155			[168]
		~30%		80			
		~16%	Slender cantilever beam	136			[139]
	Ni-8YSZ	~45%	Impulse excitation	45		24	[103]
		~40%		55			[169]
		~24%	Nano-indentation	110			[170]
	NiO-8YSZ	~27%	Impulse excitation	74		68	[103]
		-	Nano-indentation	219			[170]
Cathode	LSM	~30%	Impulse excitation	41			[165]
		~3%		108		98	
	LSCF	~25%	Nano-indentation	91			[171]
Buffer layer	GCO	~3%	Impulse excitation	201			[105]

Impulse excitation has been used in most of the studies to investigate elastic modulus, since the value obtained from indentation test might be significantly influenced by the indentation region, due to porous structure and substrate effects [167, 172].

Previous studies reported the elastic modulus as a function of temperature for typical cell materials [103, 164]. Bause [103] reported the temperature dependency of 8YSZ and Jülich anode materials in reduced and oxidized state (*Figure **3-27***). The observed behavior of 8YSZ can be divided into three regions. The elastic modulus decreased first (slowly in the region from RT to around 200°C, faster from 200 °C), until around 550 °C a minimum value of ~ 135 GPa was reached. For the Jülich anode material (warm-pressed, 1.5 mm thick), an elastic modulus for the oxidized state of 74 GPa and for the reduced state of 45 GPa were measured at room temperature. The elastic modulus in the oxidized state as function of temperature increased slightly first, until a maximum value of 77 GPa reached at 250 °C. With the increasing temperature, the values decreased linearly again. The maximum value at 250 °C was associated to the microstructure transition of NiO from trigonal to cubic. The elastic modulus showed a rather linear behavior with temperature for the reduced state.

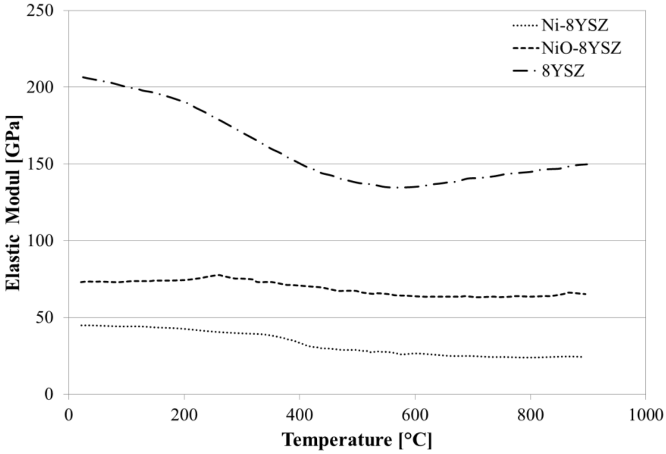

Figure 3-27: Elastic moduli of 8YSZ and Jülich's anode materials obtained from impulse excitation tests [103].

Selcuk and Atkinsion [105] reported the effect of porosity on the elastic modulus of NiO-8YSZ anode materials at room temperature, see *Figure **3-28***. The elastic modulus decreased with increasing porosity. Radovic and Lara-Curzio [169] also studied the changes in elastic modulus of YSZ-containing Ni-based anode materials as a function of the amount of reduced NiO. It was found that elastic modulus decreased significantly with increasing fraction of reduced NiO amount.

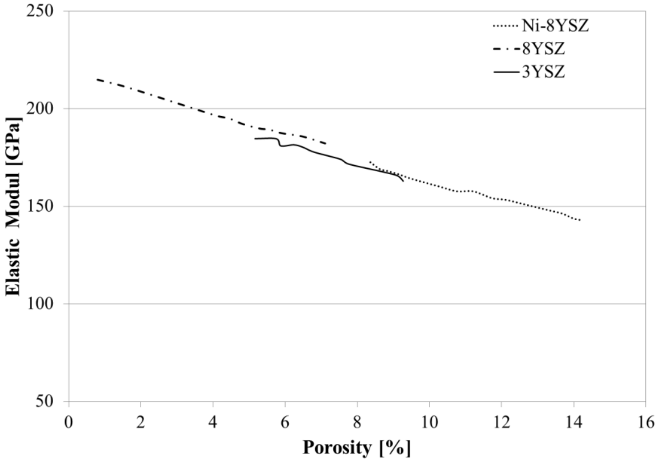

Figure 3-28 : The relationship of porosity and elastic modulus at room temperature for typical SOFC materials [105].

3.4.5.2. Fracture toughness

Fracture toughness of the anode material and other SOFC components plays an important role for designing an SOFC stack as it has to withstand high stresses, arising from a mismatch in thermal expansion coefficients of the different ceramic layers as well as metallic components and thermal gradients during the operation. As already mentioned in previous chapters, porous NiO-YSZ and its reduced state cermet are usually being used as anode material for SOFC applications. Data concerning fracture toughness of the anode materials are still limited. Some fracture toughness values of SOFC components tested using different methods are given in *Table **3-5***.

Table 3-5: Fracture toughness of typical SOFC ceramics.

Material	Testing method	Porosity (%)	Temp. (°C)	K_{Ic} (MPa m^{½})	Ref.
NiO-8YSZ	DT	~14%	RT	2.1 ± 0.2	[137]
		~22%		1.6 ± 0.2	
Ni-8YSZ	DT	~27%	RT	3.4 ± 0.2	[137]
		~40%		2.3 ± 0.5	
NiO-3YSZ	DCB	~16%	RT	2.0 ± 0.1	[138]
	SCB	~16%	RT	2.1± 0.3	[139]
YSZ	DT	~0%	RT	1.6 ± 0.1	[173]
	Indentation	~0%	RT	1.8 ± 0.2	[173]

As introduced in the last section, porosity affects the elastic properties of anode-relevant materials, see for example Selcuk and Atkinson [105], where similar porosity effects were found for fracture toughness. Radovic and Lara-Curzio [137] reported on the porosity influence on fracture toughness of NiO-8YSZ and Ni-8YSZ based on DT test data. *Figure **3-29*** gives the fracture toughness of oxidized and reduced anode materials as a function of porosity. Both materials revealed decreasing fracture toughness with increasing porosities. Ni-8YSZ yielded larger fracture toughness values compared to oxidized state since the deformed Ni phases appeared to bridge the crack surfaces [137]. The porosity influence was also found in fracture strength data [173].

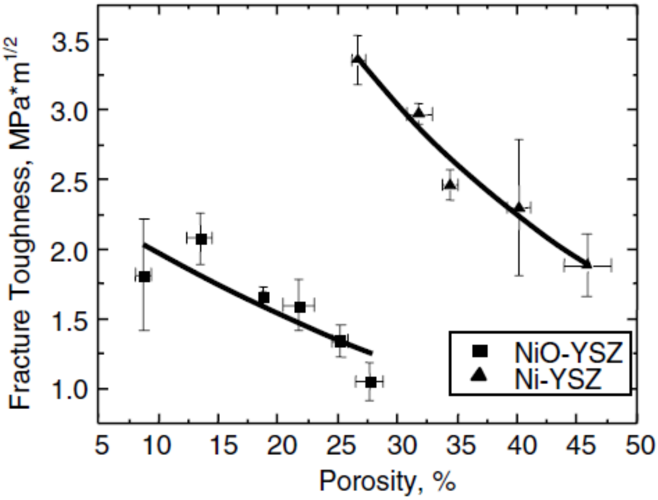

Figure 3-29: Fracture toughness of NiO-8YSZ and Ni-8YSZ as a function of porosity [137].

Besides the DT test, the fracture toughness of anode-relevant materials has also been investigated by other testing methods. Goutianos et al. [138] reported the fracture toughness and critical energy-release rate of anode material (NiO-3YSZ) from DCB tests. The necessity of the pre-crack was discussed in their work, where the fracture energy of a pre-cracked specimen appeared to be lower than the corresponding values from a specimen with blunted notch. A fracture toughness of 1.97 MPa m½ [138] was obtained from the RT test on NiO-3YSZ, which is higher than 1.74 MPa $m^{½}$ derived by Radovic and Lara-Curzio [137] for the corresponding fracture toughness of NiO-8YSZ with 15% porosity. Vandeperre et al. [139] determined the fracture toughness using slender cantilever beams (SCB). In their work the fracture toughness of Ni-3YSZ anode support (16.2 ± 0.1% porosity) was determined to be 2.13 ± 0.27 MPa $m^{½}$.

As well known, pure ZrO_2 normally is doped with other oxides to obtain a fully or partially stabilized tetragonal and/or cubic phase. Since the highest electrical conductivity of ZrO_2 is obtained by doping with 8 mol% yttria [174], this composition is the most commonly used material as the electrochemical active anode, and is hence also often used as composite in the anode substrate. The cubic phase in 8YSZ based anode is rather stable at RT and high temperature. On the other hand, the highest fracture toughness of ZrO_2 is achieved by doping with 3 mol% yttria [175], leading to its use as anode substrate material [176]. In the case of 3YSZ, the tetragonal phase is stable down to room temperature and in a crack-growth associated stress state a transformation to monoclinic phase occurs [175]. This martensitic transformation is accompanied by a volumetric change and leads to large shear strain and local compressive stresses, which finally results in higher fracture toughness, a property of main concern for all fracture mechanics based approaches. This effect is termed as the transformation toughening of YSZ materials [177]. *Figure **3-30*** shows the three different phase structures of ZrO_2.

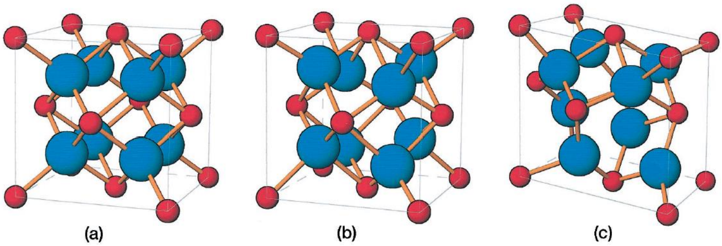

Figure 3-30: Schematic representation of the three polymorphs of ZrO_2 and the corresponding space group: (a) cubic, (b) tetragonal, and (c) monoclinic [178].

The change of fracture toughness at application-relevant temperatures also depends on the phase composition. In case of pure 3YSZ, it was reported that fracture toughness decreases with temperature, since the effect of the t-m transformation vanishes above 450°C [179]. While the fracture toughness of 8YSZ should remain rather constant since no phase change is expected to occur for this material. Both effects need verification for anode substrate materials. The previous works have focused on the fracture toughness at RT, in the current study, the fracture toughness' of oxidized and reduced specimens were investigated at RT and operation relevant high temperatures.

3.4.5.3. Creep behavior

Laurencin et al. [140] did a creep analysis on Ni-8YSZ using 4-point bending test at elevated temperatures. The obtained creep parameters are listed in *Table **3-6***. In their work, Ni-8YSZ exhibits substantial creep strain rates even at relatively low temperatures (700-850 °C). The obtained creep exponent ($1 < n < 2$) suggests that the creep mechanism has to be ascribed to a diffusional process.

Table 3-6: Creep parameters of the power law model determined by 4-point bending test on Ni-YSZ cermet [140]. Note the pre-exponent has different definition in reference data.

Temperature (°C)	Pre-exponent (s^{-1} MPa^{-n})	Stress exponent, n	Activation energy, Q (kJ mol^{-1})
750	$7.2 \cdot 10^{-11}$	1.1	-
800	$2.6 \cdot 10^{-11}$	1.7	-
700 - 850	-	-	115

Morales-Rodriguez et al. [180] reported the creep properties of Ni-3YSZ with 20 and 40 vol. % Ni using compressive creep tests at temperatures ranging from 950°C to 1250°C in reduced atmosphere. Similar values of the stress exponent n and the activation energy Q were found for the materials containing different Ni amounts. At 1200-1250°C under stresses ranging from 3 to 14 MPa, average values of $n = 4.0 \pm 0.4$ and $Q = 610 \pm 20$ kJ/mol were obtained for the materials with 20% Ni cermet, while average values of $n = 3.9 \pm 0.1$ and $Q= 640 \pm 50$ kJ/mol were obtained for the materials with 40 % Ni. The material with higher Ni amount yielded higher creep rates than the material with lower Ni amount. Both creep parameters decreased with increasing stress and/or temperature, showing a similar trend as for high-purity monolithic YSZ [180]. The studies [140, 180] based on Ni-3YSZ and Ni-8YSZ reported the similar conclusion, that the overall creep behavior of the composites is primarily controlled by the ceramic matrix phase

With respect to this matrix phase controlled effect on creep [180], Kwok et al. [44] applied three-dimensional (3D) microstructural simulation on porous Ni-YSZ materials. 3D image data of the specimen were acquired by FIB, see *Figure **3-31***. The results shown in *Figure **3-32** (a)* indicate that the creep rate of the Ni is faster than that of 3YSZ and 8YSZ by 9 and 7 orders of magnitude, respectively. The similar strain rates (*Figure **3-32** (b)*) of porous Ni-8YSZ and porous 8YSZ indicated that the YSZ phase is essentially carrying most of the applied load. Experimental tests were carried out in the current work to verify these conclusions.

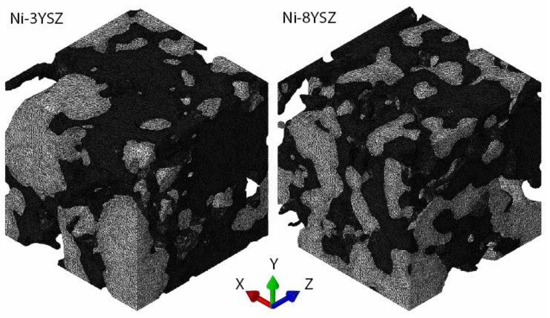

Figure 3-31: Finite element mesh of reconstructed microstructures. The Ni and YSZ phases colored white and grey, respectively [44].

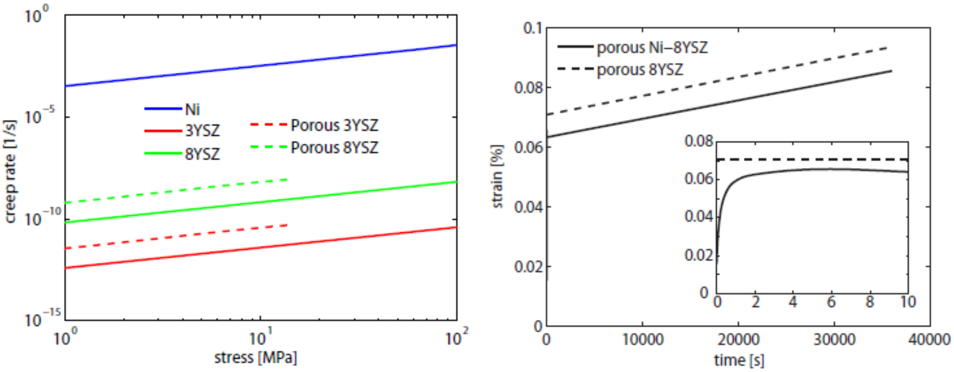

Figure 3-32: (a) Creep rate of Ni, 3YSZ and 8YSZ at 800°C for the relevant stress range; (b) volume-averaged strain in the loading direction [44].

If pores are present, the measured creep rate should differ from that of a theoretically dense material. Due to the pores the effective stress is larger than the applied stress. It has been reported for example in [181, 182] that the steady-state creep rate of polycrystalline ceramics (e.g. Li_2O-ZnO-SiO) increases with increasing porosity.

In this work, different loading configurations were applied to assess the influence on creep behavior of materials, considering also porosity and Ni/YSZ composition effects.

3.4.6. Mechanical properties of sealants

3.4.6.1. Elastic properties

During recent years glass-ceramics of the $BaO\text{-}CaO\text{-}SiO_2$ system were mostly used in SOFC stack assembling [65]. Elastic moduli of various sealant materials were investigated and discussed in previous studies [49, 65, 82, 83, 118]. *Table **3-7*** compiles the data along with the corresponding testing temperature and method.

Table 3-7: Elastic moduli of typical SOFC sealant materials.

Glass-ceramic sealant	Specimen	Conditions	Test method	Elastic modulus (GPa)	Ref.
GC-9 $BaO\text{-}SiO_2\text{-}B_2O_3\text{-}Al_2O_3, ZrO_2, La_2O_3$	Bars	As-sintered	4-points bending	66 ± 8	[183]
		Annealed		68 ± 6	
	plate	As-sintered	Ring-on-ring	18 ± 6	[184]
		Annealed		19 ± 4	
H $BaO\text{-}CaO\text{-}SiO_2$, doped with Al_2O_3, B_2O_3, V_2O_5, ZnO	Bars	As-sintered	Micro-indentation RT	72 ± 5	[83]
		Annealed		80 ± 9	
B $BaO\text{-}CaO\text{-}SiO_2\text{-}Al_2O_3$	Bars	As-sintered	Micro-indentation RT	77 ± 3	[83]
		Annealed		77 ± 3	
	Joined	As-sintered		86 ± 3	
H-P Glass H + 20 wt % YSZ particles	Sintered bars	As-sintered	Micro-indentation RT	73 ± 8	[83]
		Annealed		79 ± 6	
	Joined bars	As-sintered		80 ± 15	
	Stack	800°C for 1056 h		70 ± 12	[49]
		800°C for 19000h		100 ± 10	
	Bars	As-sintered	Impulse excitation	~ 45	[65]
			4-points bending	~ 40	
H-Ag Glass H + 20 wt % Ag particles	Bars	As-sintered	Micro-indentation RT	75 ± 5	[83]
		Annealed		74 ± 8	

An influence of testing methods the data was found in previous studies [65, 118]. Zhao at al. reported different elastic modulus values [65] obtained from three testing methods on so-called

H-P and B sealants, as shown in *Figure **3-33***. The results indicated a strong influence of the local morphology on the indentation test. Compared to the global values determined from bending and impulse excitation tests, the indentation test appears to be much more sensitive to porosity and homogeneity of the material. For a rather dense sealants such as the B glass-ceramic (almost non-porous), the different testing method yielded fairly similar results, while for a porous sealant such as H-P and H-Ag, the disagreement was quite obvious. Chang et al. [183] also obtained different values of elastic modulus for their GC-9 sealant using 4-points bending and ring-on-ring test. They associated this difference to pores and defects that were associated with different specimen preparation [183]. The relationship between elastic modulus and increasing temperature has been discussed in their work for GC-9, indicating that the elastic modulus drops above 700°C. For the H matrix based sealants, the temperature dependency of elastic modulus was also investigated, which is discussed in detail in [65].

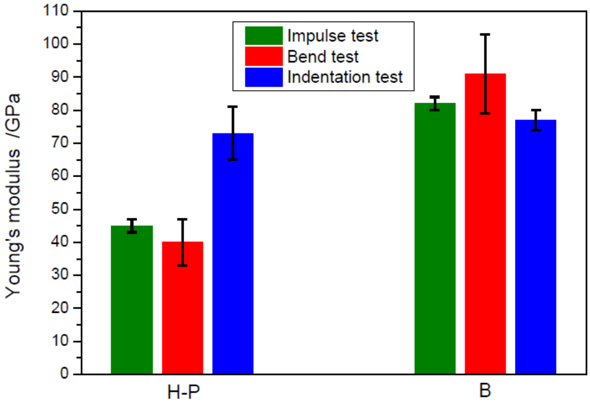

Figure 3-33: Comparison of elastic moduli obtained using different testing methods [65].

3.4.6.2. Fracture stress (Bending stress)

The fracture stress values of sealant materials similar to that considered in the present work are summarized in *Table **3-8***. Zhao [65] used bar-shaped and joined specimens to obtain the fracture stress of Jülich B and H-P type sealants by using 4-points bending test. The joined specimens are aimed to mimic the real case in the stack, by which much lower bending fracture stresses were obtained than in the case of sintered bars. Also sealant thickness effects were found for joined H-

P sealant specimens, i.e. the facture stress decreased with increasing thickness. Plenty of previous work [82, 136, 183, 184] reported that crystallization shows a positive effect on fracture stress of partially crystallized glass-ceramic sealants, while the growth and coalescence of micro-voids and micro-cracks during the annealing can noticeably degrade the strength such as reported for the GC-18 sealant [185].

Instability issues might occur at operation relevant temperatures due to viscoelastic deformation of the residual glass phase. Most partially crystallized glass-ceramic sealants, such as H, H-P, GC-9, GC-18 show a non-linear behavior close to the glass transition temperature, while fully crystallized sealants (such as B sealant) showed relative stable fracture stress at elevated temperature.

Table 3-8: The fracture strength of the typical sealant materials.

Glass sealant	Specimen	Conditions	Test method	Temp. (°C)	Fracture strength (MPa)	Ref.
H BaO-CaO-SiO$_2$, doped with Al$_2$O$_3$, B$_2$O$_3$, V$_2$O$_5$, ZnO	Joined	As-sintered	4-point bending	RT	52 ± 1	[83]
				800	~1	
B BaO-CaO-SiO$_2$-Al$_2$O$_3$	Bulk bars	As-sintered	4-point bending	RT	91 ± 12	[83]
				800	~ 90	
	Joined	As-sintered		RT	25 ± 2	
H-P Glass H + 20 wt % YSZ particles	Bulk bars	As-sintered	4-point bending	RT	28 ± 3	[83]
				800	~ 1	
	Joined bars	As-sintered		RT	22 ± 2	
				400	30 ± 5	
				800	~1	
		800°C for 500 h		RT	47 ± 3	[49]
				800	~41	[65]
GC-9 BaO-B$_2$O$_3$-SiO$_2$-Al$_2$O$_3$	Bulk bars	As-sintered	4-point bending	RT	63	[184]
				750	4.5	
		Annealed		RT	73	
	Plate	As-sintered	Ring-on-ring	RT	57 ± 10	[183]
				800	27 ± 6	
		Annealed		RT	56 ± 6	
				800°C	48 ± 7	
GC-18 BaO-CaO-SiO$_2$-Al$_2$O$_3$	Bulk bars	As-sintered	4-point bending	RT	80 ± 10	[185]
				800	39 ± 4	
		Annealed		RT	43 ± 3	
				800°C	30 ± 2	

3.4.6.3. Shear stress

The shear stresses of sealant materials similar to that considered in the present work are summarized in *Table **3-9***. Schwickert [124] reported the shear stress of Glass 58, which is based on BaO-CaO-Al2O_3-SiO_2 and joined with steel 1.4742. The shear stresses are in a range of 8.6-10.5 MPa. Nielsen [186] characterized the glass NAS based on Na_2O-Al_2O_3-SiO_2 with 30% MgO fillers using similar joined specimens. The shear stress is around 1.87 ± 0.24 MPa. The mechanism of these testing methods is very similar to the lap-tests, where the applied load is paralleled to the joined cross-section.

According to the results of KMBY sealant, the cross-bonded configuration (ISO13124, se *Figure **3-14** (c)*) is subjected to combined shear, tensile and bending stresses, as typically occurs with lap-tests [187, 188]. The apparent shear strength is much lower than 71 MPa obtained by the torsion test [189], where a pure shear strength can be obtained. The torsion test has suggested to be the most reliable method to measure the pure shear strength of glass-ceramic joined specimens for SOFCs application. Previous works mostly focused on the (apparent) shear stress at room temperature. A shear test technique at high temperature was developed by Lin et al. [190]. Glass GC-9 was tested at room temperature and 800°C to measure shear joint stress by a sealant-metal jointed shear test specimen (similar as *Figure **3-15** (a)*). For sealant GC-9 with 250 h or 500 h it appeared that shear joint strength decreases at 800°C by 17 % due to continuous growth of $BaCrO_4$ chromate.

In the current work, an improved torsion set-up has been developed for room and elevated temperatures. The pure shear stress of different sealants for SOFC application was investigated and will be discussed in the latter sections.

Table 3-9: The sealants tested by different shear tests.

Glass sealant	Specimen	Conditions	Test method	Temp. (°C)	Fracture strength (MPa)	Ref.
Glass 58 $BaO-CaO-SiO_2-Al_2O_3$	Joined	As-sintered	Joined shear	RT	8.6-10.5	[124]
NAS $Na_2O-Al_2O_3-SiO_2$ with 30% MgO fillers	Joined	As-sintered	Joined shear	RT	1.87 ± 0.24	[186]
GC-9 $BaO-B_2O_3-Al_2O_3-SiO_2$, CaO, La_2O_3 ZrO_2	Joined	As-sintered	Joined shear	RT	4.9-6.6	[190]
				800°C	4.4-4.7	
KMBY SiO_2, CaO, Al_2O_3,Na_2O, B_2O_3, Y_2O_3, K_2O	Joined	As-sintered	Torsion	RT	71 ± 5	[189]
			ISO13124		42 ± 6	

4. Experimental

4.1. Materials

4.1.1. Anode substrate materials

Two anode substrate compositions were analyzed, NiO-3YSZ anode substrates were produced by Topsoe Fuel Cells (TOFC, Denmark) and NiO-8YSZ half-cells (anode substrate with anode functional layer and electrolyte) at IEK-1 (Forschungszentrum Jülich GmbH, Germany). Due to confidentiality, the production procedure of NiO-3YSZ cannot be described here and only the production of Jülich substrates is given in detail.

(1) Fracture toughness - Double torsion specimen

The TOFC material was produced by tape casting [191]; further details on powders and production cannot be given due to confidentiality. The specimens produced at IEK-1 were either warm pressed (type 2) or tape cast (type 3 and 4), along with an additional very thin functional anode and electrolyte layers (10 to 20 µm each). The raw materials used for substrate, anode and electrolyte were NiO from Mallinckrodt Baker (Griesheim, Germany), 8 mol% yttria-stabilited zirconia (8YSZ) from USM (FYT13-H-5, Laufenburg, Germany), and 8YSZ from Tosoh (TZ-8Y, Tokio, Japan). The detailed production procedure can be found in [22] and [20]. The NiO-8YSZ material was reduced to Ni-8YSZ in 4% H_2/Ar at 900°C for 5 h. A re-oxidation test was carried out via heating in air to 800 °C with the heating rate of 8 K/min.

All specimens were supplied with dimensions of 40 × 20 mm², with a laser cut notch of a length of 14 mm and a width of 0.7 mm (see *Figure **4-1***). TOFC´s NiO-3YSZ specimens were 300 µm thick, while the Jülich specimens of type 2 were 1000 µm thick and type 3 and type 4 were 500 µm thick. Specimen details are given in *Table **4-1***.

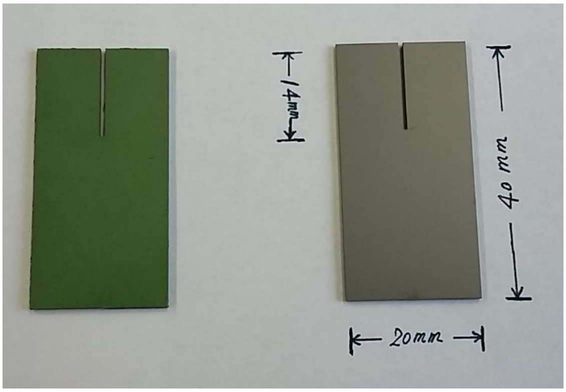

Figure 4-1: Specimens for double torsion test. The left is the oxidized anode material, while the right is in reduced state.

Table 4-1: Double torsion tests: Investigated materials.

Material	Type	Production	Thickness (µm)	Porosity (%)
NiO-3YSZ	Standard	Tape casting	328 ± 11	14 ± 1
NiO-8YSZ	2	Warm pressing	1018 ± 60	22 ± 1
	3	Classical tape casting	525 ± 18	16 ± 1
	4	Sequential tape casting	545 ± 16	13 ± 1

(2) Creep specimen

The creep investigation was only carried out on pure Ni-8YSZ anode substrate produced by IEK-1, Jülich, since TOFC material was not available in suitable geometries. The surfaces of the bar-shaped specimens were ground and polished before the compression test to ensure flatness and parallelity. Before testing, the initially oxidized specimens were again reduced at 900°C in 4 % H_2/Ar atmosphere for 5 h. Porosities of the different specimen types were determined graphically with the software package AnalySIS (details in section 4.2.1). Details on the tested Ni-8YSZ materials abbreviated as A, B, C and D, are given in *Table **4-2***.

Table 4-2: Ni-8YSZ materials tested with respect to creep

Ni-8YSZ	Porosity (%)	YSZ (wt %)	Producing process	Specimen geometry
A	20 ± 1	~49%	Warm pressed	Bar: 3 × 3 × 9 mm^3 Plate: Ø 22 mm × 1.3 mm
B	30 ± 2	~48%	Tape casting	Plate: Ø 22 mm × 0.5 mm
C	46 ± 1	48~55%	Warm pressed	Plate: Ø 36 mm × 1.5 mm Beam: 5.5 × 1.5 × 36 mm^3
D	50 ± 5	~37%	Warm pressed	Plate: Ø 25 mm × 1mm

The bar-shaped specimens were tested in compression. Bending creep tests were carried out on plate-shaped specimens using a ring-on-ring set-up and on beam specimens using four-point bending. The testing temperatures ranged from 800°C to 900°C. All tests were carried out in 4% H_2/Ar atmosphere to avoid oxidation during the elevated temperature test.

4.1.2. Sealant materials

The studied composite sealant is based on a glass matrix called glass “H” of the BaO-CaO-SiO_2 ternary system, with small amounts of Al_2O_3, B_2O_3, V_2O_5 and ZnO [192]. The filler materials added to the matrix was either 20 wt.% Ag particles or 13 wt.% YSZ fibers, subsequently abbreviated H-Ag and H-F, respectively. The raw materials were obtained from Merck KGaA Darmstadt with purity higher than 99 %. Each batch was prepared by mixing an appropriate mole fraction of oxide ingredients and melting at 1480 °C in a platinum crucible in an induction furnace. For better homogenization of the glass, the melting procedure was carried out twice. For making the powder, the frits were wet-milled in acetone in an agate ball mill to a medium particle size of 10 - 13 μm, dried and then sieved through a mesh size of 0.32 μm to collect powders. The chemical composition of the sample was analyzed by inductively coupled plasma optical emission spectroscopy (ICP-OES) [83], see *Table **4-3***. Powders were blended to paste using ethyl cellulose as binder in terpineol (18wt. %) for the screen printing.

Table 4-3: Chemical composition of sealant material H-Ag and H-F.

In wt.%	BaO	SiO_2	CaO	Additions	Filler
H-Ag	48.2	29.8	6.1	Al_2O_3, B_2O_3, V_2O_5, ZnO	20 wt.% Ag particle
H-F					13 wt.% YSZ fiber

Some sealant materials from Ceramics and Glass Institute (CSIC), Madrid, Spain, were also tested in this work, so called 7.5 B (Ba) and 10 B (Sr). The composition of sealants is given in *Table **4-4***. The raw materials are SiO_2 (Saint-Gobain), MgO (Panreac), $BaCO_3$ (Alfa Aesar), $SrCO_3$ (Alfa Aesar) and B_2O_3 (Alfa Aesar), which all have more than 90 % purity. The B_2O_3 powders (Alfa Aesar) were melted previously in a gas furnace at 900°C to obtain a glass, thus avoiding the hygroscopy of the B_2O_3 powder. The raw materials used for preparation of the glasses were mixed in a tubular mixer during one hour before calcination at 1250°C in an electrical furnace using a covered Pt/Rh crucible and subsequently melted at 1550°C for 2 h. The batch was melted twice in order to obtain a better glass homogeneity. The molten glass was poured into water and the glass frits were dried at 100°C.

Table 4-4: Chemical composition of sealant material 7.5 B (Ba) and 10B (Sr).

In mol.%	SiO_2	BaO	SrO	MgO	B_2O_3
7.5 B (Ba)	47.5	27	-	18	7.5
10 B (Sr)	45	-	27		10

(1) Fracture stress – sintered bar

The determination of the fracture stress for sintered bars concentrated on the ICV-CSIC (in Madrid, Spain) material since previous investigations [65] indicated that for the Jülich material the data obtained for sintered bars are not representative for the behavior of the material in thin-layer geometry. Bar-shaped 7.5B(Ba) and 10B(Sr) specimens were supplied by ICV-CSIC, Madrid. The stack representative thermal treatment was carried out on 7.5 B(Ba) at 800°C for 24 h and 800 h, on 10 B(Sr) at 750°C for 24 h and 800 h, respectively. The geometry of the specimen was ~45 mm × 5 mm × 4 mm. All specimen surfaces were fine-grinded with 4000-grit abrasive papers before the mechanical tests.

(2) Fracture stress - layers

The so-called head-to-head joined specimens were prepared using an in-house developed sealing jig (*Figure* **4-2.** (*a)*), resulting in a thin-layer geometry similar as in SOFC stacks. Crofer22APU was used as joining partner with surface preparation equivalent to the stack application. The sealant materials were dispensed by screen printing to the steel bar surface. Specimens' dimensions were 50 mm × 6 mm × 4 mm, sealant thicknesses after joining were between 200 ± 15, 250 ± 15 and 350 ± 25 µm. The necessary heat treatment was applied during joining. The as-sintered state corresponds to a holding time of 10 h at 850°C. Heating and cooling rates were 5 K/min. Additional thermal treatments (500h at 800°C for H-Ag or 100h and 1000h at 850°C for H-F) were carried out after joining to achieve a state representative for long term stack operation. The tensile-loaded specimen surfaces were fine-grinded with 4000-grit abrasive papers before the mechanical test. *Figure* **4-2.***(b)* shows a schematic and some real specimens after fine grinding.

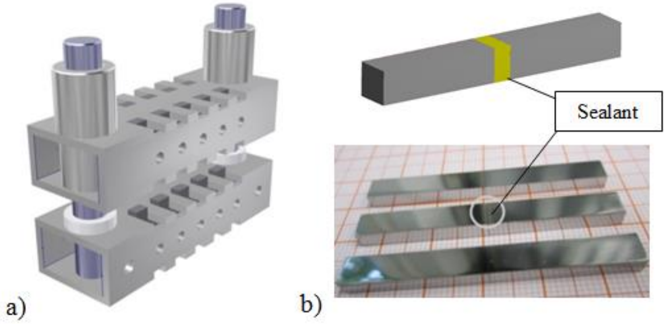

Figure 4-2: (a) In-house joining jig, (b) schematic and actual head-to-head specimens after fine grinding.

(3) Torsion test specimens

Joined plate specimens were designed for the torsion test. Similar as in the case of the head-to-head specimen, two steel plates (Crofer22APU) were joined by screen printed sealants. 4 kg (~40N) load was applied during joining at 850°C for 10 h. The annealed state sealant was prepared with further heating treatment (additional 90 h at 850°C). The dimension of the specimen was ~30 x 30 x 5.5 mm^3 and the diameter of the circular joining region 25 mm. The thickness of sealant layer was ~ 250 mm, corresponding to the typical thickness used in a SOFC stack. *Figure* ***4-3*** presents a schematic and real joined plate specimen.

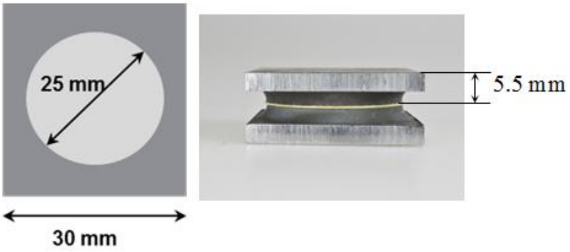

Figure 4-3: Schematic and real joined plate specimen.

4.2. Microstructural characterization

4.2.1. Microscopy

Selected specimens were embedded in epoxy resin and ground with SiC abrasive papers up to 4000 grit. Subsequently, polishing was performed using diamond paste up to 0.25 µm grain size. The microstructure of all materials was investigated using optical microscope (CSM, Switzerland) and scanning electron microscope (LEO 440, Zeiss Merlin, INCAEnergy). Element analysis was carried out using energy-dispersive X-Ray spectroscopy (EDX, Inca, Oxford).

The porosities of the initial NiO-YSZ and the material in the reduced state were investigated. Porosity was graphically analyzed with the ImageAnalysis Pro® software using the planimetric method. The pore percentage was obtained from the ratio of the pore area to the total area of microstructure image. Fractography to assess fracture origins was carried out using stereomicroscope (Olympus SZH10) and scanning electron microscope (LEO 440, Zeiss Merlin, INCAEnergy).

4.2.2 X-ray diffraction

X-ray diffraction is an effective tool for the investigation of the phase transformations. The principle is based on the change of the crystal lattice parameter α. The lattice parameter depends on the atomic species presented in a particular material. The phase analysis in this work was performed by X-ray diffraction using a Siemens D5000 diffractometer, which is equipped with an X-ray tube with copper anode (λ=1.5418 $\dot{A}$). The step scan used Cu-Ka radiation with a step size 0.02° and a step time 5s.

4.3. Mechanical characterization

4.3.1. Fracture toughness

Double torsion tests as an effective method to measure fracture toughness were carried out on various anode materials in this work. The anode materials in oxidized and reduced states were tested at room temperature in air and typical operation temperature (800°C) in a 4 % H_2/Ar atmosphere, respectively. The temperature was monitored close to the outer specimen surface with a thermocouple type K. The specimens were tested in a full ceramic double-torsion (DT) set-up placed in an Instron 1362 machine. Initially the specimens were loaded with 1 N pre-load and further applied the specimen with the controlled constant displacement rates. A schematic image of a DT setup is shown in *Figure **4-4***.

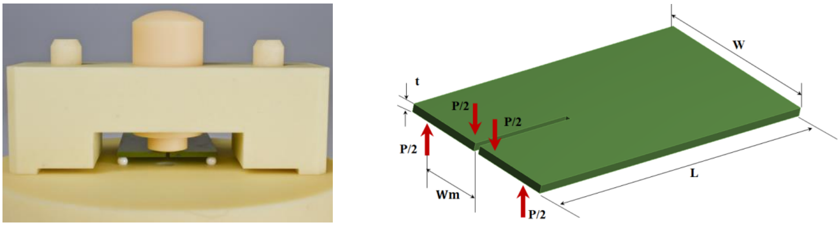

Figure 4-4: Figures of a double-torsion setup and the loading scheme of the specimen.

Fracture toughness was determined in DT testing simply by loading a specimen rapidly and recording the maximum load at failure (F_{IC}). The used fracture toughness calculation formula [193] :

$$K_I = F_{IC} \cdot W_m \cdot \left[\frac{3(1+\nu)}{W \cdot t^4 \cdot \xi} \right]^{1/2} \tag{4-1}$$

$$\xi = 1 - 1.26\left({}^{t}/_{W} \right) + 2.4 \cdot exp\left[{}^{-\pi W}/_{2t} \right] \tag{4-2}$$

where W, L and t are the width, length and thickness of the specimen, respectively, W_m is the moment arm, v the Poisson's ratio, ξ a thickness correction factor.

The list of double torsion tested specimens and corresponding experimental conditions are given in *Table **4-5***.

Table 4-5: Details of double torsion tests.

Material	Type	Number of specimens	Test conditions	Environmental conditions	Analyzed effect
NiO-3YSZ	Standard	3	Pre-crack + 1000 µm/min	RT	Pre-crack
		20	1000 µm/min	RT	Standard
		1	2000 µm/min	RT	SCG
		4	100 µm/min	RT	
		5	10 µm/min	RT	
		3	1 µm/min	RT	
		2	1000 µm/min	800 °C	HT
Ni-3YSZ	Standard	3	Pre-crack + 1000 µm/min	RT	Standard
		3	Pre-crack + 1000 µm/min	800°C	HT
NiO-8YSZ	4	2	1000 µm/min	RT	No pre-crack
	4	5	Pre-crack + 1000 µm/min	RT	Standard
	4	2	Pre-crack + 100 µm/min	RT	SCG
	4	2	Pre-crack + 10 µm/min	RT	
	3	4	Pre-crack + 1000 µm/min	RT	Type
	2	3	Pre-crack + 1000 µm/min	RT	
	4	2	Pre-crack + 1000 µm/min	800 °C	HT
Ni-8YSZ	4	2	Pre-crack + 2000 µm/min	RT	Type
	3	1	Pre-crack + 2000 µm/min	RT	
	2	1	Pre-crack + 2000 µm/min	RT	
	4	1	Pre-crack + 5000 µm/min	RT	SCG
	4	1	Pre-crack + 1000 µm/min	RT	
	4	1	Pre-crack + 100 µm/min	RT	
	4	2	Pre-crack + 2000 µm/min	800°C	HT
	4 re-oxidized	2	Pre-crack + 2000 µm/min	800 °C	Re-oxidation

4.3.2. Creep behavior

4.3.2.1. Compressive test

Compressive creep behavior was analyzed in tests in which bar-shaped (cuboid) specimens were uniaxially loaded between two supports. The tests were performed using an Instron 1362 testing machine. A linear variable differential transducer (Sangamo, LVDT, range ±1 mm, precision 1.25 µm) was used for measuring the vertical displacement. The transformer was assembled with the half-sphere in the clamping device by an alumina rod (*Figure **4-5***). The load was measured by load cells with 10 KN measuring range (1210 BLR, Interface Company). The temperature was monitored close to the outer specimen surface with a thermocouple type K.

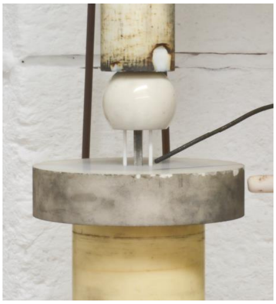

Figure 4-5: Compressive creep test set-up.

The surfaces of the specimen were previously ground and polished to ensure flatness and parallelism. The creep strain was determined by following equation:

$$\varepsilon = \frac{\Delta h}{h_0} \tag{4-3}$$

where Δh is the deformation measured during the test and h_o is the initial height of the specimen. A Norton law (Equation 3-10) was used in current study to obtain creep parameters of materials. By plotting the natural logarithm ln of the steady state creep rate $\dot{\varepsilon}$ against *ln (σ)*, at a constant temperature *T*, *n* is determined as the slope in the plot. The activation energy *Q* was calculated by plotting the *ln* ($\dot{\varepsilon}$) against the reciprocal of the absolute temperature (*1000/T*) at a constant stress.

Tests were carried out on reduced anode bar-shape specimens from 800°C to 900°C under 4 % H_2/Ar to protect the material from oxidation occurring at elevated temperatures. The specimens were heated with a heating rate 8 K/min. The thermal equilibrium was considered to be reached after 1 h dwell time. A variable stresses was applied during the experiments as illustrated in the test scheme in *Table* ***4-6***.

Table 4-6: Compressive creep tests.

Material	Applied stress (MPa)	Temperature (°C)	Number of test	Environmental conditions
Ni-8YSZ (~3 x 3 x 8 mm^3)	30	800	1	H_2/Ar
		850	1	
		900	1	
	63	800	1	
		850	1	
		900	1	
	100	800	1	
		850	1	
		900	1	

4.3.2.2. Bending test

Several types of bending tests were performed using an electromechanical testing machine (Instron 1362). The central displacement was measured with a sensor attached to the tensile loaded sample surface. A ceramic extension rod connected to a linear variable differential transducer (Sangamo, LVDT, range ± 1 mm, precision 1.25 µm) provided the actual displacement. The load was measured with a 1.5 KN load cell (Interface 110 BLR). The set-up permitted measurement from room temperature up to 1000°C. The temperature was monitored close to the outer specimen surface with a thermocouple type K. Two different bending techniques have been used, ring-on-ring test and four-point bending test, for plate- and bar-shaped specimens, respectively. The distinct atmospheres (air or 4% H_2/Ar) were varied according to the measurement requirements.

(1) Ring-on-ring bending test

The technique is based on the bending of a thin circular (or rectangular) plate-shaped specimen. A loading ring bends the specimen vertically constrained by a supporting ring (*Figure* ***4-6***). A half-spherical connection gear was used to avoid the misalignment during the force transfer.

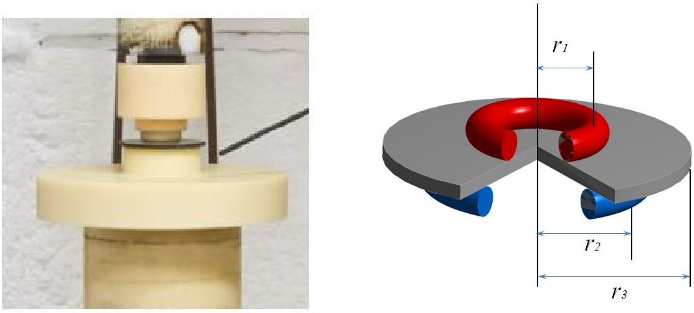

Figure 4-6: Ring on ring test set-up and schematic illustration of a ring-on-ring bending test.

The measurement procedure followed the DIN 51105 standard. Assuming that the creep mechanism is dominated by diffusion (n ~1), the creep rate could be estimated by following equations:

$$\sigma = \frac{3F}{2\pi t^2}\left[(1+\nu)\ln\left(\frac{r_2}{r_1}\right)+\frac{1-\nu}{2}\left(\frac{r_2^2-r_1^2}{r_3^2}\right)\right] \tag{4-4}$$

$$\dot{\varepsilon} = \frac{\dfrac{t\,(1-\nu)}{(1-\nu^2)r_1^2}\left[(1+\nu)\,ln\left(\frac{r_2}{r_1}\right)+\frac{1-\nu}{2}\left(\frac{r_2^2-r_1^2}{r_3^2}\right)\right]}{\left[\left(\frac{r_2}{r_1}\right)^2-1-ln\left(\frac{r_2}{r_1}\right)+\frac{1}{2}\left(\frac{1-\nu}{1+\nu}\right)\left(\frac{(r_2^2-r_1^2)r_2^2}{r_3^2r_1^2}\right)\right]}\,\dot{d} \tag{4-5}$$

where F is the applied force, t the thickness of the sample, v the Poisson's ratio, $\dot{d}$ is the displacement rate measured from the bottom of the specimen, and r_1, r_2 and r_3 are the loading ring, supporting ring and specimen radius, respectively.

The ring-on-ring tests were carried out for anode materials (Ni-8YSZ). The purpose of the tests was to investigate the bending creep behavior of the anode, which were further compared with 4-point bending creep and compressive creep tests. The tests along with the specimens are described in *Table* **4-7**.

Table 4-7: Ring-on-ring creep tests.

Ni-8YSZ	Condition	Temp. (°C)	Stress (MPa)			
			5	10	20	30
A	4% H_2/Ar	800	-	1	1	1
		900	-	1	1	1
B		800	-	1	1	-
		900	-	1	1	1
C		800	-	1	-	-
		900	-	1	1	1
D		800	1	1	1	-
		900	-	1	1	1

(2) Four-point bending test

In a four-point bending test, a bar-shaped specimen is placed on two supporting rods and the load is applied by the two loading rods, as illustrated in *Figure* **4-7**.

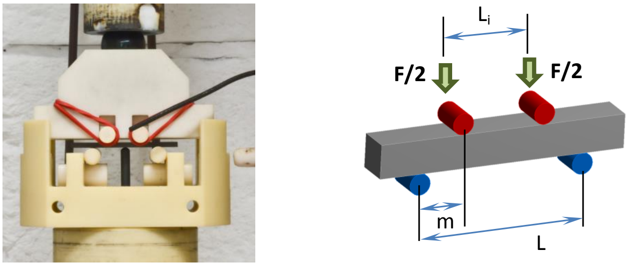

Figure 4-7: Four-point bending set-up and schematic illustration of a four-point bending test.

The bar-shaped specimens of reduced state anode material (Ni-8YSZ) were tested to determine the creep behavior. The equations used for analysis are discussed and shown in previous section 3.4.4. The list of anode specimens tested under 4-point bending and the corresponding testing conditions are given in *Table **4-8***.

Table 4-8: The anode specimens and testing conditions of four-point bending creep tests.

Ni-8YSZ	Condition	Temp. (°C)	Stress (MPa)	
			10	20
C	4% H_2/Ar	800	1	1
		900	1	1

4.3.3. Finite element simulation

The creep behavior of the anode materials was simulated to compare the behavior with analytical and experimental results. The comparison of the analytical formulations and experiments was based on creep rates obtained from ring-on-ring and four-point bending tests.

All numerical simulations were performed using the software ANSYS 14.5. 2D analysis of the creep test was used in order to reduce computation time. An example of the meshed model for ring-on-ring simulations is given in *Figure **4-8***, while the meshed model of 4-point bending was very similar but in other symmetrical arrangement. In the case of ring-on-ring testing the boundary condition was that the axis of symmetry was constrained against movement in x-direction and a selected node against y-direction. In the case of 4-point bending, the boundary condition was similar. Loads were directly applied on selected nodes. The simulation was based on the Norton creep relationship. The material data used for the simulation are summarized in *Table **4-9***. The simulations of bending creep consisted of 2D specimen models, which were loaded /constrained by a point load/constraint. Simulation models of four-point and ring-on-ring bending tests consisted of around 14000 finite elements each.

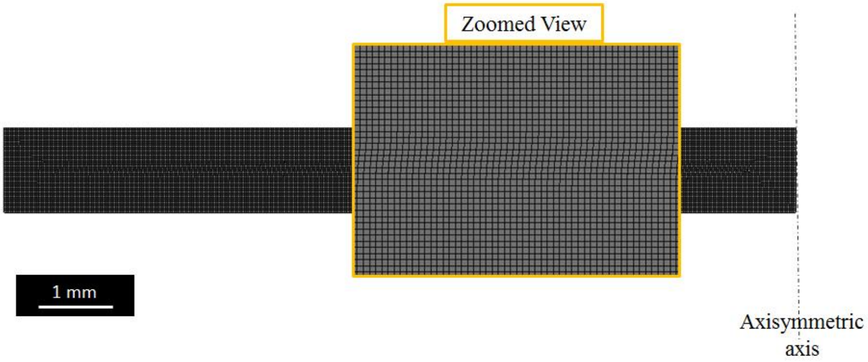

Figure 4-8: Meshed 2D model with 0.03 mm finite element size in the case of axisymmetric anode arrangement.

Table 4-9: Data from 4-point bending test in this work used in the FEM simulation of creep.

Temperature (°C)	*E* (GPa) [140]	Poisson's ratio [140]	*A* (s^{-1} MPa^{-n})	*n*	*Q* (kJ/mol)
800	29	0.29	5.7×10^{-4}	1.4	147

4.3.4. Bending strength

Bending tests were performed using an electromechanical testing machine (Instron 1362). The central displacement was measured with a sensor attached to the tensile loaded sample surface. A ceramic extension rod connected to a linear variable differential transformer (Sangamo, LVDT, range ± 1 mm, precision 1.25 µm) provided the value of actual displacement. The load was measured with a 1.5 KN load cell (Interface 110 BLR). The testing set-up permitted measurement was carried out from room temperature up to 1000°C. In this work two different bending techniques have been used, four-point bending test and three-point bending test, with head-to-head and bar-shaped specimens, respectively.

4.3.1.1 Four-point bending test

Besides creep behavior, four-point bending tests were also carried out to characterize fracture stress, following the ASTM C1-161 standard. The particularly designed head-to-head specimens used in this work are described in section 4.1.2. The elastic modulus and corresponding stress of 4-point bending can be expressed as:

$$E = \frac{3 \cdot \Delta F \cdot L^3}{16 \cdot b \cdot h^3 \cdot \Delta f} \tag{4-6}$$

$$\sigma = \frac{3 \cdot F \cdot m}{b \cdot h^2} \tag{4-7}$$

where ΔF and Δf are the force and deflection in the linear region of load-deflection curve, respectively. F is the applied force, L is the length between supporting rods, b and h is the specimen width and height, respectively. The elastic modulus is determined from the linear region of the load-deflection curve. The fracture stress is determined from the maximum applied load.

The four-point bending tested sealant specimens are listed in *Table* ***4-10***.

Table 4-10: Performed four-point tests on head-to-head and bar-shaped specimens along with the number of tested specimen.

Specimen	Material		Tests			Condition
			RT	700°C	800°C	
Head-to-head joined	H-Ag	As-sintered	15	1	1	Air
		500h/800°C	7	1	1	
	H-F	As-sintered	7	1	1	
		100h/850°C	5	1	3	
		1000h/850°C	5	1	1	
	7.5B(Ba)	As-sintered	20		6	
	10B(Sr)	As-sintered	10	6	2	

4.3.1.2 Three-point bending test

In a three-point bending test, a bar-shaped specimen is placed on two supporting rods and the load is applied by a rod placed in the center, as illustrated in *Figure **4-9***.

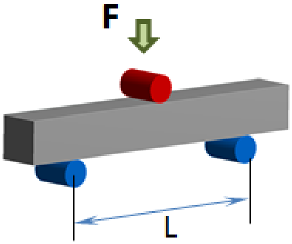

Figure 4-9: Schematic illustration of a three-point bending test

The experiments were carried out following the procedure recommended in ASTM C1-161. According to the linear elastic theory, the maximum stress, which appears in the central part on the tensile side of the specimen, can be determined from the relationship:

$$\sigma = \frac{3 \cdot F \cdot L}{2 \cdot b \cdot h^2} \tag{4-8}$$

where *F* is the applied force, *L* the length between the supporting rods, *b* the specimen width, and *h* the specimen height.

Three-point bending tests were used to characterize the fracture stress of 7.5 B(Ba) and 10B(Sr) and further compared with Jülich sealant materials. The tests were carried out at room temperature and elevated temperatures (650°C and 800°C), respectively. Note that 3-point bending tests were carried out to permit a direct comparison with tests carried out at CSIC, Madrid.

The list of specimens tested under 3-point bending and the corresponding testing conditions are given in *Table **4-11***.

Table 4-11: Performed three-point tests on bar-shaped specimens along with the test number.

Sealant	State	Test		
		RT	650°C	800°C
7.5 B(Ba)	24h/800°C	5	-	3
	800h/800°C	5		3
10 B(Sr)	24h/750°C	5	3	
	800h/750°C	5		3

4.3.5. Torsion strength (shear strength)

Sealants in SOFC stacks are exposed to a combination of tensile and shear load [120]. Since ceramic materials can have different properties in compression and tension [194] and to correlate tensile and shear properties, a torsion test appears to be the most useful method to observe the shear strength. An in-house torsion set-up has been developed at IEK-2, Forschungszentrum Jülich (*Figure **4-10***). The torsion tests were carried out for H-Ag and H-F sealants.

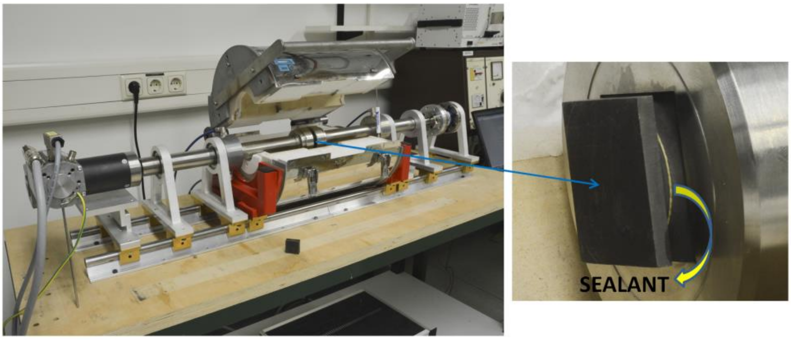

Figure 4-10: The torsion set-up along with the joined plate specimen.

In the torsion test, a joined plate-shape specimen was twisted by two loading arms until fracture occurred. The rotational speed was ~ 4°/min. The maximum torque that might be used in the set-up is 220 Nm. A horizontal folding oven with temperature range up to 1000°C was used for the high temperature tests. The shear stress could be calculated by following equation [189]:

$$\tau = \frac{16\,T}{\pi d^3} \tag{4-9}$$

where τ is the shear stress, T the applied torque, and d the diameter of the joining area, here 25 mm. The torques was calculated at specimen fracture.

A list of specimens tested in the torsion test and the corresponding testing conditions are given in *Table* ***4-12***.

Table 4-12: Performed torsion tests on joined plate specimens.

Sealant	Joining at 850°C (h)	Temperature (°C)	Tests	Condition
H-Ag	100	RT	1	Air
	10	RT	3	
		600	2	
		800	1	
H-F	100	RT	5	
		600	1	
		800	1	
	10	RT	3	
		800	1	

5. Results and discussion

5.1. Anode material

In this chapter anode materials have been investigated. Microstructural investigations show the internal structure, such as grain size, phases and pores. Fracture toughness and creep behavior results are summarized as studied via different testing methods.

5.1.1. Microstructure

5.1.1.1. Microstructure of double torsion specimens

Microstructural investigations were carried out on several types of materials mainly to analyze the porosity, which might influence the fracture toughness values. SEM images of all 8YSZ-composed material types are shown in *Figure* ***5-1***. Due to confidential issues, microstructural analysis was not carried out for the TOFC-supplied NiO-3YSZ material.

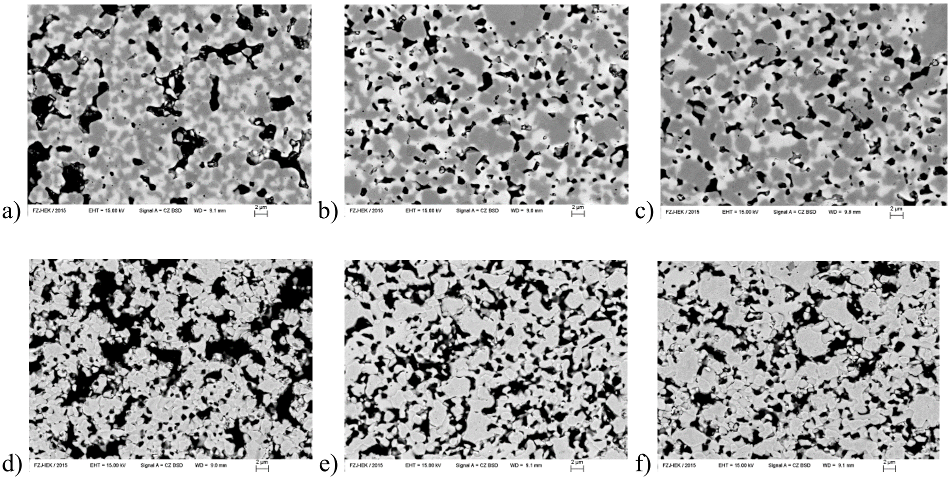

Figure 5-1: SEM images of 8YSZ-composed material types analyzed in this study; upper row corresponds to NiO-8YSZ, while lower row to Ni-8YSZ microstructures: (a) and (d) type 2, (b) and (e) type 3 and (c) and (f) type 4.

5.1.1.2. Microstructure of creep tested materials

The microstructures of anode materials A, B, C and D tested in this work are shown in *Figure* ***5-2***. By shortening the working distance of SEM lens to the specimen, the brightness and contrast were specially adjusted in few images to enhance grain orientation contrast, which permits the grain sizes' determination of the materials by visual inspection even in the case of blurry boundaries. It appeared that all of the materials possessed similar grain sizes according to these high contrast SEM images (*Figure* ***5-2*** (e)), with average value of around 1 to 2 µm. The similarity of the grain sizes ensures that there is no grain size effect that would bias the creep rates for the tested materials.

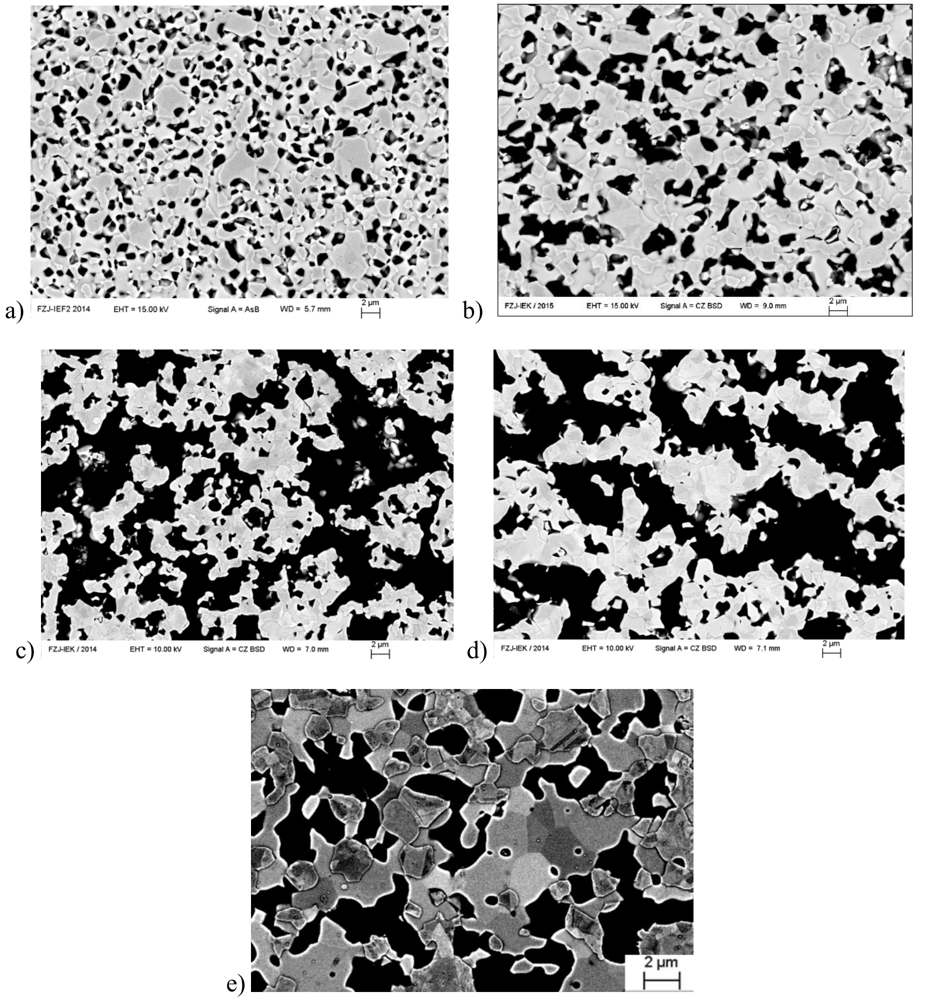

Figure 5-2: Microstructures of materials A, B, C and D in a) to d); as well as an example for the high contrast image for grain orientation in e).

5.1.2. Fracture toughness by double torsion test[1]

5.1.2.1. Necessity of a pre-crack

Double-torsion tests, like most fracture toughness tests [138], require a notched specimen in order to reduce elastic energy on crack initiation and hence to permit stable crack growth that is a prerequisite for fracture toughness evaluation. In addition, it has been observed that the evaluated fracture toughness data are biased by the crack tip radius, i.e. round crack tips lead to higher values and hence often a sharpening of the notch is carried out [138]. In the case of a double-torsion test, a pre-crack of the specimen is normally introduced before the test to obtain a sharp crack tip and high stress concentration [193]. However, the effect and necessity of the pre-cracking onto the evaluated data required an initial test series. Note, in addition to the potential effect on the fracture toughness via the crack tip radius, the pre-crack also leads to a further reduction of the necessary elastic energy for crack initiation and hence enhances the crack growth stability.

a) NiO-3YSZ

The specimens were tested initially with and without pre-crack to observe the effect and necessity of pre-crack. The resulting curves (*Figure* ***5-3***) show a significantly longer plateau region in case of specimens which were previously loaded with a slow displacement rate to obtain a pre-crack before the DT test. The specimens tested without previously inducing a pre-crack showed a shorter and a slightly instable plateau region (*Figure* ***5-3***). However, when taking individual thickness of specimen and average value of the plateau region into account, fracture toughness was identical within the limits of uncertainty. The average fracture toughness of specimens with and without the pre-crack was 3.05 ± 0.17 $\mathrm{MPa \cdot m^{1/2}}$ (*Table* ***5-1***), confirming that there is no necessity to pre-crack the current thin and brittle material.

The obtained fracture toughness values are slightly higher than the ones reported in literature for NiO-3YSZ (2.55 ± 0.2 $\mathrm{MPa \cdot m^{1/2}}$ [138]), which might be a result of slight porosity differences of the respective specimen batches. Furthermore, the values are significantly lower than reported for dense 3YSZ, which has a fracture toughness of 5.0 $\mathrm{MPa \cdot m^{1/2}}$ [195]. It might be assumed that the difference in fracture toughness is mainly caused by a difference in porosity of the specimens.

---

[1] Study has partly been published as J. Wei, G. Pećanac, et al., Proc. 12th Euro SOFC & SOE Forum, Luzern, B1309, 2016 and publiched as G. Pećanac, J. Wei, J. Malzbender, J Power Sources, 327 (2016) 629-637.

Furthermore, Delaforce et al [196] showed that NiO also effects the stability of the t-phase, leading to less transformation toughening of 3YSZ and hence a lower fracture toughness.

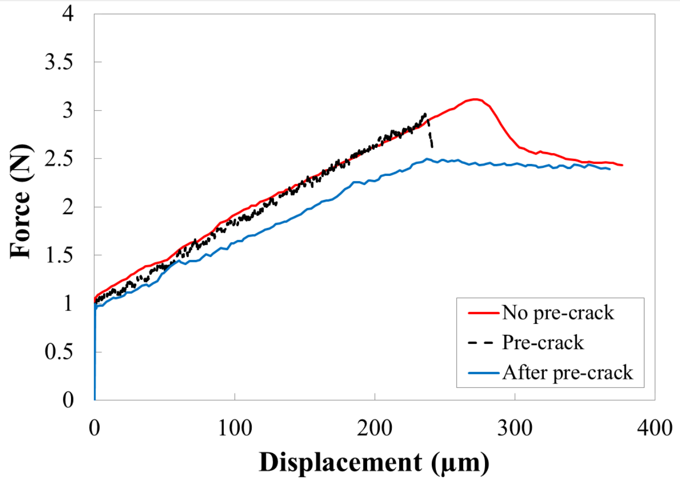

Figure 5-3: Typical curves of fracture tests with and without a pre-crack, indicating similar results and therefore confirming that pre-crack is not necessary for the material in the used geometry.

b) NiO-8YSZ

Similar initial tests were carried out on NiO-8YSZ (type 4) materials to analyze the necessity of pre-cracking. The NiO-8YSZ specimens are slightly thicker, hence, the elastic energy before crack initiation would be much larger and the instable crack growth might be possible in this case. The resulting curves confirmed this assumption (*Figure* ***5-4***), the specimen without pre-crack failed instable and did not permit a reliable fracture toughness characterization (red curve in *Figure* ***5-4*** shows a typical behavior without a pre-crack).

Compared to the non-pre-cracked specimen, the pre-cracked specimen yielded a stable crack growth region, which permitted a reliable determination of fracture toughness. The obtained average fracture toughness of 1.76 ± 0.15 MPa·m$^{1/2}$, considering the difference in material's production and porosity, is in agreement with the reported data from Radovic et al (1.6 ± 0.2 for 21.8 ± 1.3 % porosity [137]). According to literature, the fracture toughness of dense 8YSZ and NiO are 1.65 MPa·m$^{1/2}$ [197] and 1.5 MPa·m$^{1/2}$ [198] respectively, implying that the difference compared to those values might be a result of experimental uncertainties, or it might be speculated that NiO has even a positive influence on the fracture resistance of the composite. The latter might not be the case since Delaforce et al [196] found that in case of 8YSZ the phase composition remained unaltered after NiO was added.

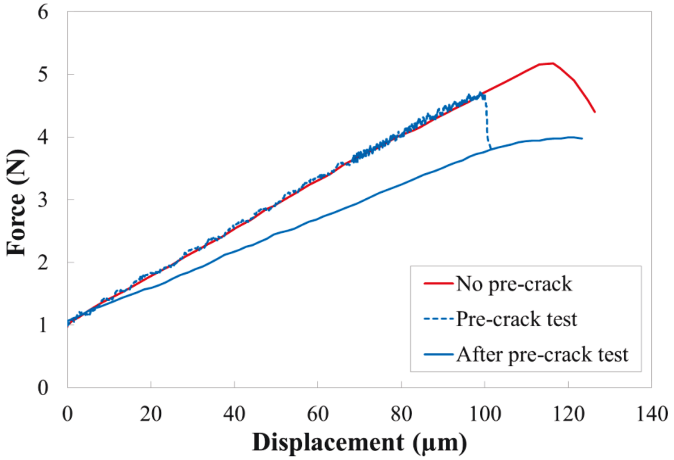

Figure 5-4: The type 4 Ni-8YSZ specimens were tested with and without pre-cracking. It showed that the fracture test without a pre-crack test leads instable crack growth and overestimation of the fracture toughness.

Table 5-1: Fracture toughness of NiO-3YSZ and NiO-8YSZ was measured under 1000 µm/min at room temperature in air.

Material	Fracture toughness (MPa·m$^{1/2}$)
NiO-3YSZ	3.05 ± 0.17
NiO-8YSZ	1.76 ± 0.15

5.1.2.2. Ni-YSZ (reduced material)

The necessity of pre-cracking was also verified for the reduced material. Tests on the load rate effect (see following section) revealed that the load rate of at least 2000 µm/min was necessary for Ni-8YSZ type 4 specimens, yielding an apparently higher fracture toughness (4.12 ± 0.12 MPa·m$^{1/2}$) compared to the oxidized state (*Table* **5-2**). (Note that 2000 µm/min was determined based on displacement rate effect described in next section as shown in *Figure **5-5***.) A similar value for reduced cells has been reported in [199]. The result indicates a positive effect of ductile metallic Ni particles on crack growth resistance, which was obviously stronger than the decrease of the fracture toughness due to the reduction-associated increase in porosity.

Ni-3YSZ specimens tested with a load rate of 1000 µm/min yielded with 3.85 ± 0.27 MPa·m$^{1/2}$ a very similar fracture toughness value as obtained for Ni-8YSZ. The fracture toughness is 26 % higher compared to the respective material in the oxidized state (3.05 ± 0.17 MPa·m$^{1/2}$), confirming that Ni particles enhance the fracture toughness. However the effect is stronger in the case of Ni-8YSZ where the increase in fracture toughness of reduced specimens compared to oxidized specimens accounts in the case of type 4 material to ~ 230%, indicating that in the case of Ni-3YSZ either the decrease of the fracture toughness due to porosity has a stronger effect or any increase due to Ni ductility is less pronounced which might be associated with differences in Ni-YSZ ratio or grain / pore size.

Table 5-2: Fracture toughness of NiO-8YSZ in type 4 and NiO-3YSZ along with their reduced state.

Material	K_{IC} at RT (MPa·m$^{1/2}$)
NiO-8YSZ	1.76 ± 0.15
Ni-8YSZ	4.12 ± 0.12
NiO-3YSZ	3.05 ± 0.17
Ni-8YSZ	3.85 ± 0.27

5.1.2.3. Sub-critical crack growth

Both NiO-3YSZ and NiO-8YSZ were characterized with respect to their sensitivity to subcritical crack growth (SCG) at RT via variation of displacement rates. To have a sufficient range, NiO-8YSZ was analyzed with loading rates of 10 µm/min, 100 µm/min and 1000 µm/min, while NiO-3YSZ was additionally also tested with 1 µm/min and 2000 µm/min. In both cases it was confirmed that the materials are sensitive to SCG and the fracture toughness evaluation is affected, as shown in *Figure **5-5***. Lower fracture toughness were obtained when testing the specimens with lower displacement rates, i.e. more time was available for chemical reaction to take place at the crack tip in the stressed microstructure. The results generally agree with previous findings by Selçuk and Atkinson [173] on YSZ material´s SCG sensitivity. This result also indicates 1000 µm/min is sufficient enough to measure fracture toughness of NiO-3YSZ and NiO-8YSZ reliably. Post-test SEM inspection of the specimens which were tested with 10 µm/min did not reveal any changes in microstructure related to the SCG.

Testing reduced Ni-8YSZ with different displacement rates resulted in a larger SCG effect. The material (Ni-8YSZ, type 4) was tested in a range from 100 µm/min to 5000 µm/min (*Figure* **5-5**). In all cases, the maximum load was used for fracture toughness determination. The obtained results imply that for NiO-3YSZ and NiO-8YSZ it is sufficient to perform the tests at 1000 µm/min in order to avoid SCG influence, while for Ni-8YSZ the test should be performed with at least 2000 µm/min.

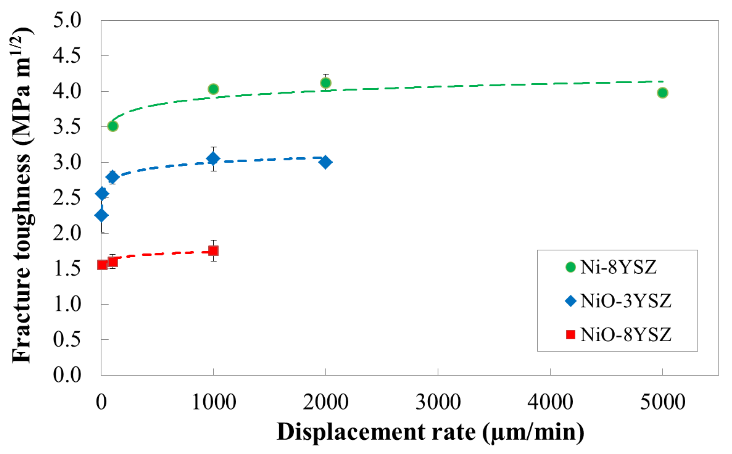

Figure 5-5: Ni-8YSZ appears to be strongly influenced by SCG effects. Fracture toughness as a function of displacement rate for Ni-8YSZ.

5.1.2.4. Elevated temperature tests

The start-up of a SOFC stack is often associated with the joining or sealing step before the reduction step. Hence, both NiO-3YSZ and NiO-8YSZ (type 4) were tested at a typical operation temperature of 800°C in air (*Table* **5-3**). While NiO-8YSZ showed similar values as at room temperature (1.93 ± 0.04 compared to 1.76 ± 0.15 MPa·m$^{1/2}$), the fracture toughness of NiO-

3YSZ was clearly lower than that obtained at room temperature (2.64 ± 0.06 compared to 3.05 ± 0.17 MPa·m$^{1/2}$) as shown in *Figure* ***5-6***. The rather stable fracture toughness could be associated with the cubic phase remaining stable at 800°C, resulting in relatively constant fracture toughness. NiO-3YSZ exhibits a transformation toughening due to t-m phase transformation. This effect becomes significantly weaker with increasing temperature [179], leading to a decrease of fracture toughness compared to values at room temperature. The additional fracture toughness tests for Ni-3YSZ at 300, 500 and 650 °C confirmed that the decrease occurred above 300 °C (see *Figure* ***5-6***), which agrees with the information of phase transformation diagram (YSZ ~ 50 wt%).

The temperature influence was also investigated in the case of reduced specimens. Ni-8YSZ revealed an almost 50 % decrease for a temperature of 800 °C compared to room temperature (2.75 ± 0.09 compared to 4.12 ± 0.12 MPa·m$^{1/2}$, see also *Table* ***5-3)***. Tests on Ni-3YSZ indicated a strong deformation at 800 °C due to low elastic modulus and perhaps ductile behavior. The curves showed a clear plateau region associated with crack growth permitting determination of facture toughness (~ 3.56 ± 0.14 MPa·m$^{1/2}$). The extremely large deformation impeded full fracture within the measuring range of set-up, which however, is not a pre-requisite for fracture toughness determination. It appears that the ductility of Ni which enhances fracture toughness of especially the 8YSZ composite strongly at room temperature via energy consumption does not lead to such a strong enhancement at elevated temperatures, i.e. the yield strength of the Ni is much lower at 800 °C. The 3YSZ composite, whose fracture toughness was increased by a lower amount at room temperature by the ductile Ni also shows a lower decrease of fracture toughness at elevated temperatures. Hence, Ni-3YSZ shows superior behavior with respect to fracture toughness compared to Ni-8YSZ at 800 °C.

Table 5-3: The fracture toughness of anode materials in oxidized state at room temperature and 800°C.

Material	K_{IC} at RT (MPa·m$^{1/2}$)	K_{IC} at 800°C (MPa·m$^{1/2}$)
NiO-3YSZ	3.05 ± 0.17	2.64 ± 0.06
NiO-8YSZ	1.76 ± 0.15	1.93 ± 0.04
Ni-3YSZ	3.85 ± 0.27	3.56 ± 0.14
Ni-8YSZ	4.12 ± 0.12	2.75 ± 0.09

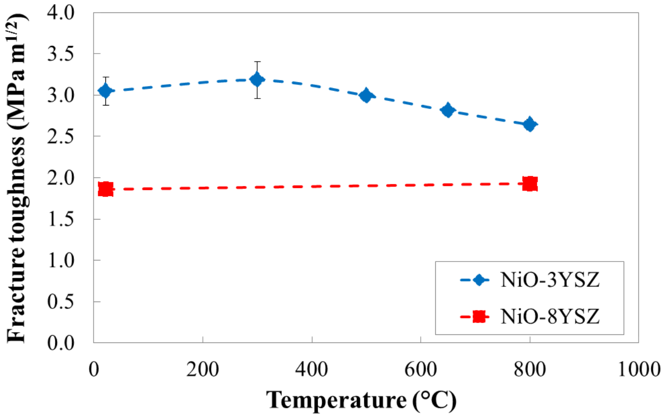

Figure 5-6: Facture toughness of Ni-3YSZ decreased at 800°C, while the values of NiO-8YSZ remained rather stable.

5.1.2.5. Influence of production route

With respect to industrial relevant material production it is critical to optimize the production routine. Although tape casting is nowadays the standard procedure for large scale cell production, a benchmarking against warm pressed material is still appropriate. The tests using pre-cracked specimens with the appropriate loading rate of 1000 µm/min revealed that tape cast type 4 material has the highest fracture toughness (1.76 ± 0.15 MPa·m$^{1/2}$), while type 3 (1.56 ± 0.10 MPa·m$^{1/2}$) and type 2 (1.23 ± 0.12 MPa·m$^{1/2}$) yielded lower values. Differences can be related to the different porosity of these materials (see *Table* **5-4),** i.e. type 4 has the lowest porosity (13 %), whereas type 2 material has the highest porosity (22 %).

Fracture toughness differences become even larger for the respective reduced Ni-8YSZ materials. Here the type 4 material displayed the highest fracture toughness (4.12 ± 0.12 MPa·m$^{1/2}$), while single complementary tests on type 3 (2.97 MPa·m$^{1/2}$) and type 2 (1.84 MPa·m$^{1/2}$) showed lower values. This decreased fracture toughness of reduced materials confirms the porosity influence, where type 4 contains lowest porosity (30 %), and type 3 and type 2 have the porosity of 32 % and 38 %, respectively.

Based on the obtained results, it seems from mechanical point of view that the sequential tape casting is the most advantageous production route compared to the classical tape casting and warm pressing, although it still remains a question if similar high values can be obtained for type 2 and 3 materials if porosities are adjusted to similar levels. The observed differences are in agreement with [22], where a fracture strength analysis of the currently tested different NiO-8YSZ material types verified rather similar values for tape cast materials and a lower strength for the warm pressed material.

Table 5-4: The obtained fracture toughness of three different types of NiO-8YSZ and Ni-8YSZ.

Material	Base production	Porosity (%)	Fracture toughness (MPa $m^{1/2}$)
NiO-8YSZ type 4	Sequential tape casting	13 ± 1	1.76 ± 0.15
NiO-8YSZ type 3	Standard tape casting	16 ± 1	1.56 ± 0.10
NiO-8YSZ type 2	Warm pressing	22 ± 1	1.23 ± 0.12
Ni-8YSZ type 4	Sequential tape casting	30 ± 1	4.12 ± 0.12
Ni-8YSZ type 3	Standard tape casting	32 ± 2	2.97
Ni-8YSZ type 2	Warm pressing	38 ± 1	1.84

5.1.2.6. Re-oxidation of Ni

Two Ni-8YSZ type 4 specimens were tested at 800 °C in air after slow heating (8 K/min), which resulted in re-oxidation of Ni to obtain an indication of reoxidation effects onto this material property. The fracture toughness of 3.05 ± 0.03 MPa·$m^{1/2}$ was higher than for the NiO-8YSZ. This result is surprising considering that reoxidation causes formation of porous NiO particles and the associated volume expansion typically leads to micro-cracks in the brittle microstructure [47]. Force-displacement curves for the tested reoxidized NiO-8YSZ are shown in *Figure **5-7***, along with the equivalent for oxidized NiO-8YSZ which serves for comparison.

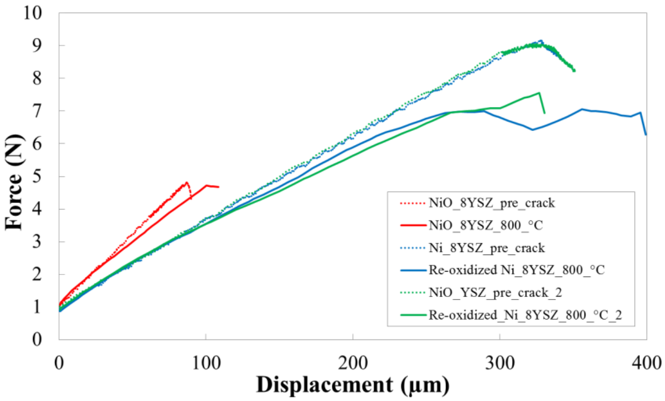

Figure 5-7: Force-displacement curves reveal for re-oxidized NiO-8YSZ higher fracture toughness values than for the oxidized material.

Insight into the reason for the high fracture toughness of re-oxidized Ni-8YSZ could be obtained by SEM/EDX analysis. The analysis revealed that the Ni was not fully re-oxidized, but metallic Ni cores remained within the NiO particles (*Figure* ***5-8***). Hence, Ni, which has high fracture toughness, contributed to the fracture toughness and resulted in a high fracture toughness of the re-oxidized Ni-8YSZ.

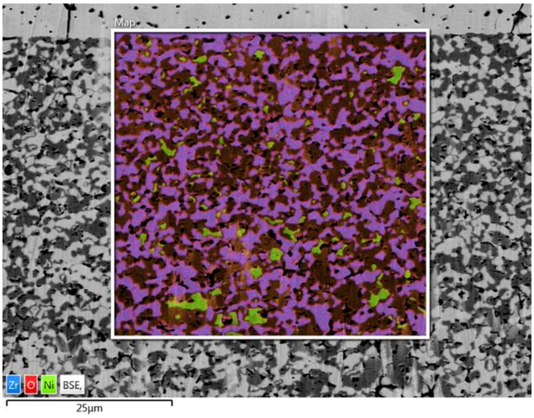

Figure 5-8: NiO particles found in the re-oxidized NiO-8YSZ verified the incomplete re-oxidization.

The microstructural analysis confirmed literature reports [47] of re-oxidation associated micro-cracking of the electrolyte layer. The channeling crack-type failure of the electrolyte can be seen in *Figure* ***5-9***.

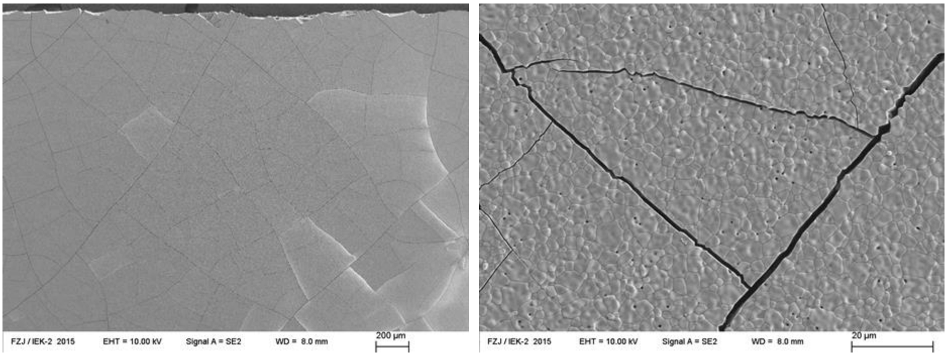

Figure 5-9: SEM images of the electrolyte surface showing a) numerous micro-cracks and b) transgranular failure mode.

5.1.2.7. Fracture surface analysis

Microstructural analyses were carried out in order to support fracture toughness analyses of anode substrate materials. Fracture surfaces of NiO-8YSZ (type 4) material were observed in the reduced state and re-oxidized state.

a) NiO-8YSZ tested at room temperature

With respect to the failure mode, the fracture surface of NiO-8YSZ specimens indicated a mixed failure mode (*Figure* ***5-10***). Similar findings on the failure mode of these material compositions have been reported in [143].

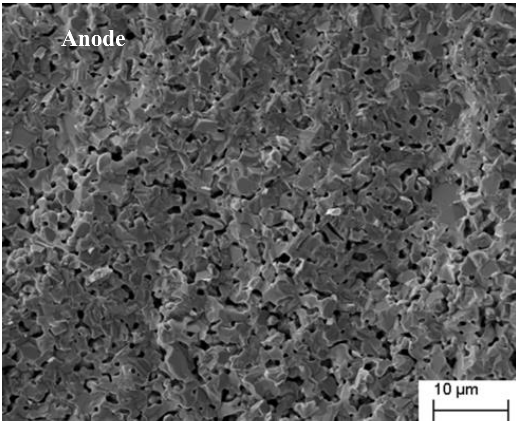

Figure 5-10: SEM images indicate a mixed mode failure of the NiO phase for a type 4 specimen.

b) NiO-8YSZ tested at 800°C

After the 800 °C tests, SEM investigations revealed a higher amount of intergranular failure for NiO-8YSZ, however, it was not possible to be quantified (*Figure* ***5-11***). This higher amount of intergranular failure at 800°C indicates that grain boundary fracture energy becomes lower compared to the fracture energy of the grains at elevated temperature. Nevertheless it can be concluded that, due to the small differences in values obtained at RT and elevated temperatures, the failure mode itself, i.e. trans- or intergranular does not permit any conclusion on the fracture toughness behavior.

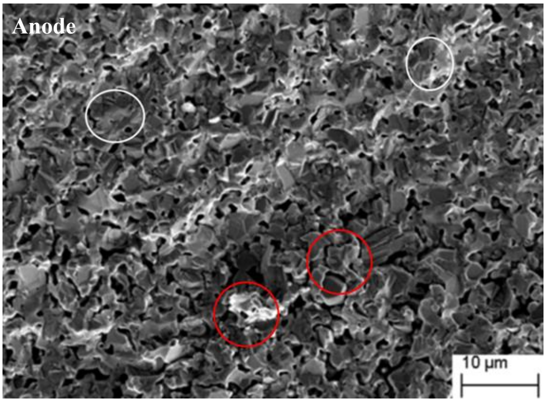

Figure 5-11: SEM image revealed a mixed failure modes of NiO-8YSZ at 800°C (type 4). The areas with white circles show transgranular failure mode examples, while intergranular mode examples are marked with red circles.

c) Ni-8YSZ tested at room temperature

In case of Ni-8YSZ, Ni particles showed pure intergranular failure (*Figure* ***5-12*** *(a)*) and a ductile deformation (*Figure* ***5-12*** *(b)),* indicating a fracture toughness increase due to energy consumption during crack growth. Crack bridging of Ni particles, which has been reported in [137], could not be found in the current study.

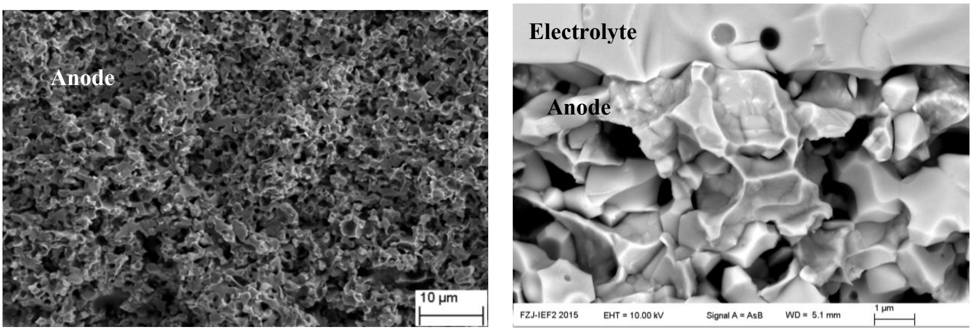

Figure 5-12: (a) Intergranular failure mode of Ni-8YSZ and (b) ductile deformation of Ni particles.

d) Re-oxidized NiO-8YSZ tested at 800°C

The channelling crack-type failure of the electrolyte through thickness can be seen in *Figure* ***5-13***. Further crack propagation into the substrate was not found. With respect to the failure mode, the re-oxidized NiO showed an intergranular failure mode (*Figure* ***5-13***).

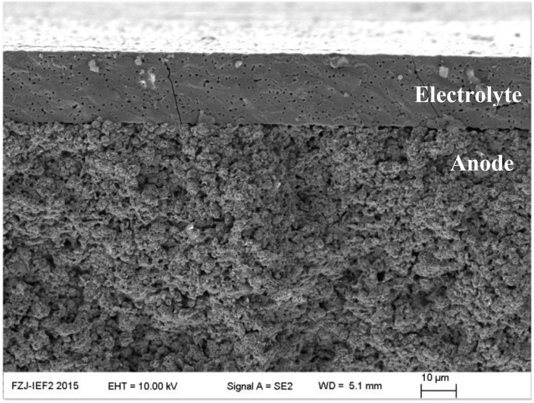

Figure 5-13: As in case of oxidized NiO, the re-oxidized NiO also showed an intergranular failure mode. The SEM image also confirms that the channelling-type cracks in the electrolyte do not propagate into the re-oxidized NiO-8YSZ composite.

5.1.2.8. Summary – fracture toughness

The section reported and discussed the fracture toughness results of the two most common anode substrate material variants, NiO-3YSZ and NiO-8YSZ, at room temperature and at a typical stack operation temperature of 800°C. Different types of warm pressed and tape cast NiO-8YSZ substrates were characterized in oxidized and reduced states. The study considered both, oxidized and reduced material states, where also an outlook is given onto the behavior of the re-oxidized state that might be induced by malfunctions of sealants or other functional components. Overall, the results confirmed superior fracture toughness of 3YSZ based composites compared to 8YSZ based composites in the oxidized state, whereas in the reduced 3YSZ based composites showed similar fracture toughness at room temperature, but a higher value at 800°C compared to 8YSZ based composites. Complementary microstructural analysis aided the interpretation of mechanical characterization.

5.1.3. Creep behavior

5.1.3.1. Compressive creep

The most straightforward way to assess creep behavior of ceramics is a compressive test. However, this requires special specimens that were produced as sintered bars in a rather dense state (20% porosity), i.e. it was not possible to add the pore formers typical for porous SOFC cells to the warm pressed materials and hence the porosity was only a result of the reduction associated shrinkage of the NiO particles.

The analysis of the steady-state creep rates was based on a linear fit of the data, reaching the regime of an inelastic flow characterized by a nearly constant slope in the experimental curve. To avoid the primary creep regime, the testing time was typically adjusted to between 20 and 25 h. Examples of typical deformation – time curves are shown in *Figure **5-14** (a)*.

The results for this type “A” bar-shape specimens are presented in a Norton’s plot in *Figure **5-14** (b)*. The stress exponent was determined from the slope of the $\ln(\dot{\varepsilon})$ versus ln (σ) representation at a constant temperature *T*. An average stress exponent of 1.2 ± 0.3 was derived (see also *Table **5**-**5***), indicating a diffusional dominated creep mechanism. Laurencin et al. [140] reported similar values of stress exponent, i.e. 1.1 for 750 °C and 1.7 for 800 °C, also indicating a diffusion creep mechanism for Ni-8YSZ anode materials.

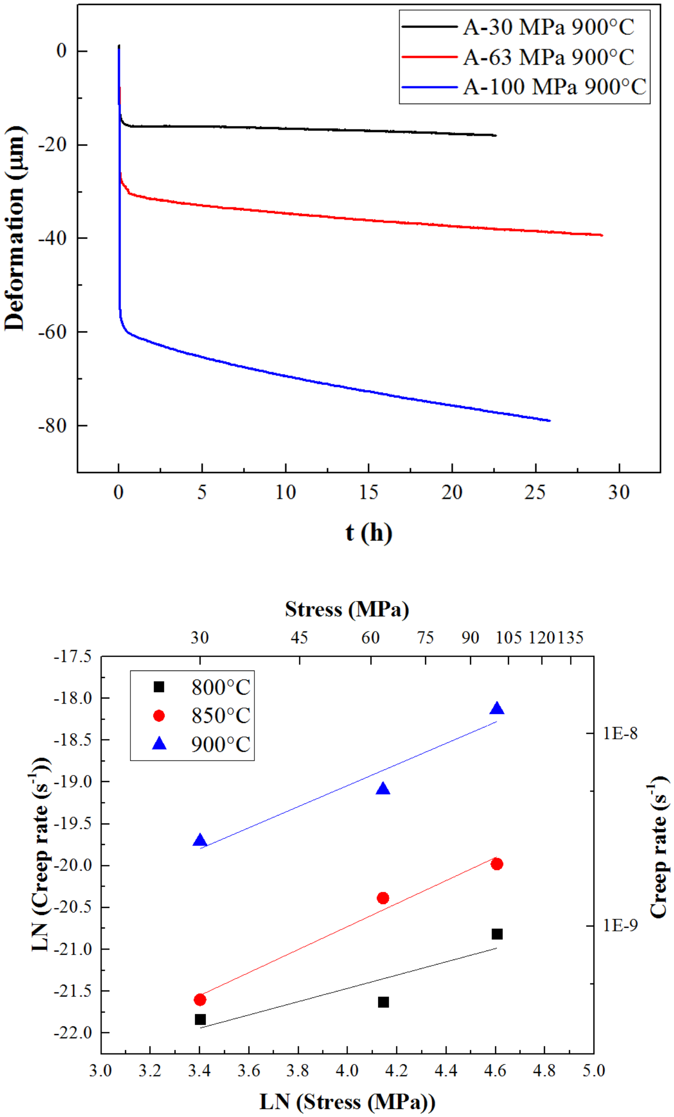

a)

b)

Figure 5-14: a) Typical deformation – time curves; b) compressive creep rates as a function of applied stresses.

The activation energy *Q* was calculated from a ln ($\dot{\varepsilon}$) versus 1000/*T* plot at a constant stress (*Figure* **5-15**). The derived activation energies for a temperature range of 800°C to 900ºC were 220 kJ/mol, 265 kJ/mol and 279 kJ/mol for stresses of 30, 63 and 100 MPa, respectively, yielding an average value of 255 ± 31 kJ/mol. The derived creep parameters are summarized in *Table* **5-5**.

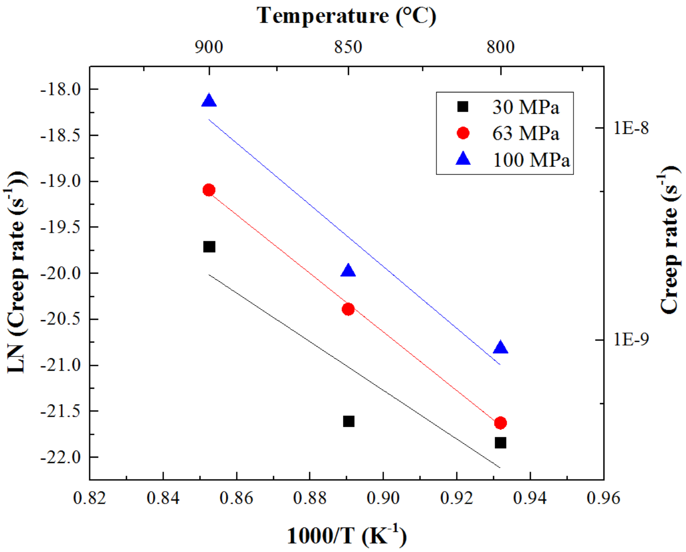

Figure 5-15: Creep rates as a function of temperatures

Table 5-5: Creep parameters of the Norton's law determined via compression test.

Temperature (°C)	Pre-factor *A* (s^{-1}MPa^{-n})	Stress exponent, *n*	*Q* (KJ/mol)
800	50	0.8	-
850	2.8	1.4	-
900	7.5	1.3	
800 - 900°C	-	-	255 ± 31

5.1.3.2. Ring-on-ring creep test

In order to assess if the creep is the same under compression and tension, ring-on-ring bending tests were carried out. In addition porosity and composition was varied to assess both effects for plate-shaped specimens of material A, B, C and D.

Material A yielded creep rates of $3.4 \cdot 10^{-10}$ s^{-1} and $1.6 \cdot 10^{-9}$ s^{-1} at 800°C and 900°C, respectively for an applied stress of 30 MPa , which are very similar to the values obtained from the compressive tests ($3.3 \cdot 10^{-10}$ and $2.8 \cdot 10^{-9}$ s^{-1}). This indicates a similar creep behavior of rather dense Ni-8YSZ anode material (~ 20 % porosity) under tension and compression for such a low, nevertheless application relevant, applied stress. Note that a higher applied stress might cause faster creep under tension due to well-known micro-crack formation for ceramics under tensile loads at elevated temperature (creep rupture effects) [200]. It has been suggested that materials with higher porosity, tensile creep rates should be higher than compressive creep rates due to densification [182, 201].

The activation energy of material A was also obtained from a creep rate-temperature plot as shown in *Figure* ***5-16***. The derived activation energies for a temperature range of 800 °C to 900 ºC were 221 kJ/mol, 135 kJ/mol and 161 kJ/mol for applied stresses of 10, 20 and 30 MPa, respectively, yielding an average value of 172 ± 44 kJ/mol.

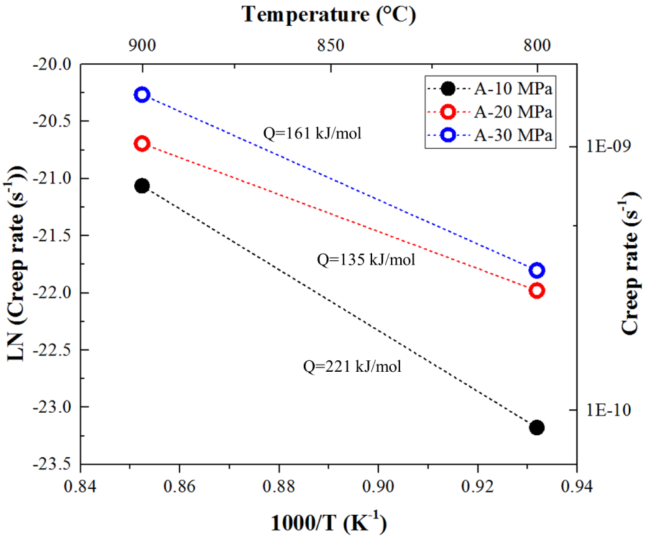

Figure 5-16: Creep rates as a function of temperatures of material A by ring-on-ring bending test.

The activation energies of materials B, C and D were also determined (*Figure* ***5-17***), which are 156 kJ/mol, 177 kJ/mol and 81 kJ/mol for the temperatures 800 °C and 900 °C (stresses either 10 or 20 MPa), respectively.

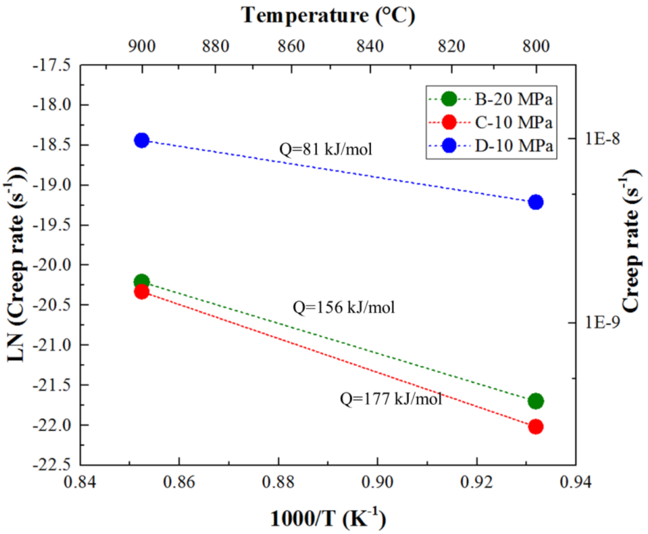

Figure 5-17: Creep rates as a function of temperatures of material B, C and D, ring-on-ring bending tests.

5.1.3.3. Four-point bending creep test

The equations used for ring-on-ring test assume a purely diffusional mechanism (n = 1), which might not to be the case according to the parameters derived from compression tests, i.e. although the standard deviation has to be considered, it appeared that n might be slightly above unity. Hence, due to the limitation of equation ***(4-5)*** of ring-on-ring creep, i.e. n = 1, complementary tests on material C were carried out using four-point bending and compared to ring-on-ring bending test results. Note, the four-point bending that were analyzed using a more complex set of equations that is not based on the assumption that n = 1.

Since the equation of 4-point bending creep includes stress exponent and deformation rate as input data, the stress exponent needs to be determined first. By deriving the equations of 4-point bending and creep, the deformation rate in the center of specimen has a straightforward relationship with half applied load as:

$$\ln\frac{\partial y}{\partial t} = n \cdot \ln\frac{F}{2} + \ln H \tag{5-1}$$

where *n* is stress exponent, *F* is applied load and *H* is a function of specimen geometry. The detailed derivation of equation can be found in the ***Appendix***.

By plotting the deformation rate as a function of the applied loading force and temperature, the stress exponent and activation energy can be obtained, see *Figure* ***5-18***. The values of ln(*H*) were determined from the intersection on Y-axis of *Figure* ***5-18*** *(a)*, which were used to determine A values (see ***Appendix***). The obtained creep parameters from the 4-point bending are shown in *Table* ***5-6***.

4-point bending creep yielded an average stress exponent 1.4 ± 0.1, which is similar to the value obtained from ring-on-ring bending creep. This indicates diffusion-dominated creep. The average activation energy of 147 ± 1 kJ/mol for the temperature range of 800°C and 900°C is similar to the value of 177 kJ/mol obtained from ring-on-ring creep for a stress of 10 MPa

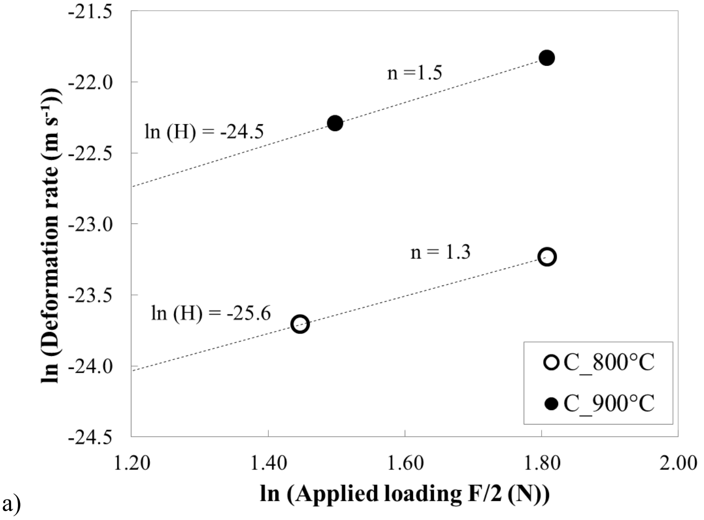

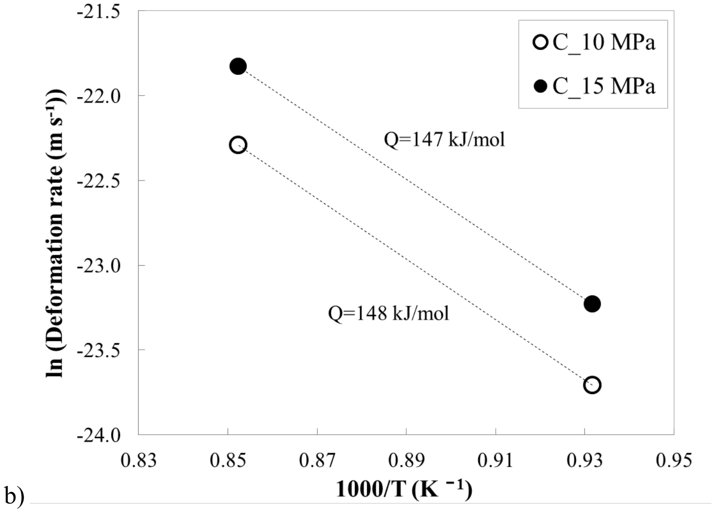

Figure 5-18: Stationary deformation rates are plotted as a function of (a) applied loading force; (b) inverse temperatures.

Table 5-6: The creep parameters of material C obtained from 4-point bending test.

Temperature (°C)	*A* (s^{-1} MPa^{-n})	Stress exponent, *n*	Activation energy *Q,* (KJ/mol)
800	5.7×10^{-4}	1.3	-
900	3.3×10^{-4}	1.5	-
800 - 900	-		147 ± 1

5.1.3.4. Discussion

5.1.3.4.1. Activation energies

The activation energies obtained from the different tests for the temperature range of 800 °C to 900 °C are summarized in Table ***5-7***, whereas Table ***5-8*** gives reference values from literature.

Table 5-7: Average activation energies of material A-D were measured by different tests in this work.

Ni-8YSZ	*Q,* (kJ/mol)		
	Compression	Ring-on-ring bending	4-point bending
A	255 ± 31 (30-100 MPa)	221 (10 MPa)	-
		135 (20 MPa)	
		161 (30 MPa)	
B	-	156 (20 MPa)	-
C	-	177 (10 MPa)	148 (10 MPa)
			147 (15 MPa)
D	-	81 (10 MPa)	-

Table 5-8: Activation energies for diffusion and creep in literatures.

Material	Grain boundary diffusion, Q_{gb} (kJ/mol)	Plasma-sprayed coating creep, Q_{plasma} (kJ/mol)	4-point bending creep, $Q_{4\text{-}p}$ (kJ/mol)
Ni	115[148]	-	-
8YSZ	309[202]	-	-
Porous 8YSZ	-	190[203]	-
Ni-8YSZ	-	-	115[140]

(1) Influence of loading configuration on activation energy

It is clear from the compressive tests on material A that the activation energy does not depend on the applied compressive stresses. Controversy, the ring-on-ring bending tests revealed a clear decrease of the activation energy with increasing applied stress, even though the stress range was much lower (10-30 MPa) than the one in compression (30-100 MPa). Hence, there is an indication of a stress dependency under tensile stresses for the material.

For material A, the activation energy (255 ± 31 kJ/mol) obtained from compressive test is in very good agreement with the value from ring-on-ring bending test under a low stress of 10 MPa (221 ± 44 kJ/mol), verifying the similar creep behavior of compressive and tensile creep rates at rather lower stress.

On the other side, the activation energy (~147 kJ/mol) of material C obtained from four-point bending is close to the value (177 kJ/mol) from ring-on-ring bending test (uncertainty ~ 15 and 20% as discussed above). This verifies that both four-point and ring-on-ring bending tests are suitable for a determination of the activation energy.

(2) Temperature dependency

Changes of activation energy with temperature have been reported in other studies [204]. It appears from Fig. 2c that there might be a change in activation energy at around 850 °C, which would indicate below 850 °C a lower activation energy, which would be in agreement with the value from bending tests quoted in [140]. However, due to the limited experimental database and associated high uncertainty in derived parameters, it was not attempted in the current work to separate the creep rates into different temperature ranges and corresponding activation energies.

(3) Comparison of activation energy with diffusion

In a previous study it was suggested that the creep of Ni-8YSZ cermet is mainly controlled by the behavior of 8YSZ [44, 140]. For material A, the average activation energies of compressive tests as well as the ring-on-ring test at low stress (10 MPa) are similar to the activation energy of bulk 8YSZ for grain boundary diffusion (Q_{gb} = 309 kJ/mol), although the values are still slightly lower. Actually, most of values obtained from bending tests are much lower than $Q_{gb.}$ Withney et al. [205] have proposed an explanation to this low activation energy based on the creep behavior of 8YSZ plasma-sprayed coatings. At T < 1100°C, the creep mechanism in YSZ appears to be dominated by a Zr^{4+} surface diffusion (Q_{plasma} = 190 kJ/mol), which shows a good agreement to the values in current work. It seems that the creep mechanism for bending tests is more dominated by this surface diffusion for higher creep deformation (at deflections exceeding 15% of thickness), while the compressive test is more dominated by the bulk diffusion (creep deformation is ~ 1% of height). This indicates the potential different creep response under the compression and tension.

(4) Porosity effect

In the current work, the Q values of material A-D were determined, in order to investigate the effects of porosity and composition. Considering only average values, in the case of the similar material’s composition, Materials B and C yielded similar activation energies as material A, indicating that the porosity doesn’t have a strong effect onto the activation energy of the considered materials. However, material D yielded a much lower value (81 kJ/mol) along with significantly higher creep rates, indicating a strong influence of the material´s composition or surface diffusion effects on the activation energy.

5.1.3.4.2. Effects of porosity on creep rates

Previous studies verified that porosity influences the properties of ceramics, not only fracture strength and elastic modulus, but also creep behavior [206]. Kawai et al. [44] suggested that the creep is dominated by the elevated temperature deformation of YSZ and the Ni phase can be considered in a good approximation as pore in porous Ni-YSZ composites. Hence, it is leading an apparent "equivalent porosity", which is basically the sum of volume percentage of pores and Ni phase in the cermet. In fact, in the current work, a series of experiments were carried out to investigate the porosity influence. Material A, B, C and D were tested in a ring-on-ring setup.

The creep rates as a function of equivalent porosity are shown in *Figure* ***5-19***, where an apparent equivalent porosity was also calculated for material D. In agreement with previous studies the current work verifies that the Ni in the cermet material doesn't contribute much to the material's creep resistance. It can be clearly seen that the creep rates increase with increasing porosity. At 800 °C under 10 MPa, material B yields an around 2 times higher creep rate compared to material A, while material C shows an around 3 times higher creep rate. At 900 °C, material C shows around 2 times higher creep rate than material A. Similarly, for each stress and temperature, the higher porosity led to around 1.5 to 3 times higher creep rate compared to the rather dense material A, confirming that the porosity can significantly decrease creep resistance. Material D contains the smallest amount of YSZ, which leads even 7 or 17 times higher creep rates compared to material C.

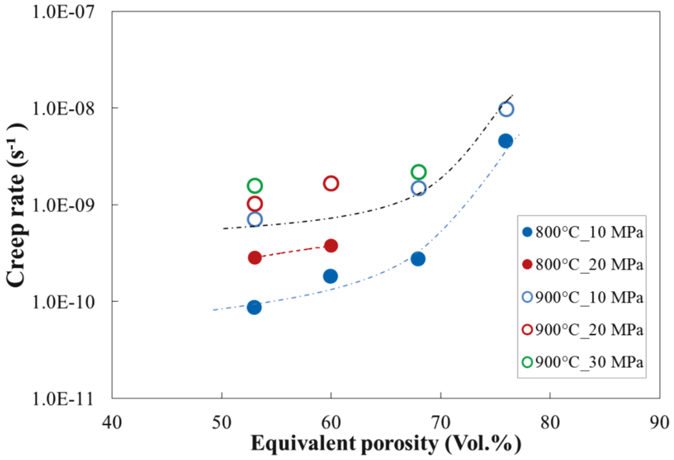

Figure 5-19: Creep rates as a function of equivalent porosities.

Several models are available to predict the creep rates for porous materials, such as Gibson-Ashby [161], Hashin-Shtrikman [109], Ramakrishnan [112] and Mueller [162] models, using equations (3-14) (3-17) (3-18) and (3-15), respectively. To analyze the porosity effect numerically, the creep rates obtained experimentally are compared with the analytical models in *Figure* ***5-20***. The analytical models were used to model the creep rates at 800 ºC under 10 MPa, in fact, the tendency of the models was similar for the other data sets. Among the analytical models, the Hashin-Shtrikman yielded the good approximation in range of 50-70% equivalent porosity, while the Ramakrishnan model provides the closet prediction when the equivalent porosity is above 70% in agreement with [44].

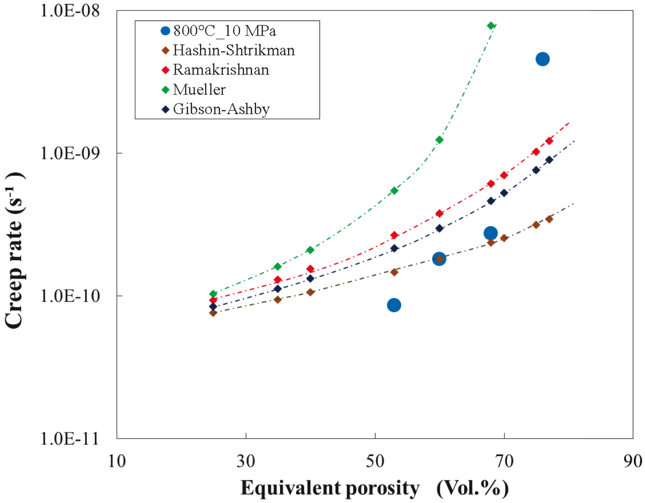

Figure 5-20: Comparison of the creep rates obtained from analytical models and ring-on-ring bending tests at 800°C.

5.1.3.4.3. Comparison of 4-point and ring-on-ring bending creep for material C

Once the stress exponent is determined (see section 5.1.3.3), the creep rate of 4-point bending test can also be determined by equation (3-12). A comparison of creep rates of 4-point and ring-on-ring creep along with reference data is shown in *Figure* ***5-21***.

The literature results [140] are slightly higher than the values obtained in this work, the reason might be assigned to material difference and/or experimental uncertainty. Creep rates of material C obtained from ring-on-ring tests are around 3 times lower than the values obtained from 4-point bending tests. This effect might be assigned to 1) stress distribution changes in 4-point bending and ring-on-ring bending tests and also 2) the limitation of analytical equation used for ring-on-ring creep. As mentioned above, the equations used for ring-on-ring creep calculation assumes a stress exponent of 1, which is not the case for the material in the current study. Since this could be the origin of the differences between 4-point bending and ring-on-ring creep, the accuracy of ring-on-ring creep determination is discussed in the following subsection.

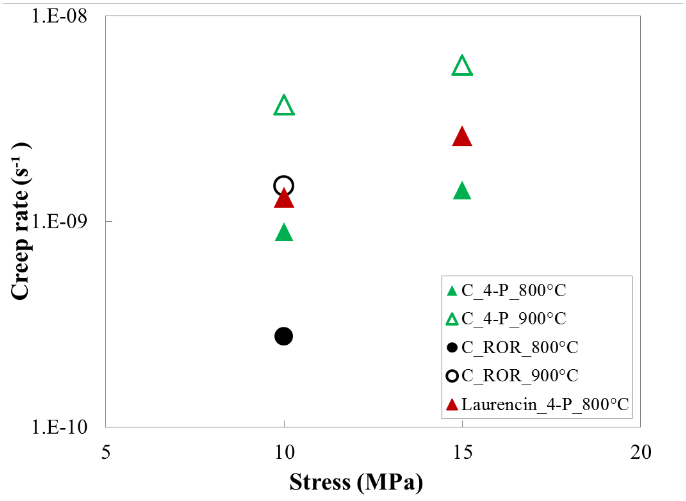

Figure 5-21: Comparison of creep rates obtained via 4-point and ring-on-ring tests along with reference data [140].

5.1.3.5. FEM simulation

A FEM analysis was carried out to analyze the origin of different creep behavior in ring-on-ring and 4-point bending tests, creep parameters derived from 4-point bending test in this work were used as input for the simulation (*Table **4-9*** in section 4.3.3). In the FEM simulation the creep rates were derived in two ways, i) from the equivalent creep strain by ANSYS and ii) from the deflection using the simulated displacement with the analytical formulas (Equation (3-12) and (4-5)). The creep rates obtained by these two methods are termed "FEM Result" and "FEM Equation", respectively, in the following. The creep strain at the bottom surface of the specimen, which is rather constant within the area enclosed by the loading ring, was taken as the FEM numerical result. An example of the simulated creep strain under 30 MPa at 800ºC by 4-point bending test is shown in *Figure* ***5-22***.

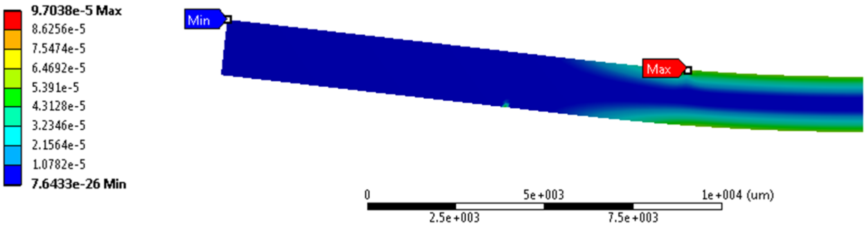

Figure 5-22: The equivalent creep strain simulated by ANSYS for a 4-point bending test under 30 MPa at 800 ºC.

The comparison of simulations and experimental data is shown in *Figure* ***5-23***. Both simulation results for 4-point bending creep (FEM Result and FEM Equation) show an agreement with experimental results at rather low stresses (10 and 15 MPa). The experimental value is slightly lower (the difference is smaller than 9%) than the simulation values which might be caused by friction during the real testing. The friction is not taken into account in case of simulation, while it seems that friction has an effect on creep rate. However, the FEM Result and FEM Equation also agree with each other (the difference is smaller than 4%), indicating the rather accurate analysis for creep in 4-point bending tests.

The FEM Equation and experimental data of ring-on-ring bending creep, both based on formulation, show general agreement. Similarly the friction effect might play an important role for this difference, which could have a stronger effect on ring-on-ring test due to the larger contacted area. While the FEM Results yielded around 50% and 72% higher creep rate compared to values of FEM Equation and experimental result, respectively, indicating the limitation of an analytical formulation to analyze data from ring-on-ring tests (Equation (4-5)). The formula analysis neglected changes of geometry, stress distribution due to the creep deformation and assume the unit stress exponent. It seems that the neglected changes of stress distribution and geometry play an important role in an accurate determination of ring-on-ring test creep rates.

To assess the inaccuracy caused by stress exponent in ring-on-ring equation (4-5), a few simulations based on various n values with same creep parameters (*Table* ***4-9***) at 800 °C for 10, 20 and 30 MPa were carried out (*Figure* ***5-24***). With increasing n, the difference of analytical to equivalent strain based result increases and then slightly decreases above $n \sim 2$. Since the equation neglects the change of stress distribution and geometry, a difference exists between the FEM Result and the FEM Equation, even when n is equal to one. Hence, the analytical formulation might be used as an approximation only in case that stress exponent is close to 1, otherwise FEM analysis has to be carried out to analyze ring-on-ring test data. However, for a very thin specimen, ring-on-ring test always needs higher load compared to 4-point bending test to reach the same applied stress, which makes bending creep characterization possible even for very thin specimens that fracture in uniaxial bending under experimentally necessary preloads. Hence in some special cases, such as extremely small applied load or excessive deformation in 4-point bending test, the ring-on-ring test is still a reliable testing method to estimate the creep behavior.

During the bending simulation, it was found that the stress distribution changes with time (being associated with an increase in deformation). The stress at the axial bottom of the specimen decreases slightly. The maximum stress at loading and supporting points increases largely, which might cause the crack in ceramics. This change of the stress distribution is a result of creep relaxation and illustrates well that such an effect should be taken into account for SOFC/SOEC stack operation.

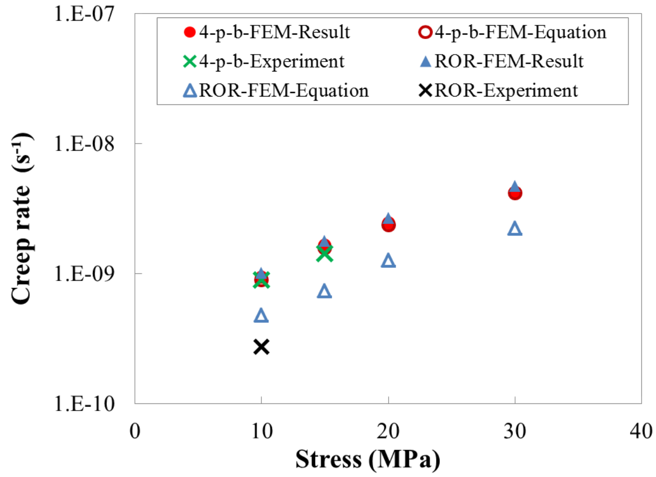

Figure 5-23: Creep rates obtained from FEM simulations

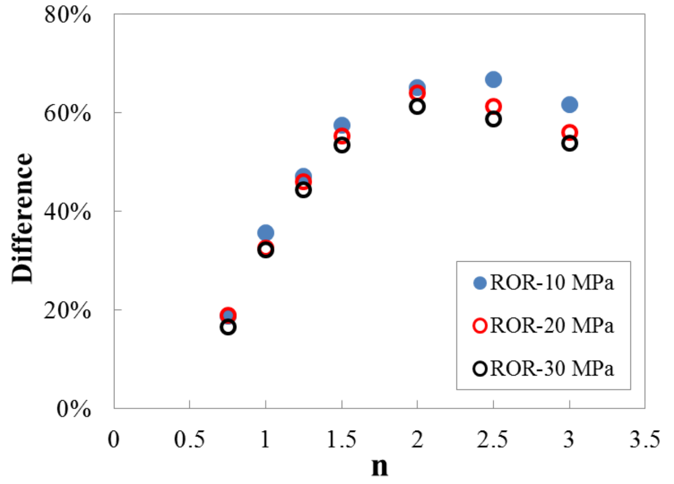

Figure 5-24: Difference in FEM results based on equivalent strain and analytical results as a function of stress exponent for different applied stresses.

5.1.3.6. Summary – anode creep and FEM simulation

Although the creep tests of Ni-8YSZ were rather difficult due to the small deformations and specimen geometry, the creep behavior of Ni-8YSZ anode materials was investigated systematically by different testing methods in this work. A diffusion-dominated creep mechanism of Ni-8YSZ was found for both compressive and tensile creep. The activation energies show a dependence on the material composition. The porosity has a negligible influence on activation energy of Ni-8YSZ anodes, while porosity can reduce creep resistance significantly and yield larger creep rates. YSZ is confirmed to carry most of the load during creep. The creep behavior obtained in this work can be used as important input data for microstructure simulation and modeling for the stack application.

FEM simulation was carried out to analyze the limitations of equations used in this work, especially for ring-on-ring creep tests. The discrepancy of the equation for ring-on-ring creep becomes larger with increasing stress exponent deviating from the value of unity. The change of the stress distribution with time should be taken into account for long-term application under stress exposure for SOFC stack operation.

5.2. Sealant materials

This section presents and discusses the experimental results obtained for the H-Ag, H-F, 7.5B(Ba) and 10B(Sr) sealants using bending and torsional testing. First, initial and annealed microstructures of the materials are compared. Then, bending strengths and the respective temperature dependency are discussed and compared with previous studies. Thereafter, crystallization effects and creep behavior of as-sintered and annealed sealant are compared. Finally, the shear strengths are discussed and compared with bending strengths.

5.2.1. Microstructure and XRD analysis

The microstructures of as-sintered and annealed sealant materials investigated using scanning electron microscopy and EDX will be presented in the following section. XRD analysis was carried out to characterize the crystallized phases in the H-Ag sealant.

(1) H-Ag

A representative SEM image in *Figure* ***5-25*** *(a)* shows white Ag particles, large black pores and light grey glassy phases in the as-sintered H-Ag sealant. The vertical interface with the steel plate can be seen on the right side of the image, where the microstructure appears to consist of smaller particles and crystallites. An elemental mapping (in *Figure* ***5-26*** *(a)*) verifies that there is no excessive reaction layer at the interface between sealant and steel. After 500 h annealing (*Figure* ***5-25*** (*b)*) the silver particles deformed and appeared to shrink. A respective elemental mapping in *Figure 5-26* (*b)* indicates that there is no significant change in the elemental distribution. The amount of dark grey crystallized phases (79 %) in annealed sealant increased significantly compared to the as-sintered state (46 %) (see also [65]). An additional complementary EDX focusing onto the interface of sealant and steel revealed a very thin oxidized steel layer (*Figure* ***5-26*** (*c)*). Also the XRD analysis of the annealed state (*Figure* ***5-27*** (*b)*) confirmed that the crystalline phase significantly increased after annealing, compared to as-sintered H-Ag (*Figure* ***5-27*** *(a)*).

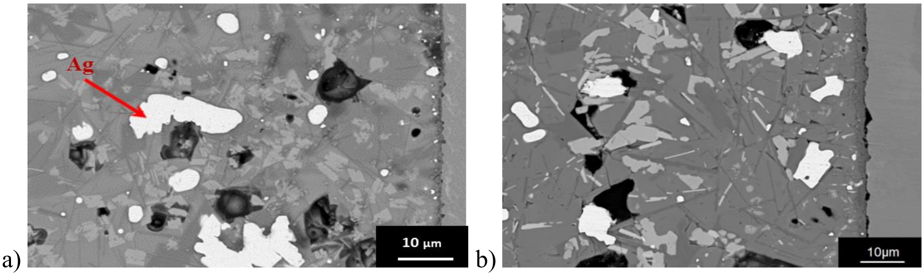

Figure 5-25: Microstructure of (a) as-sintered H-Ag and (b) annealed H-Ag.

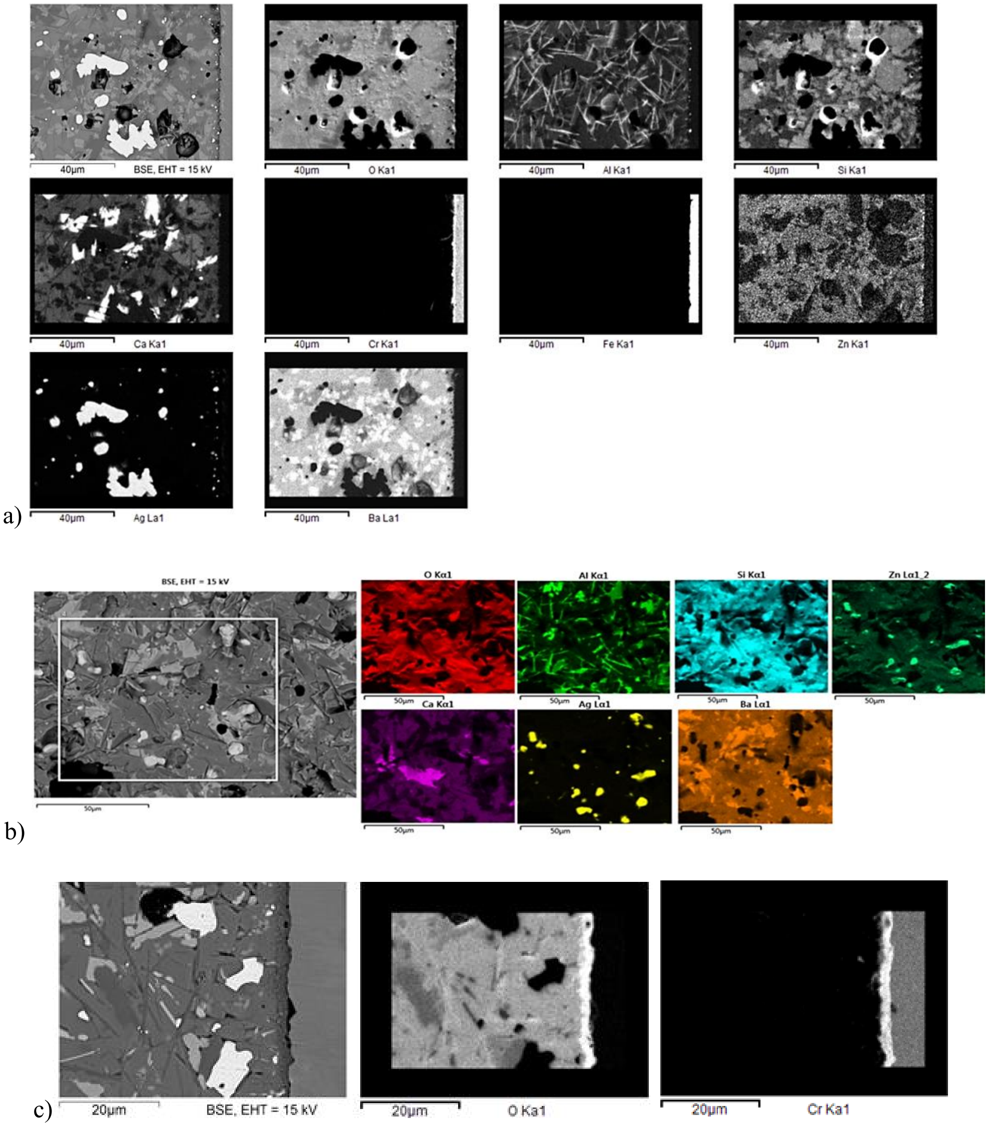

Figure 5-26: Elemental mapping of (a) as-sintered H-Ag; (b) and (c) annealed H-Ag.

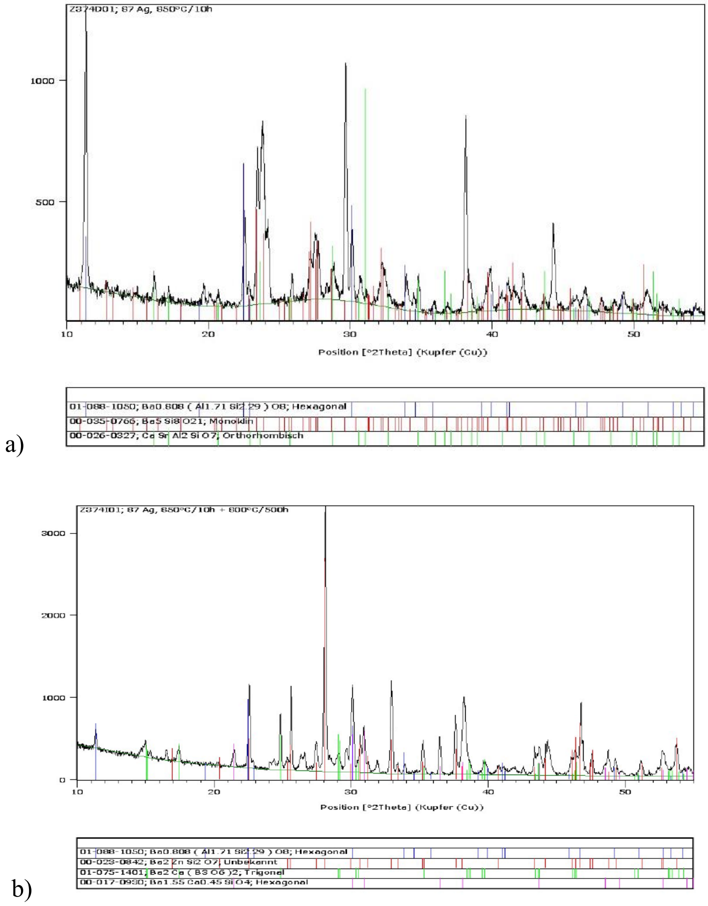

Figure 5-27: XRD patterns of (a) as-sintered H-Ag and (b) annealed state.

(2) H-F

Figure ***5-28*** illustrates the microstructure of the sealant H-F after 10 h joining and 1000 h annealing at 850°C, respectively. The microstructure consists of white YSZ fibers and black pores and the residual glassy phases. In fact, the sealant material appears to consist mostly of residual glassy phases; crystallized phases are almost absent. Microstructure in an annealed state shows an apparently higher amount of crystalline phases as shown in the bright phases in *Figure* ***5-28*** (*b*). It has also been reported that the fraction of crystallized phase is only around 8%, after

500 h annealing treatment, the crystallization is enhanced to ~ 25% [83]. The XRD patterns before and after 500 h annealing are shown in *Figure **5-29***.

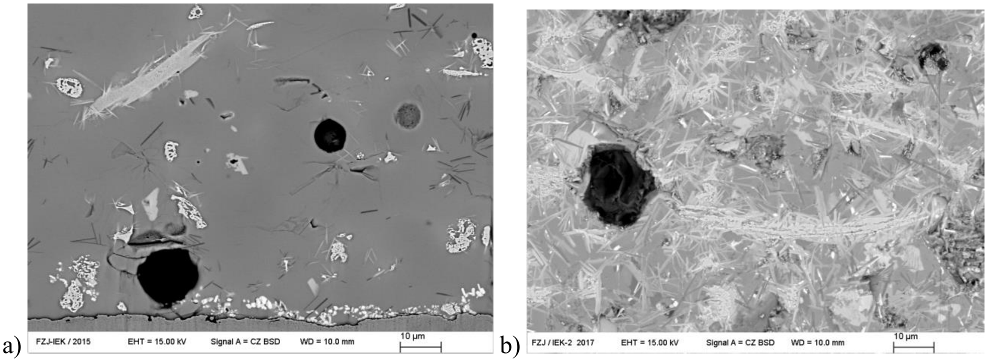

Figure 5-28: SEM image of H-F sealant materials with 850°C for (a) 10 hours joining, (b) 1000 hours annealing.

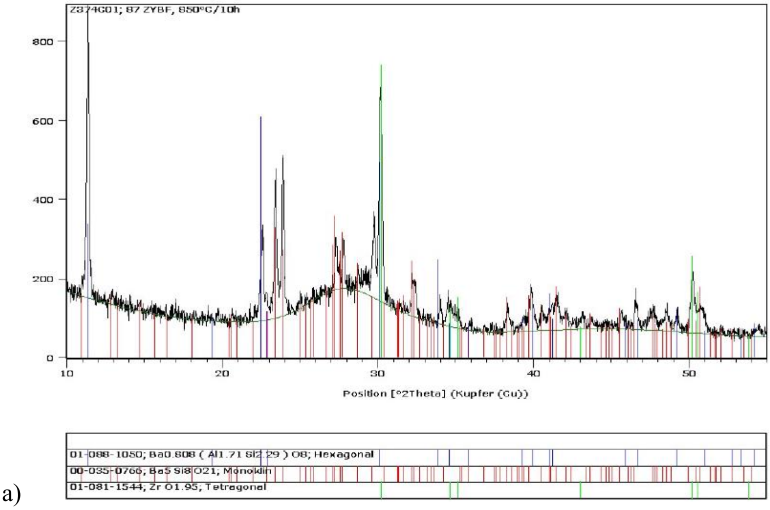

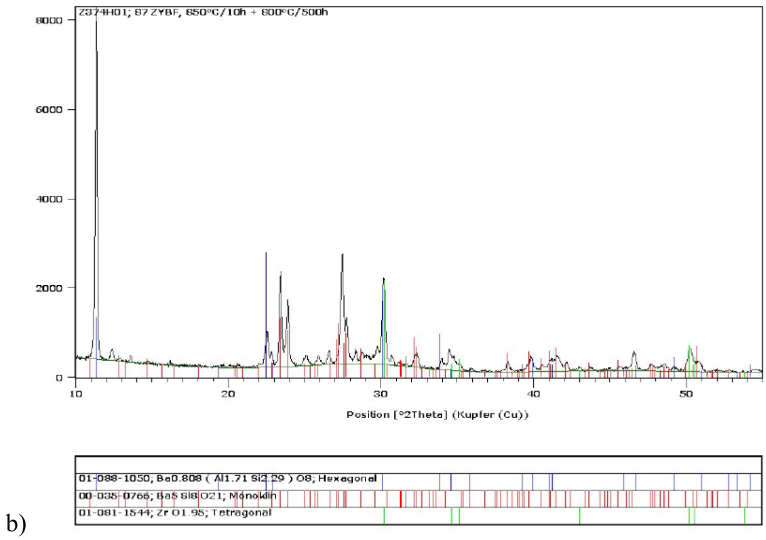

Figure 5-29: XRD patterns of (a) as-sintered H-F and (b) 500 h annealed state [83].

(3) 7.5 B(Ba)

The microstructures of as-sintered and annealed (800°C for 800 h) sealant 7.5B(Ba) are shown in *Figure* ***5-30***. The as-sintered sealant appears to be rather dense. *Figure* ***5-30*** *(b)* clearly shows the phases in the microstructure, where the white areas are barium silicate, the dark needle-shape areas are $BaMa_2Si_2O_7$ and the dark amorphous areas correspond to residual glassy phase as identified via complementary spot elemental analysis by EDX at CSIC, Madrid, Spain. After 800 h annealing treatment, a slightly increased porosity related to crystallization shrinkage can be seen and, with respect to the phases (see *Figure* ***5-30*** *(d)*), barium silicate is again visible without a defined stoichiometry as bright area, however, these phases seem to increase considerably in size and in proportion compared to the as-sintered state. Despite the increased amount of these barium silicate phases, the dark needle-shape phase $BaMg_2Si_2O_7$ is present as majority in the composition.

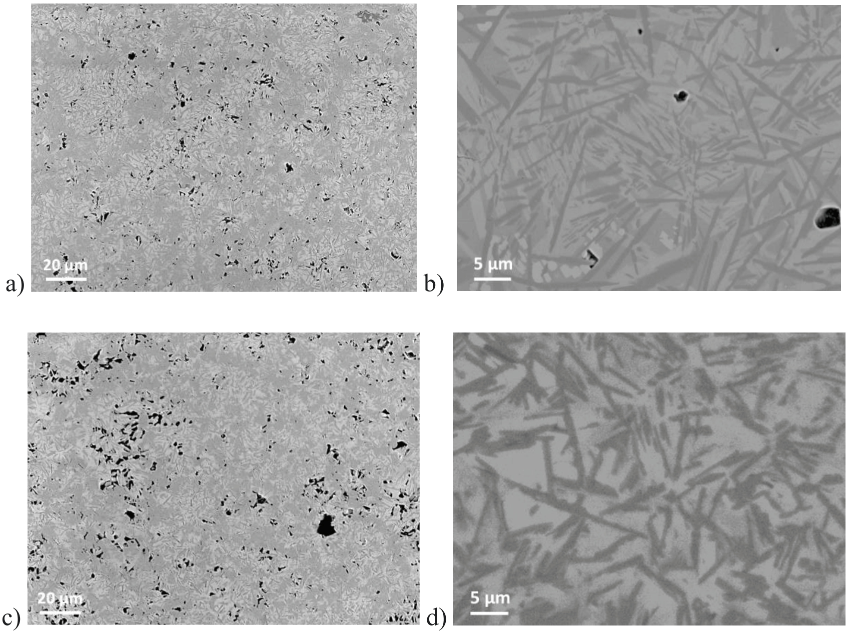

Figure 5-30: Microstructure of sealant 7.5 B(Ba): (a) and (b) as-sintered; (c) and (d) annealed at 800°C for 800 h [SEM images, CSIC, Madrid, Spain].

(4) 10 B(Sr)

Compared to the as-sintered 7.5 B(Ba) sealant, as-sintered 10 B(Sr) contains more glassy phases. The major grey background area is glassy phase as shown in *Figure* ***5-31*** *(a)* and *(b).* The light lumpy areas are crystallized $Sr_2MgSi_2O_7$ phases, while the darker lumpy areas are $SrMgSi_2O_6$ phases as identified via spot elemental analysis by EDX at CSIC, Madrid, Spain. Similar as for 7.5 B(Ba), the porosity of this sealant also increased after 800°C annealing treatment due to crystallization associated shrinkage. The crystallized phases grew during the annealing into larger and amorphous shapes, where the light areas are $Sr_2MgSi_2O_7$ and the light grey areas are $SrMgSi_2O_6$ (*Figure* ***5-31*** *(d)*), respectively. A small amount of glassy phase still remains, as seen as dark grey areas.

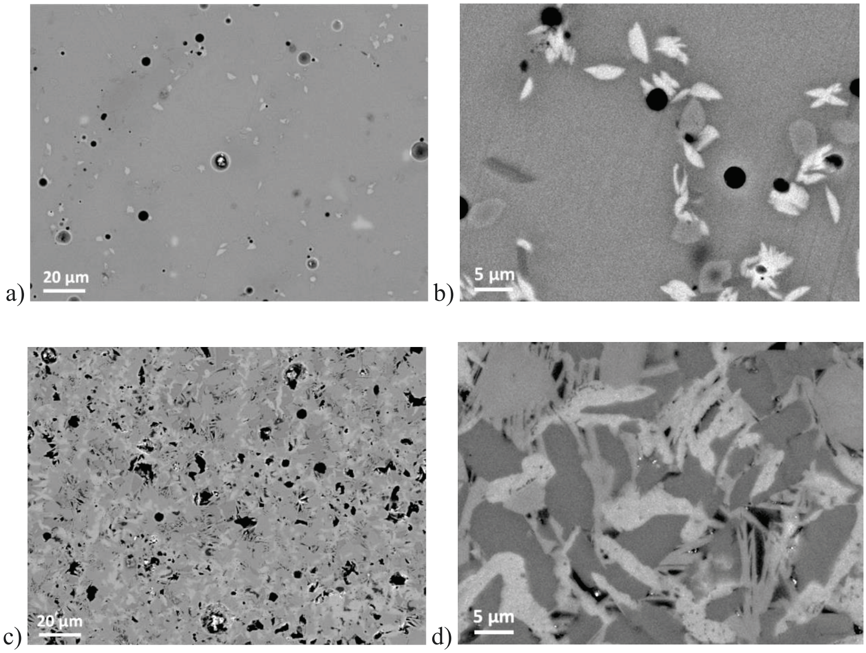

Figure 5-31: The microstructure of 10 B(Sr): a) and b) as-sintered; c) and d) annealed at 750°C for 800 h. [SEM images, CSIC, Madrid, Spain].

5.2.2. Bending fracture stress

5.2.2.1. Fracture stress comparison[2]

Fracture tests were carried out on head-to-head joined specimens at room temperature. The tensile surface was fine-grinded. For most sealant specimens, groups of different thickness in the range ~ 150 µm to 400 µm were tested to investigate if the bending fracture stress is affected by the thickness. For material H-F only specimens with one particular thickness were available.

The resulting average room temperature fracture stresses are presented in *Figure **5-32***, along with the previously derived data for the fully crystallized sealant B and the YSZ particle enhanced H-P sealant [49]. The sealant B is based on the BaO-CaO-SiO_2 ternary system similar as H-P, but with different compositions and with a small amount of Al_2O_3.

---

[2] Study has partly been published as J. Wei, G. Poćanac, et al., Ceram. Int. 41 (2015) 15122-15127 and J. Wei, G. Poćanac, et al., Proc. 12th Euro. SOFC & SOE Forum, Luzern, B0609, 2016.

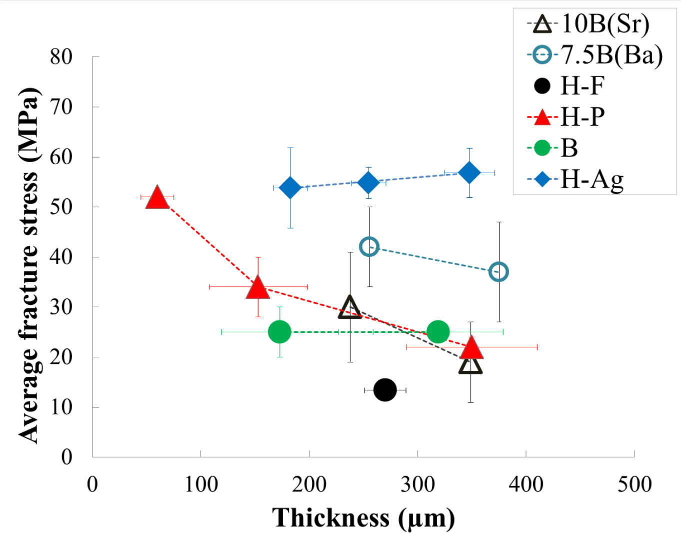

Figure 5-32: Average fracture stresses as a function of thickness at RT.

The comparison indicates an approximately two times higher average fracture stress of the H-Ag sealant for an SOFC stack typical sealant thickness of 200 to 300 µm, which implies that the ductile Ag particles significantly enhance the strength. Ag particles are able to increase crack energy by plastic deformation, which consumes energy. H-F shows a much lower fracture stress, indicating that the YSZ fibers do not yield a significant reinforcement at room temperature.

Previous results on H-P indicated a decrease in fracture stress with increasing sealant thickness [49], while no thickness dependency of fracture stress was found in the current study on the H-Ag material. An apparent thickness effects appears to exist for 10 B(Sr), while although a slight decrease is visible for 7.5 B (Ba), it is within the limits of experimental uncertainty. An effect of thickness on fracture stress can be a result of differences in thermal expansion of sealant and steel that lead to favorable compressive stresses that become lower for higher sealant thickness, see also [65].

5.2.2.2. Surface preparation effect

Three as-produced H-Ag specimens were tested without grinding to assess if surface preparation affects the mechanical behavior. The obtained average fracture stress (*Table **5-9***) was significantly lower than the average strength of the fine-grinded specimens, which is in agreement with a previous study on the H-P material [82], where it has been suggested that the fracture stress difference is a result of a stress concentration at the joining related to the wetting limitation during the sealing process. Another effect leading to a joining angle is obviously the friction between the sealant and the steel counterpart during the joining associated deformation. A possible difference in the microstructure between bulk and surface can be ruled out since the SEM analysis indicated a similar microstructure for the free surface. However, H-F results did not indicate a difference between fine-grinded and as-produced specimens. This might be related to differences in surface preparation used for the steel substrates. The corner of the steel bars used for joining H-F sealant is close to 90° with respect to the specimens' side, whereas the corner of the ones used for H-Ag was rounded due to excessive cutting edge removal. This indicates that a sharp corner of steel bars can have a positive effect on avoiding joining angle effects.

Table 5-9: Average fracture stress of fine-grinded and as-produced H-Ag and H-F head-to-head specimens.

Sealant	Preparation	Stress (MPa)
H-Ag	fine-grinded	55 ± 6
	As-produced	35 ± 6
H-F	fine-grinded	15 ± 2
	As-produced	13 ± 1

5.2.2.3. Elevated temperature tests

Since the sealants are exposed to high temperatures during the operation of SOFC stacks, the fracture stresses were also investigated at the elevated temperatures.

The average fracture stresses as a function of temperature are compiled in *Table **5-10***, where the value for the H-P sealant at 700°C is an estimate since the material deformed non-linearly above a stress of 30 MPa due to creep, and the accuracy of the rather low value for H-P at 800°C is limited by the experimental resolution [49]. Sealant 7.5 B(Ba) and 10 B (Sr) with rather small (~250 µm) and large (~350 µm) thickness were tested at 700°C and 800°C.

Table 5-10: Comparison of average fracture stresses for different as-sintered sealant materials (in MPa).

T (°C) Sealant	RT	700	800
H-Ag	55 ± 6	25 (1 test)	7 (1 test)
H-F	13 ± 1	53	viscous
H-P [49]	22 ± 2	Non-linear above ~ 30 MPa	1
B [49]	25 ± 2	x	30 ± 1
7.5 B(Ba)	42 ± 8 (~250 µm) 37 ± 10 (~350 µm)	x	11 ± 1 (~250 µm) 10 ± 0.3 (~350 µm)
10 B(Sr)	30 ± 11 (~250 µm) 19 ± 8 (~350 µm)	65 ± 9 (~250 µm) 38 ± 6 (~350 µm)	10 ± 0.3 (~250 µm)

Compared to the temperature independent behavior of the fully crystallized sealant B [65], the values of H-Ag revealed a drop of the fracture stress at 700°C, however, at 800°C the value is still higher than that obtained for the H-P sealant. The reason of significantly lower values at typical operation temperatures can be related to non-linear deformation of the remnant glassy phase, being also reflected in a non-linear deformation behaviour. The room temperature curves were linear, reflecting the brittle behavior of the material (*Figure **5-33***). The test at 700 °C already showed a nonlinear behavior, which suggests an influence of viscous deformation effects. These effects became even more pronounced at 800 °C.

While H-F sealant revealed an outstanding fracture stress at 700°C, a significant non-linear behavior can be seen from the load-displacement curve in *Figure **5-33***. This large non-linear behavior is a result of the larger amout of remaining glassy phase. H-F revealed a similar brittle behavior as H-Ag at room temperature. However, H-F sealant revealed an extremely strong viscous behavior at 800°C, where the specimen bended even under the experimentally necessary preload 2 N (~ 0.7 MPa).

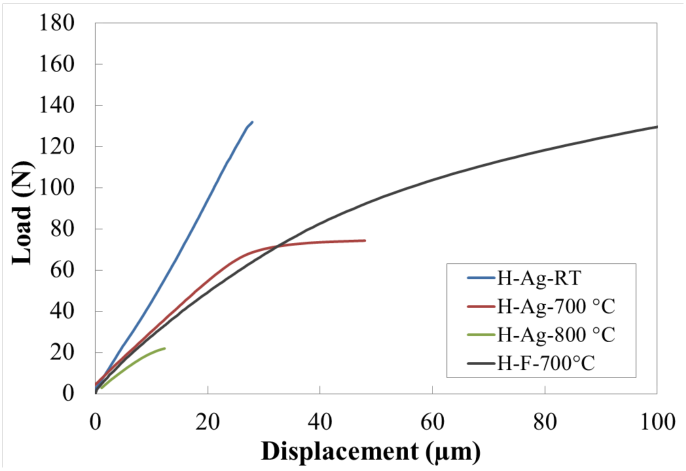

Figure 5-33: Load-displacement curves indicating non-linear behavior of the H-Ag and H-F sealant at elevated temperatures.

The sealant material 7.5 B(Ba) showed a similar behavior as the H-Ag material. The fracture behavior was brittle at room temperature and a significant drop in fracture stress at 800°C with some non-linear behavior occurred (see *Figure **5-34***). Sealant 10 B(Sr) displayed a similar behavior as H-F. The apparent fracture stress increases at significantly 700°C, while it decreases strongly at 800°C. The load-displacement curve also shows the significant non-linear behavior at 700°C, that again can be related to viscous behavior and in this case the failure stress appears again to be rather the deviation from linearity than the maximum sustainable stress (*Figure **5-34***).

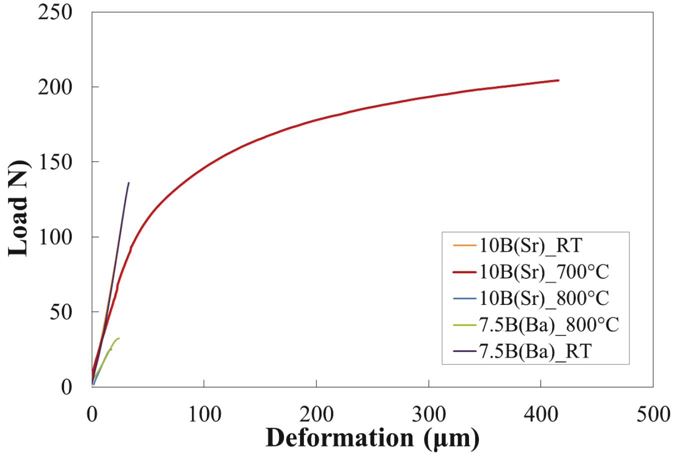

Figure 5-34: Load-displacement curves of 10 B(Sr) and 7.5 B(Ba) at room temperature and elevated temperature.

5.2.3. Annealing effects

Operation times exceeding 40.000 h are envisaged for stationary SOFC applications. Such long term exposures can lead to changes of the properties of the sealant and hence raise the need to characterize the properties as a function of annealing time. Therefore, similar mechanical tests were carried out on annealed specimens at room temperature and selected elevated temperature (700°C and 800°C).

Figure ***5-35*** compares room temperature average fracture stresses as a function of annealing time for different sealant materials. Very similar to H-P sealant, H-F shows an increase of the fracture stress with increasing annealing time, which indicates that the crystallization enhanced this property. However, material H-Ag revealed a contrary behavior, i.e. a decrease with increasing annealing time. Therefore, additional investigations were carried out to explain this behavior, which will be discussed in later sections.

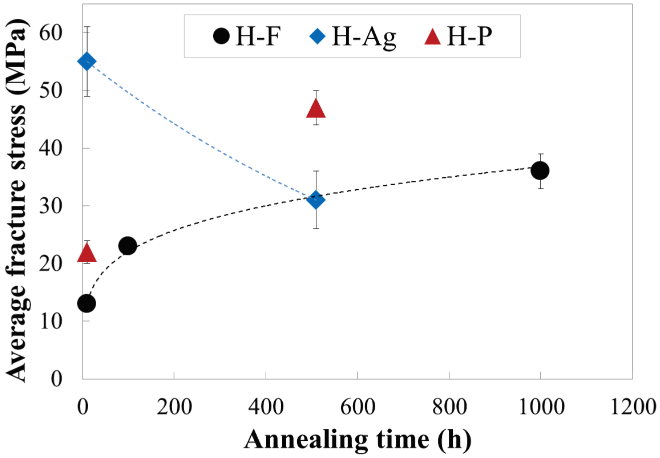

Figure 5-35: Relationship between the average fracture stress and annealing time for sealants H-Ag and H-F at RT.

All results from high temperature tests are compiled in (*Table* ***5-11***). Compared to the as-sintered condition, H-Ag displays a significantly lower fracture stress in annealed state at room temperature. The fracture stress of the annealed sealant decreases at 800°C. However, it preserves the fracture stress better than the as-sintered H-F. The 100 h annealed H-F has a higher fracture stress at room temperature and also at high temperature. It is very similar to the as-sintered H-P, i.e. the apparent fracture stress determined from the maximum load increases at 700°C due to non-linear deformation. After 1000 h annealing treatment, the fracture stress is rather invariant of temperature, indicating that almost full crystallization is reached. Compared to the H-Ag sealant, H-F appears to be advantageous for long-term application in SOFCs.

Table 5-11: Comparison of average fracture stresses for as-sintered and annealed sealants (in MPa).

T (°C) Sealant	RT	600	700	800
H-Ag	55 ± 6	x	25 (1 test)	7 (1 test)
H-Ag annealed /500h	31 ± 5	x	x	18 (1 test)
H-F	13 ± 1	x	53 (1 test)	x
H-F Annealed/100h	23 ± 1	x	50 (1 test)	6 ± 0.4
H-F Annealed/1000h	36 ± 3	29	32 (1 test)	29 (1 test)

Complementary SEM microstructure investigations aided the interpretation of annealing effects. Compared to the as-sintered material (*Figure* ***5-36*** *(a)*), Ag particles on the same particular position had a less rounded shape and decreased in size after just 10 h additional annealing at 800°C (*Figure* ***5-36*** *(b)*).

Previous work [52] suggests that, although the material is insulating in the as-sintered state, long-term annealing significantly increases its electrical conductivity. Hence, along with the SEM investigation it can be suggested that Ag probably percolates via diffusion along the grain boundaries which leads to a fracture stress decrease. The diffusion process and migration of Ag from the particles into the glass matrix during annealing can also occur due to reactions involving polyvalent ions like vanadium in the glass-matrix. The Ag incorporation into glass-ceramic matrix can lead to volume expansion and increased brittleness associated with the formation of micro-cracks. Such micro-cracks will reduce stiffness and fracture stress. The lower apparent elastic modulus of the annealed sealant (132 ± 6 GPa) obtained from 4-point bending test, compared to the as-sintered sealant (165 ± 10 GPa) supports this assumption. *Figure* ***5-37*** shows micro-cracks in the annealed sealant and load-deformation curves in the as-sintered and annealed state. The fracture stress of the annealed sealant showed a decrease at 800°C, however, it preserves its strength better than the as-sintered H-Ag (*Table* ***5-11***).

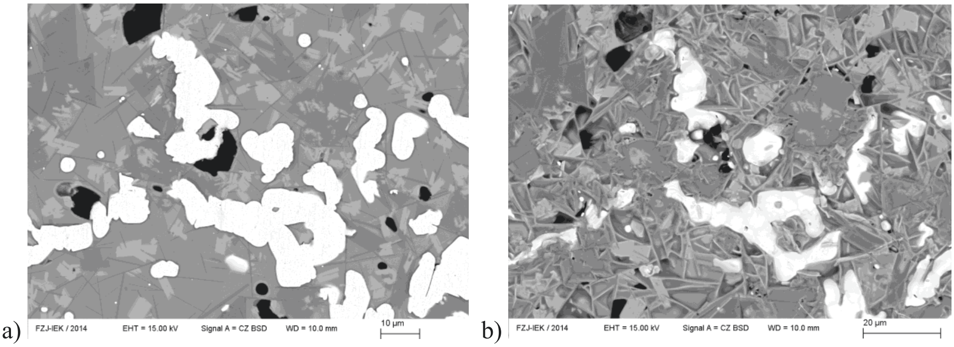

Figure 5-36: SEM image revealing the change of Ag particles already after only of 10 h annealing at 800°C. The particles became smaller and spread more over the glass matrix.

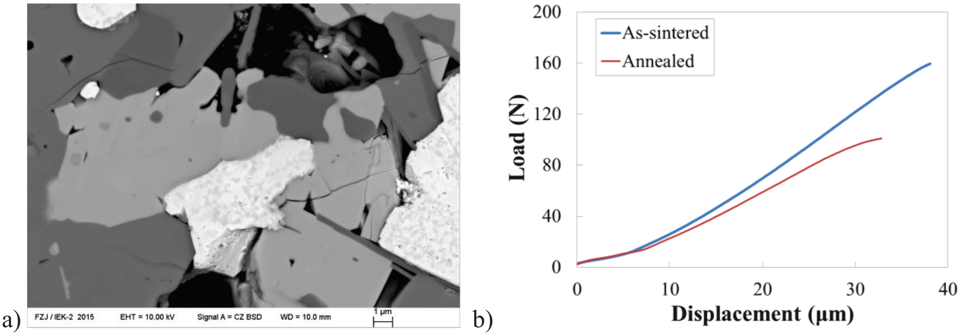

Figure 5-37: (a) Microstructure of the annealed sealant contained the micro-cracks; (b) Load-displacement curves for the as-sintered and annealed specimen confirming an annealing effect onto the sealants ductility.

5.2.4. Complementary 3-point-bending tests on 7.5 B(Ba) and 10 B(Sr) bar specimens

Additional tests were carried out on bar specimens to assess the bulk properties. The results are summarized in *Table* ***5-12***.

7.5 B(Ba) after 24 h heating treatment reveals a significant decrease of fracture stress at 800°C due to viscosity of the residual glassy phases, while for the longer annealing time the fracture stress is rather independent of temperature. Hence, crystallization appears to be completed.

10 B(Sr) after 24 h revealed a similar fracture stress at room temperature and 650°C, which indicates a negligible viscous deformation effect due to glassy phases at 650°C. The specimen showed extremely strong viscous behavior at 800°C due to the high amount of glassy phases, where the specimen deformed significantly without fracture, hence as suggested by the project partner CISC, Madrid, the testing temperature was reduced to 650°C.

Crystallization is expected to be almost completed after 800 h heating treatment, which is confirmed by the similar fracture stress at room temperature and 800°C for annealed specimens.

A previous work [65] revealed an average fracture stress of 91 ± 12 MPa at room temperature and ~ 90 MPa at 800°C for Jülich bar-shaped B type sealant, which is a material sintered at 950°C for 10 h. Compared with 7.5 B(Ba) and 10 B(Sr), sealant B has hence a superior fracture stability, while Jülich bar-shaped H-P sealant yielded much lower fracture stress 28 ± 3 MPa at room temperature and ~1 MPa at 800 °C, indicating a lower elevated temperature stability compared with 7.5 B(Ba) and 10 B(Sr).

Table 5-12: Average fracture stress (in MPa) obtained from 3-point-bending tests on bar type specimens.

Sealant	Pre-treatment	RT	650°C	800°C
7.5 B(Ba)	24h/800°C	81 ± 5		25 ± 4
	800h/800°C	63 ± 7		72 ± 2
10 B(Sr)	24h/750°C	101 ± 18	92 ± 8	
	800h/750°C	68 ± 9		84 ± 17

5.2.5. Shear strength[3]

5.2.5.1. Sealant H-Ag

Torsion tests of the H-Ag sealant at RT after 10 h joining at 850 °C yielded similar an average fracture stress (61 ± 4 MPa) as obtained from bending tests on head-to-head specimens (55 ± 6 MPa). A comparison of bending and shear stress of H-Ag sealant is shown in *Figure **5-38***. Two tests at 600°C resulted in a similar shear stress of 64.1 ± 0.3 MPa, indicating that residual

---

[3] Study has partly been submitted for publication as J. Wei, G. Pećanac, et al., Proc. 12th Euro. SOFC & SOE Forum, Luzern, B1309, 2016.

stresses induced by thermal mismatch of sealant and steel, which are maximum at RT, do not affect the torsion test. A single test at 800°C revealed a non-linear loading behavior of H-Ag specimens and a significant decrease in shear fracture stress (13 MPa), similar as previously observed for head-to-head joined bending specimen (7 MPa, see above). This decrease in the fracture stress can be associated with the softening of the sealant above the glass transition temperature T_g due to residual glassy phases that also led to noticeable creep effects reported for head-to-head joined bending specimens.

Testing of a specimen after joining for 100 h at 850°C, to simulate the effect of longer stack operation, yielded a lower RT shear failure stress (14 MPa). A similar effect has been reported for annealed H-Ag head-to-head joined bending specimens. Such a decrease in fracture stress has obvious implications for the sealant application in stacks.

Failure in bending tests appeared to be predominant via cracking through the glass-ceramic close to the interface with the steel (oxide scale did not delaminate), i.e. the fracture path in case of RT and elevated temperature torsion test specimens was the interface of the oxide scale with the steel as shown in *Figure **5-39***.

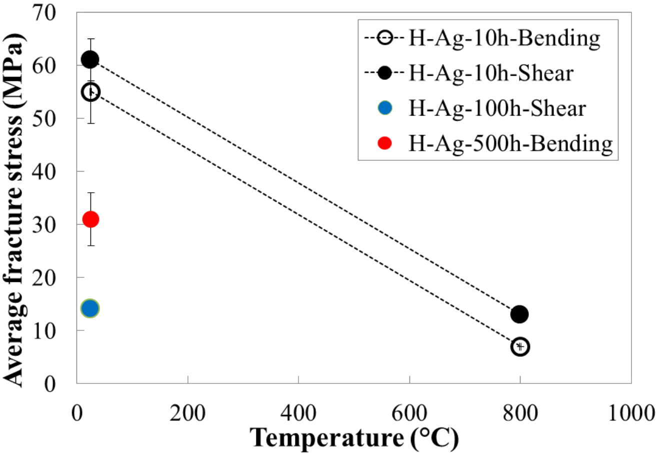

Figure 5-38: Comparison of bending and shear stress of H-Ag sealant.

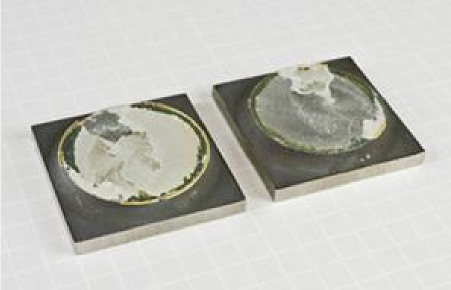

Figure 5-39: Fractured specimen of H-Ag after the torsional shear test at RT.

5.2.5.2. Sealant H-F

Due to the load limit of the set-up it was not possible to induce RT failure for 10 h joined specimens, implying that the shear stress is higher than 68.6 MPa, indicating a much higher shear stress value than bending stress (13 ± 1 MPa) obtained from head-to-head specimens. At 800°C, a similar value (17 MPa) as for H-Ag was obtained, where the bending stress of H-F could not be determined due to extreme deformation of head-to-head specimen. The shear stresses obtained from torsion tests are listed in *Table **5-13***.

For 100 h joined specimens the average torsional shear failure stress was 58 ± 8 MPa (for the single test where failure did not occur up to the maximum applicable stress of 68.6 MPa, this particular stress was assumed to be the failure stress), hence being slightly lower than for the 10 h joining case. However, compared to bending stress (23 ± 1 MPa, see above) obtained from head-to-head specimens, the shear stress is still much higher (see *Figure **5-40***). The value at 600 °C was similar as at RT indicating again that residual stresses do not affect failure stress.

In an initial elevated temperature loading experiment at 660°C failure could not be initiated and deformation was dominated by plastic deformation of the steel. Nevertheless, the same specimen was subsequently loaded at 760°C, where failure of the sealant occurred (see *Figure **5-41** (a)*). The fracture shear stress of 15 MPa obtained in this test agreed with the one obtained in a subsequent test of another specimen at 800°C (16.5 MPa), which contrary to the previous test was rather unbiased by deformation of the steel (*Figure **5-41** (a)*). The test at 760°C was not repeated again, since the further test was carried out at 800°C successfully, which is a more relative operation temperature in SOFC. The first specimen loaded initially at 660°C could sustain a higher torsion moment since it was tested below seal softening temperature. At this temperature the steel was less creep resistant than the sealant. The second specimen was tested above the softening temperature and hence a lower moment was necessary.

Hence, it can be concluded from these tests that pre-deformation due to plasticity of the Crofer22APU steel does not affect the maximum applied and sustained shear stress of the sealant material. The loading curve indicated that the maximum sustainable moment, at which plastic deformation of the steel started at 660°C was ~ 15 % lower than the sealant failure moment at RT, implying that at this temperature (below T_g) the sealant has almost the same shear strength as at RT. At 760°C and 800°C the sustainable moment and, hence, also the shear strength was reduced by a factor of almost three due to softening of the sealant, but it is still higher than bending stress at 800°C.

Contrary to H-Ag that revealed the same failure mode at RT and high temperature in the torsion tests, the failure mode of H-F changed from interfacial failure at RT to cracking through the glass-ceramic at high temperatures (see *Figure **5-41** (b)*); indicating that below the softening temperature the interface is the weakest position in torsional loading, whereas above the sealant is weaker than the interface. Contrary to this, bending tests on head-to-head joined H-F specimens yielded similar crack paths through the sealant at RT and elevated temperatures, indicating differences in the ratio of torsion and bending strength of sealant and interface at room and elevated temperature, respectively. Although similar interfacial failure was found for the H-Ag sealant at RT and elevated temperature, the measured shear stress was also in this case significantly lower than at room temperature. Hence, contrary to the H-F material, where temperature dependency of properties of sealant and interface appear to differ, in case of H-Ag they appear to be related, i.e. the elevated temperature sustainable shear stress appears to be affected by a softening effect, implying that from a structural point of view interface and sealant in the case of H-Ag are more similar than in the case of H-F.

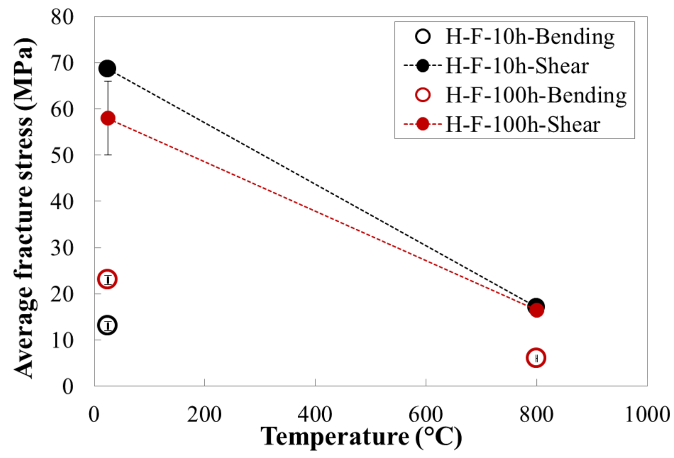

Figure 5-40: Comparison of bending and shear stress of as-sintered H-F and 100 h annealed state.

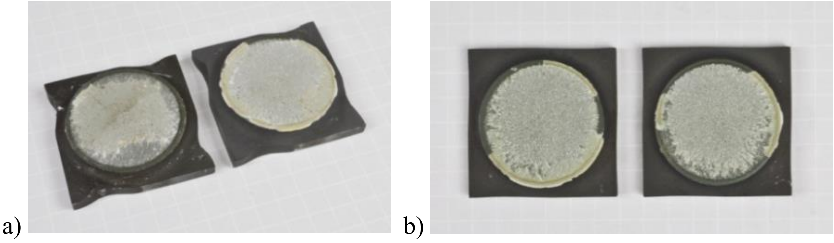

Figure 5-41: Fracture H-F specimens after torsion tests: (a) testing at 600/760 °C; (b) testing at 800°C.

Table 5-13: Results from torsion tests at room temperature and elevated temperatures.

Sealant	Joining (h)	Temp. (°C)	Shear stress (MPa)	Average shear stress (MPa)
H-Ag – Crofer22APU	10	RT	59.2	61 ± 4
		RT	57.0	
		RT	65.3	
		600	64.4	64.1 ± 0.3
		600	63.8	
		800	12.5	12.5
	100	RT	14.0	14.0
H-F – Crofer22APU	10	3 Test, RT	> 68.6	> 68.6
		800	17.1	17.1
	100	RT	48.6	58 ± 8
		RT	50.1	
		RT	57.4	
		RT	> 68.6	
		RT	65.9	
		600	58.9	58.9
		760	15.2	15.2
		800	16.5	16.5

In this section, various sealants were investigated by different testing method on as-sintered and annealed states. The bending fracture stresses were determined by 4-point bending test on head-to-head specimens, which mimic the real situation of stacks. The diffusion of Ag particles led to micro-cracks in matrix and decreased the fracture stress. Shear stresses were observed by torsion tests at room temperature and elevated temperatures.

6. Conclusions

Ceramic cells and sealants are critical components for the long term reliable operation of SOFC stacks and systems. With respect to cells, different NiO-YSZ compositions along with its reduced state have been investigated systematically in this work as the typical anode materials for SOFCs application. With respect to sealants, materials developed in Jülich and from CSIC, Madrid, Spain were characterized. H-Ag sealant as a revised H matrix sealant with Ag particles reinforcements has been tested to observe the mechanical performance at room temperature and operating temperature. Additional tests on 7.5 B(Ba) and 10 B(Sr) developed in Spain provide complementary results for the sealant study and comparison. Properties choice was based on observed and reported issues, leading to an assessment of fracture toughness and creep for the anode substrate materials and mainly strength for the sealants. All data were discussed and compared to previous results.

Anode materials

Based on improved testing procedures, the fracture toughness of different anode substrate materials has been determined. This study has shown that in general, when attempting to analyze material´s fracture toughness with a double-torsion test, pre-tests should be performed to analyze whether the particular material needs a pre-crack before the double-torsion test. Such tests were carried out in the current study, confirming that the thin NiO-3YSZ material can be tested without a pre-crack, whereas for the thicker NiO-8YSZ material such pre-cracks are necessary. Furthermore, DT tests with different displacement rates are necessary to assess the range in which the fracture toughness evaluation is not biased by a subcritical crack growth effect.

The derived fracture toughness of NiO-3YSZ was higher than that of NiO-8YSZ, which can be ascribed to the transformation toughening that occurs for 3YSZ composition, indicating the advantage of the former for the use as an SOFC anode substrate during processing and joining. NiO-3YSZ yields a lower fracture toughness at 800 °C compared to room temperature, which is caused by a decrease of transformation toughening of 3YSZ at elevated temperatures. On the other hand, NiO-8YSZ revealed a high-temperature thermo-mechanical stability and kept its fracture toughness even at 800 °C, however, with a still lower absolute value than that obtained for NiO-3YSZ.

Reduction of NiO-8YSZ leads to higher fracture toughness compared to the oxidized state due to the ductility of Ni. A smaller increase in fracture toughness in the reduced state suggests that the 3YSZ based composites is less affected by the ductility of Ni particles, indicating that in the development of anode substrates with high fracture toughness also other microstructural aspects like Ni – YSZ ratio, grain and pore size, need consideration as also indicated by a comparison of the results of oxidized and reduced 8YSZ based composited of different porosity with data quoted in literature.

Results also imply that in the envisaged SOFC application long term reliability of cells in the reduced state will be challenged by subcritical crack growth effects, where future studies should consider also SCG at elevated temperatures under the respective large moisture containing hydrogen atmosphere. NiO-8YSZ tested using the current re-oxidation procedure revealed a higher fracture toughness than in the initial oxidized state. This high fracture toughness is ascribed in the current study to Ni cores which remained inside the NiO particles after the re-oxidation.

In the current work, three common-used testing methods to assess the materials creep behavior were carried out and compared systematically. Compressive tests are considered as the most direct and probably most reliable way to obtain creep parameters for ceramic materials where simple tensile testing is not an option. Bending tests are easier to carry out and, especially for the case of solid oxide fuel cell anode substrate materials, close to the real case due to the materials' geometry. Four-point bending tests yielded rather accurate data, while the disadvantage is the limitation of applied loads. Using too low loads obviously renders data acquisition difficultly, whereas too high loads can cause fracture of specimens. Due to the larger specimen size, ring-on-ring test can applied over a rather wide range of applied loads, while the equation used for analysis possesses limits, i.e. it can be used for approximation of the materials behavior only if the stress exponent is ~ 1.

Hence, overall the creep behavior of Ni-8YSZ anode materials was investigated by different testing methods. A diffusion-dominated creep mechanism of Ni-8YSZ was found for both compressive and tensile creep, while the activation energies show a dependence on the material´s composition, probably also related to temperature and loading modes. Porosity significantly reduces the creep resistance and yields larger creep rates. For the considered material composition, it appears that YSZ carries most of the load during creep.

FEM simulation was carried out to assess the limitations of equations used for creep evaluations, especially in case of the more critical ring-on-ring test. The discrepancy of the equation for ring-on-ring creep becomes larger with increasing stress exponent deviating from the value of unity. The creep behavior obtained in this work can be used as important input data for validation and modeling of SOFC/SOEC stacks. The change of the stress distribution with time should be taken into account for long-term application under stress exposure for stack operation.

With respect to the chosen composition, obviously, a material with high YSZ content would have better creep resistance. Although enhanced creep resistance would increase long-term stability, functional properties need to be the main consideration in compositional and porosity optimized materials development.

Sealant materials

Reinforcing the glass-ceramic sealant with Ag particles yielded a positive effect on the materials' mechanical behavior in its initial state. The comparison based on the bending tests with previously tests H-P and B sealant variants revealed an approximately two times higher average fracture stress of the H-Ag sealant. A thickness dependency of the fracture stress was not found for the H-Ag material, while the analysis with respect to temperature dependency revealed a strength decrease already at 700°C, whereas at 800°C the bending test derived fracture stress was still higher than that of the YSZ particle reinforced variant H-P. The reason for the significantly lower values at typical operation temperatures can be associated with the residual glassy phase. Compared to the H-Ag material, H-F, 10 B(Sr) and 7.5 B(Ba) yielded lower fracture stresses at RT. However, a similar non-linear behavior at high temperature was found for these materials, but H-F indicated a much higher fracture stress at 700°C and extremely large deformation at

800°C. An apparent thickness effects was found for 10 B(Sr), while the sealant 7.5 B(Ba) did not reveal such an effect within the limits of experimental uncertainty.

Bending tests were carried out for annealed H-Ag and H-F head-to-head specimens. H-Ag revealed a lower average fracture stress compared to the respective as-sintered sealant; an opposite effect to the one previously reported for the sealant H-P. SEM analysis indicated that for the annealed material, the Ag particles distribute more evenly through the microstructure, where it appeared that Ag incorporation into the glass-ceramic matrix leads to micro-cracks and lowers the fracture stress. The annealed sealant revealed also a fracture stress decrease at 800°C; however, the fracture stress is better preserved than for the as-sintered material. H-F showed an increase of the fracture stress with increasing annealing time, indicating that crystallization enhances this property for this particular material. H-F with 1000 h annealing yielded a rather temperature independent fracture stress (RT, 700°C, 800°C).

The two Jülich sealant materials have been characterized using a torsion set-up at RT and elevated temperatures. The results indicate that, similar as for the bending test, the obtained values are rather insensitive to residual stresses that are mainly induced by the thermal expansion mismatch of sealant and steel. Both sealant materials show a pronounced decrease of the shear strength above their softening temperature. Ag reinforced sealant material shows a decrease of the shear strength for longer annealing time, a similar effect was observed for the bending strength of head-to-head joined specimens, while such an effect was not observed for the YSZ fiber reinforced material. Contrary to the Ag particle reinforced sealant, the H-F material revealed a change in fracture mode from interfacial to cracking through the sealant at elevated temperatures, indicating that at RT the weakest position is located at the oxide scale, whereas at high temperatures the sealant becomes weaker due to the softening of the material. An obvious implication is that progressive annealing that might enhance the properties of the sealant material, will not necessarily lead to higher shear strength at RT, where the properties and the behavior with respect to long term temperature exposure of the oxide scale dominates. Typically oxide scales become thicker and weaker for longer annealing time. Note, for bending tests failure through the sealant was observed at all temperatures. The complex loading situation in a stack requires consideration of both, shear and bending/tensile strengths.

7. References

[1] J. Gibbins, H. Chalmers, Carbon capture and storage, Energy Policy, 36 (2008) 4317-4322.

[2] V. Ramanathan, Air pollution, greenhouse gases and climate change: Global and regional perspectives, Atmospheric Environment, 43 (2009) 37-50.

[3] A.B. Stambouli, E. Traversa, Solid oxide fuel cells (SOFCs): A review of an environmentally clean and efficient source of energy, Renew Sust Energ Rev, 6 (2002) 433-455.

[4] S.C. Singhal, K. Kendall, Chapter 1 - Introduction to SOFCs, in: S.C. Singhal, K. Kendal (Eds.) High Temperature and Solid Oxide Fuel Cells, Elsevier Science, Amsterdam, 2003, pp. 1-22.

[5] P. Knauth, H.L. Tuller, Solid-state ionics: Roots, status, and future prospects, Journal of the American Ceramic Society, 85 (2002) 1654-1680.

[6] N.Q. Minh, T. Takahashi, Chapter 1 - Introduction, in: N.Q.M. Takahashi (Ed.) Science and Technology of Ceramic Fuel Cells, Elsevier Science Ltd, Oxford, 1995, pp. 1-14.

[7] H. Yokokawa, H.Y. Tu, B. Iwanschitz, A. Mai, Fundamental mechanisms limiting solid oxide fuel cell durability, Journal of Power Sources, 182 (2008) 400-412.

[8] N. Laosiripojana, W. Wiyaratn, W. Kiatkittipong, A. Arpornwichanop, A. Soottitantawat, S. Assabumrungrat, Reviews on solid oxide fuel cell technology, Engineering Journal, 13 (2009) 65-84.

[9] L. Blum, W.A. Meulenberg, H. Nabielek, R. Steinberger-Wilckens, Worldwide SOFC technology overview and benchmark, International Journal of Applied Ceramic Technology, 2 (2005) 482-492.

[10] J. Larminie, A. Dicks, J. Larminie, A. Dicks, Fuel cell systems analysed, in: Fuel Cell Systems Explained, John Wiley & Sons, Ltd,. 2013, pp. 369-389.

[11] K.C. Wincewicz, J.S. Cooper, Taxonomies of SOFC material and manufacturing alternatives, Journal of Power Sources, 140 (2005) 280-296.

[12] F. Tietz, Thermal expansion of SOFC materials, Ionics, 5 (1999) 129-139.

[13] A. Weber, E. Ivers-Tiffee, Materials and concepts for solid oxide fuel cells (SOFCs) in stationary and mobile applications, Journal of Power Sources, 127 (2004) 273-283.

[14] N.Q. Minh, Ceramic Fuel-Cells, Journal of the American Ceramic Society, 76 (1993) 563-588.

[15] H.P. Buchkremer, R. Conradt, Durable sealing concepts with glass sealants or compression seals, in: Handbook of Fuel Cells, John Wiley & Sons, Ltd, 2010.

[16] M.K. Mahapatra, K. Lu, Thermochemical Compatibility of a Seal Glass with Different Solid Oxide Cell Components, International Journal of Applied Ceramic Technology, 7 (2010) 10-21.

[17] N.H. Menzler, W. Schafbauer, F. Han, O. Buchler, R. Mucke, H.P. Buchkremer, D. Stover, Development of high power density solid oxide fuel cells (SOFCs) for long-term operation, Mater Sci Forum, 654-656 (2010) 2875-2878.

[18] N. Christiansen, H. Holm-Larsen, S. Primdahl, M. Wandel, S. Ramousse, A. Hagen, Recent progress in development and manufacturing of SOFC at Topsoe Fuel Cell A/S and Riso DTU, Solid Oxide Fuel Cells 12 (Sofc Xii), 35 (2011) 71-80.

[19] M. Bertoldi, O. Bucheli, S. Modena, D. Larrain, A. Ravagni, Manufacturing and market-oriented development of SOFC generators at SOFCpower SpA, Solid Oxide Fuel Cells 12 (Sofc Xii), 35 (2011) 127-138.

[20] W.A. Meulenberg, N.H. Menzler, H.P. Buchkremer, D. Stöver, Manufacturing Routes and State-of-the-Art of the Planar Jülich Anode-Supported Concept for Solid Oxide Fuel Cells, in:

Materials for Electrochemical Energy Conversion and Storage, The American Ceramic Society, 2006, pp. 99-108.

[21] J. Koong, K. Sun, D. Zhou, J. Qiao, J. Li, Anode-supported IT-SOFC anode prepared by tape casting technique, in: 2006 International Forum on Strategic Technology, 2006, pp. 186-189.

[22] N.H. Menzler, J. Malzbender, P. Schoderböck, R. Kauert, H.P. Buchkremer, Sequential tape casting of anode-supported solid oxide fuel cells, Fuel Cells, 14 (2014) 96-106.

[23] R. Knibbe, J. Hjelm, M. Menon, N. Pryds, M. Sogaard, H.J. Wang, K. Neufeld, Cathode-electrolyte interfaces with CGO barrier layers in SOFC, Journal of the American Ceramic Society, 93 (2010) 2877-2883.

[24] S. Islam, J.M. Hill, CHAPTER 4 Anode Material Development, in: Solid Oxide Fuel Cells: From Materials to System Modeling, The Royal Society of Chemistry, 2013, pp. 88-105.

[25] T. Takeguchi, R. Kikuchi, T. Yano, K. Eguchi, K. Murata, Effect of precious metal addition to Ni-YSZ cermet on reforming of CH4 and electrochemical activity as SOFC anode, Catalysis Today, 84 (2003) 217-222.

[26] S.F. Corbin, R.M.C. Clemmer, Q. Yang, Development and characterization of porous composites for solid oxide fuel cell anode conduction layers using ceramic-filled highly porous Ni foam, Journal of the American Ceramic Society, 92 (2009) 331-337.

[27] M. Koyama, H. Kohno, T. Ogura, T. Ishimoto, Applications of computational chemistry to designing materials and microstructure in fuel cell technologies, Journal of Computer Chemistry, Japan, 12 (2013) 1-7.

[28] S. Tao, J.T. Irvine, A redox-stable efficient anode for solid-oxide fuel cells, Nature Materials, 2 (2003) 320-323.

[29] J.T.S. Irvine, A. Sauvet, Improved Oxidation of Hydrocarbons with New Electrodes in High Temperature Fuel Cells, Fuel Cells, 1 (2001) 205-210.

[30] D.W. Dees, T.D. Claar, Conductivity of porous Ni / ZrO_2-Y_2O_3 cermets Journal of The Electrochemical Society, 134 (1987) 2141-2146.

[31] E. Ivers-Tiffée, W. Wersing, M. Schießl, H. Greiner, Ceramic and metallic components for a planar SOFC, Berichte der Bunsengesellschaft für physikalische Chemie, 94 (1990) 978-981.

[32] J.H. Lee, H. Moon, H.W. Lee, J. Kim, J.D. Kim, K.H. Yoon, Quantitative analysis of microstructure and its related electrical property of SOFC anode, Ni–YSZ cermet, Solid State Ionics, 148 (2002) 15-26.

[33] A. Atkinson, S. Barnett, R.J. Gorte, J.T. Irvine, A.J. McEvoy, M. Mogensen, S.C. Singhal, J. Vohs, Advanced anodes for high-temperature fuel cells, Nature Materials, 3 (2004) 17-27.

[34] F. Frusteri, G. Italiano, C. Espro, F. Arena, CH_4 decomposition on Ni and Co thin layer catalysts to produce H_2 for fuel cell, Catalysis Today, 171 (2011) 60-66.

[35] N.Q. Minh, Solid oxide fuel cell technology—features and applications, Solid State Ionics, 174 (2004) 271-277.

[36] D. Simwonis, H. Thülen, F.J. Dias, A. Naoumidis, D. Stöver, Properties of Ni/YSZ porous cermets for SOFC anode substrates prepared by tape casting and coat-mix® process, Journal of Materials Processing Technology, 92–93 (1999) 107-111.

[37] L. Blum, L.G.J. de Haart, J. Malzbender, N.H. Menzler, J. Remmel, R. Steinberger-Wilckens, Recent results in Jülich solid oxide fuel cell technology development, Journal of Power Sources, 241 (2013) 477-485.

[38] J.W. Fergus, Oxide anode materials for solid oxide fuel cells, Solid State Ionics, 177 (2006) 1529-1541.

[39] S.K. Pratihar, A. Dassharma, H.S. Maiti, Processing microstructure property correlation of porous Ni–YSZ cermets anode for SOFC application, Materials Research Bulletin, 40 (2005) 1936-1944.
[40] V.Vasechko, Thermo-mechanical investigation of reoxidation-stable material concepts for solid oxide feul cells, in, RWTH Aachen, 2014.
[41] S. Majumdar, T. Claar, B. Flandermeyer, Stress and Fracture Behavior of Monolithic Fuel Cell Tapes, Journal of the American Ceramic Society, 69 (1986) 628-633.
[42] B.A. Horri, C. Selomulya, H. Wang, Modeling the Influence of Carbon Spheres on the Porosity of SOFC Anode Materials, Journal of the American Ceramic Society, 95 (2012) 1261-1268.
[43] T. Kawada, S. Watanabe, S.-i. Hashimoto, T. Sakamoto, A. Unemoto, M. Kurumatani, K. Sato, F. Iguchi, K. Yashiro, K. Amezawa, K. Terada, M. Kubo, H. Yugami, T. Hashida, J. Mizusaki, Classification of mechanical failure in SOFC and strategy for evaluation of operational margin, ECS Transactions, 25 (2009) 467-472.
[44] K. Kwok, P.S. Jorgensen, H.L. Frandsen, Computation of effective steady-state creep of porous Ni-YSZ composites with reconstructed microstructures, Journal of the American Ceramic Society, 98 (2015) 2873-2880.
[45] D. Fouquet, A.C. Müller, A. Weber, E. Ivers-Tiffée, Kinetics of oxidation and reduction of Ni/YSZ cermets, Ionics, 9 (2003) 103-108.
[46] G. Stathis, D. Simwonis, F. Tietz, A. Moropoulou, A. Naoumides, Oxidation and resulting mechanical properties of Ni/8Y_2O_3-stabilized zirconia anode substrate for solid-oxide fuel cells, Journal of Materials Research, 17 (2011) 951-958.
[47] J. Malzbender, E. Wessel, R.W. Steinbrech, Reduction and re-oxidation of anodes for solid oxide fuel cells, Solid State Ionics, 176 (2005) 2201-2203.
[48] F. Smeacetto, A. De Miranda, A. Chrysanthou, E. Bernardo, M. Secco, M. Bindi, M. Salvo, A.G. Sabato, M. Ferraris, Novel glass-ceramic composition as sealant for SOFCs, Journal of the American Ceramic Society, 97 (2014) 3835-3842.
[49] J. Malzbender, Y. Zhao, T. Beck, Fracture and creep of glass–ceramic solid oxide fuel cell sealant materials, Journal of Power Sources, 246 (2014) 574-580.
[50] J.W. Fergus, Sealants for solid oxide fuel cells, Journal of Power Sources, 147 (2005) 46-57.
[51] S.M. Gross, D. Federmann, J. Remmel, M. Pap, Reinforced composite sealants for solid oxide fuel cell applications, Journal of Power Sources, 196 (2011) 7338-7342.
[52] B. Cela Greven, S.M. Gross-Barsnick, D. Federmann, R. Conradt, Strength Evaluation of Multilayer Glass–Ceramic Sealants, Fuel Cells, 13 (2013) 565-571.
[53] X. Qi, F.T. Akin, Y.S. Lin, Ceramic–glass composite high temperature seals for dense ionic-conducting ceramic membranes, Journal of Membrane Science, 193 (2001) 185-193.
[54] K.A. Nielsen, M. Solvang, S.B.L. Nielsen, A.R. Dinesen, D. Beeaff, P.H. Larsen, Glass composite seals for SOFC application, Journal of the European Ceramic Society, 27 (2007) 1817-1822.
[55] F. Smeacetto, M. Salvo, M. Ferraris, J. Cho, A.R. Boccaccini, Glass–ceramic seal to join Crofer 22 APU alloy to YSZ ceramic in planar SOFCs, Journal of the European Ceramic Society, 28 (2008) 61-68.
[56] K.S. Weil, C.A. Coyle, J.S. Hardy, J.Y. Kim, G.-G. Xia, Alternative planar SOFC sealing concepts, Fuel Cells Bulletin, 2004 (2004) 11-16.
[57] I.W. Donald, Preparation, properties and chemistry of glass-ceramic-to-metal and glass-ceramic-to-metal seals and coatings, J Mater Sci, 28 (1993) 2841-2886.

[58] K.S. Weil, The state-of-the-art in sealing technology for solid oxide fuel cells, Jom-Us, 58 (2006) 37-44.
[59] P.A. Lessing, A review of sealing technologies applicable to solid oxide electrolysis cells, J Mater Sci, 42 (2007) 3465-3476.
[60] K. Kokini, R.W. Perkins, Thermal-stresses in annular glass-to-metal seals under thermal-shock, AIAA Journal, 22 (1984) 1472-1477.
[61] J. Laurencin, B. Morel, Y. Bultel, F. Lefebvre-Joud, Thermo-Mechanical Model of Solid Oxide Fuel Cell Fed with Methane, Fuel Cells, 6 (2006) 64-70.
[62] I. Dlouhy, M. Reinisch, A.R. Boccaccini, J.F. Knott, Fracture characteristics of borosilicate glasses reinforced by metallic particles, Fatigue & Fracture of Engineering Materials & Structures, 20 (1997) 1235-1253.
[63] P. Geasee, T. Schwickert, U. Diekmann, R. Conradt, Glasses from the System RO-R2O3-SiO2 As Sealants of High Chromium Steel Components in the Planar SOFC, in: Ceramic Materials and Components for Engines, Wiley-VCH Verlag GmbH, 2007, pp. 57-62.
[64] S.M. Gross, T. Koppitz, J. Remmel, J.-B. Bouche, U. Reisgen, Joining properties of a composite glass-ceramic sealant, Fuel Cells Bulletin, 2006 (2006) 12-15.
[65] Y. Zhao, Y. Zhao, Thermo-mechanical properties of glass-ceramic solid oxide fuel cell sealant materials, in, RWTH Aachen, 2013.
[66] K.S. Eichler, G.; Otschik, P. ; Schafferath, W., BAS ($BaO.Al_2O_3.SiO_2$)-glasses for high temperature applications, Elsevier, Kidlington, ROYAUME-UNI, 1999.
[67] K.D. Meinhardt, J.D. Vienna, T.R. Armstrong, L.R. Pederson, Glass-ceramic material and method of making, in, Google Patents, 2002.
[68] Y.-S. Chou, E.C. Thomsen, J.P. Choi, J.W. Stevenson, Compliant alkali silicate sealing glass for solid oxide fuel cell applications: The effect of protective YSZ coating on electrical stability in dual environment, Journal of Power Sources, 202 (2012) 149-156.
[69] M.K. Mahapatra, K. Lu, Seal glass for solid oxide fuel cells, Journal of Power Sources, 195 (2010) 7129-7139.
[70] H. Scholze, Glass, Springer-Verlag New York, 1991.
[71] M. Bram, S. Reckers, P. Drinovac, J. Moench, R.W. Steinbrech, Characterisation and evaluation of compression loaded sealing concepts for SOFC stacks, Electrochemical Society, Pennington, NJ, ETATS-UNIS, 2003.
[72] J. Duquette, A. Petric, Silver wire seal design for planar solid oxide fuel cell stack, Journal of Power Sources, 137 (2004) 71-75.
[73] M. Bram, S. Reckers, P. Drinovac, J. Mönch, R.W. Steinbrech, H.P. Buchkremer, D. Stöver, Deformation behavior and leakage tests of alternate sealing materials for SOFC stacks, Journal of Power Sources, 138 (2004) 111-119.
[74] S.P. Simner, J.W. Stevenson, Compressive mica seals for SOFC applications, Journal of Power Sources, 102 (2001) 310-316.
[75] Y.-S. Chou, J.W. Stevenson, L.A. Chick, Ultra-low leak rate of hybrid compressive mica seals for solid oxide fuel cells, Journal of Power Sources, 112 (2002) 130-136.
[76] Y.-S. Chou, J.W. Stevenson, Phlogopite mica-based compressive seals for solid oxide fuel cells: effect of mica thickness, Journal of Power Sources, 124 (2003) 473-478.
[77] Y.-S. Chou, J.W. Stevenson, Mid-term stability of novel mica-based compressive seals for solid oxide fuel cells, Journal of Power Sources, 115 (2003) 274-278.
[78] B.C. Greven, Glass-Ceramic Sealant Reinforcementfor High-Temperature Applications, in, RWTH Aachen University, 2015.

[79] G. Quinn, Strength and Proof Testing, ASM International, Engineered Materials Handbook, 1991.

[80] J.W. Hutchinson, Mechanisms of toughening in ceramics, IUTAM, 1989.

[81] P. Lipetzky, Z. Knesl, Crack-particle interaction in a two-phase composite Part II: crack deflection, International Journal of Fracture, 73 (1995) 81-92.

[82] Y. Zhao, J. Malzbender, Elevated temperature effects on the mechanical properties of solid oxide fuel cell sealing materials, Journal of Power Sources, 239 (2013) 500-504.

[83] Y. Zhao, J. Malzbender, S.M. Gross, The effect of room temperature and high temperature exposure on the elastic modulus, hardness and fracture toughness of glass ceramic sealants for solid oxide fuel cells, Journal of the European Ceramic Society, 31 (2011) 541-548.

[84] L. Blum, S.M. Groß, J. Malzbender, U. Pabst, M. Peksen, R. Peters, I.C. Vinke, Investigation of solid oxide fuel cell sealing behavior under stack relevant conditions at Forschungszentrum Jülich, Journal of Power Sources, 196 (2011) 7175-7181.

[85] N. Lahl, K. Singh, L. Singheiser, K. Hilpert, D. Bahadur, Crystallisation kinetics in AO-Al_2O_3-SiO_2-B_2O_3 glasses (A = Ba, Ca, Mg), J Mater Sci, 35 3089-3096.

[86] J. Wei, G. Pecanac, J. Malzbender, Review of mechanical characterization methods for ceramics used in energy technologies, Ceramics International, 40 (2014) 15371-15380.

[87] F. Smeacetto, A. De Miranda, A. Ventrella, M. Salvo, M. Ferraris, Shear strength tests of glass ceramic sealant for solid oxide fuel cells applications, Advances in Applied Ceramics, 114 (2015) S70-S75.

[88] J. Malzbender, R.W. Steinbrech, Advanced measurement techniques to characterize thermo-mechanical aspects of solid oxide fuel cells, Journal of Power Sources, 173 (2007) 60-67.

[89] S. Baumann, W.A. Meulenberg, H.P. Buchkremer, Manufacturing strategies for asymmetric ceramic membranes for efficient separation of oxygen from air, Journal of the European Ceramic Society, 33 (2013) 1251-1261.

[90] P.V. Hendriksen, J.R. Høgsberg, A.M. Kjeldsen, B.F. Sørensen, H.G. Pedersen, Failure Modes of Thin Supported Membranes, in: Advances in Solid Oxide Fuel Cells II: Ceramic Engineering and Science Proceedings, John Wiley & Sons, Inc., 2008, pp. 347-360.

[91] W.C. Oliver, G.M. Pharr, An improved technique for determining hardness and elastic modulus using load and displacement sensing indentation experiments, Journal of Materials Research, 7 (1992) 1564-1583.

[92] J. Hay, Introduction to Instrumented Indentation Testing, Experimental Techniques, 33 (2009) 66-72.

[93] J. Malzbender, G. de With, J.M.J. den Toonder, Elastic modulus, indentation pressure and fracture toughness of hybrid coatings on glass, Thin Solid Films, 366 (2000) 139-149.

[94] Z. Chen, X. Wang, A. Atkinson, N. Brandon, Spherical indentation of porous ceramics: Elasticity and hardness, Journal of the European Ceramic Society, 36 (2016) 1435-1445.

[95] T. Klemensø, Lund, E., Sørensen, B.F, Optimal shape of thin tensile test specimen, Journal of the American Ceramic Society, 90 (2007) 1827-1835.

[96] J. Malzbender, R.W. Steinbrech, Mechanical properties of coated materials and multi-layered composites determined using bending methods, Surface and Coatings Technology, 176 (2004) 165-172.

[97] N.H. Menzler, P. Batfalsky, L. Blum, M. Bram, S.M. Gross, V.A.C. Haanappel, J. Malzbender, V. Shemet, R.W. Steinbrech, I. Vinke, Studies of material interaction after long-term stack operation, Fuel Cells, 7 (2007) 356-363.

[98] K. Bongartz, E. Gyarmati, H. Schuster, K. Täuber, The Brittle Ring Test: A method for measuring strength and young's modulus on coatings of HTR fuel particles, Journal of Nuclear Materials, 62 (1976) 123-137.
[99] K. Kwok, L. Kiesel, H.L. Frandsen, M. Søgaard, P.V. Hendriksen, Strength characterization of tubular ceramic materials by flexure of semi-cylindrical specimens, Journal of the European Ceramic Society, 34 (2014) 1423-1432.
[100] B.X. Huang, J. Malzbender, R.W. Steinbrech, L. Singheiser, Discussion of the complex thermo-mechanical behavior of Ba0.5Sr0.5Co0.8Fe0.2O3−δ, Journal of Membrane Science, 359 (2010) 80-85.
[101] G. Quinn, J. Swab, Elastic Modulus by Resonance of Rectangular Prisms: Corrections for Efge Treatments Army Research Laboratory July, 2000.
[102] M. Radovic, E. Lara-Curzio, L. Riester, Comparison of different experimental techniques for determination of elastic properties of solids, Mat Sci Eng a-Struct, 368 (2004) 56-70.
[103] T. Bause, Thermomechanische Eigenschaften und Schädigungsverhalten keramischer Werkstoffverbunde in der Hochtemperaturzelle, in, RWTH Aachen, 2012.
[104] W. Araki, H. Azuma, T. Yota, Y. Arai, J. Malzbender, Mechanical characteristics of electrolytes assessed with resonant ultrasound spectroscopy, Fuel Cells, 13 (2013) 542-548.
[105] A. Selçuk, A. Atkinson, Elastic properties of ceramic oxides used in solid oxide fuel cells (SOFC), Journal of the European Ceramic Society, 17 (1997) 1523-1532.
[106] R.E. Fryxell, B.A. Chandler, Creep, strength, expansion, and elastic moduli of sintered BeO as a function of grain size, porosity, and grain orientation, Journal of the American Ceramic Society, 47 (1964) 283-291.
[107] R.M. Spriggs, Expression for effect of porosity on elastic modulus of polycrystalline refractory materials, particularly aluminum oxide, Journal of the American Ceramic Society, 44 (1961) 628-629.
[108] D.P.H. Hasselman, On the porosity dependence of the elastic moduli of polycrystalline refractory materials, Journal of the American Ceramic Society, 45 (1962) 452-453.
[109] Z. Hashin, S. Shtrikman, A variational approach to the theory of the elastic behaviour of multiphase materials, Journal of the Mechanics and Physics of Solids, 11 (1963) 127-140.
[110] B. Budiansky, On the elastic moduli of some heterogeneous materials, Journal of the Mechanics and Physics of Solids, 13 (1965) 223-227.
[111] Z. Hashin, The elastic moduli of heterogeneous materials, Journal of Applied Mechanics, 29 (1962) 143-150.
[112] N. Ramakrishnan, V.S. Arunachalam, Effective Elastic-Moduli of Porous Solids, J Mater Sci, 25 (1990) 3930-3937.
[113] N. Ramakrishnan, V.S. Arunachalam, Effective elastic moduli of porous ceramic materials, Journal of the American Ceramic Society, 76 (1993) 2745-2752.
[114] K.K. Phani, S.K. Niyogi, Young's modulus of porous brittle solids, J Mater Sci, 22 (1987) 257-263.
[115] A. Nakajo, C. Stiller, G. Härkegård, O. Bolland, Modeling of thermal stresses and probability of survival of tubular SOFC, Journal of Power Sources, 158 (2006) 287-294.
[116] A. Faes, H.L. Frandsen, A. Kaiser, M. Pihlatie, Strength of anode-supported solid oxide fuel cells, Fuel Cells, 11 (2011) 682-689.
[117] R. Danzer, W. Harrer, P. Supancic, T. Lube, Z. Wang, A. Börger, The ball on three balls test—Strength and failure analysis of different materials, Journal of the European Ceramic Society, 27 (2007) 1481-1485.

[118] J. Wei, G. Pećanac, J. Malzbender, Mechanical behavior of silver reinforced glass–ceramic sealants for solid oxide fuel cells, Ceramics International, 41 (2015) 15122-15127.
[119] C.A. Klein, Characteristic strength, Weibull modulus, and failure probability of fused silica glass, OPTICE, 48 (2009) 113401.
[120] B. Kuhn, Bruchmechanische Untersuchung von Metall, in: Keramik-Verbundsystemen für die Anwendung in der Hochtemperatur-Brennstoffzelle, RWTH Aachen, 2009.
[121] M. Ferraris, M. Salvo, S. Rizzo, V. Casalegno, S.H. Han, A. Ventrella, T. Hinoki, Y. Katoh, Torsional shear strength of silicon carbide components pressurelessly joined by a glass-ceramic, International Journal of Applied Ceramic Technology, 9 (2012) 786-794.
[122] M. Ferraris, A. Ventrella, M. Salvo, M. Avalle, F. Pavia, E. Martin, Comparison of shear strength tests on AV119 epoxy-joined carbon/carbon composites, Composites Part B: Engineering, 41 (2010) 182-191.
[123] M. Ferraris, A. Ventrella, M. Salvo, Y. Katoh, D. Gross, Torsional shear strength tests for glass-ceramic joined silicon carbide, International Journal of Applied Ceramic Technology, 12 (2015) 693-699.
[124] T. Schwickert, Fügen von Hochtemperatur-Brennstoffzellen, in, RWTH Aachen, RWTH Aachen 2002.
[125] J. Malzbender, J. Monch, R.W. Steinbrech, T. Koppitz, S.M. Gross, J. Remmel, Symmetric shear test of glass-ceramic sealants at SOFC operation temperature, J Mater Sci, 42 (2007) 6297-6301.
[126] G.A. Gogotsi, Fracture toughness of ceramics and ceramic composites, Ceramics International, 29 (2003) 777-784.
[127] G.D. Quinn, Fracture toughness of advanced ceramics at room temperature: a vamas round robin, in: Proceedings of the 17th Annual Conference on Composites and Advanced Ceramic Materials: Ceramic Engineering and Science Proceedings, John Wiley & Sons, Inc., 2008, pp. 92-100.
[128] D. Roylance, Introduction to fracture mechanics, in, Department of Materials Science and Engineering, Massachusetts Institute of Technology, Cambridge, 2001.
[129] G. Quinn, Measring fracture toughness, in: ACerS Course, Daytona US Jan. 2015.
[130] S.W. Freiman, Environmentally enhanced fracture of ceramics, MRS Proceedings, 125 (2011).
[131] G.R. Anstis, P. Chantikul, B.R. Lawn, D.B. Marshall, A critical evaluation of indentation techniques for measuring fracture toughness: Direct crack measurements, Journal of the American Ceramic Society, 64 (1981) 533-538.
[132] B.X. Huang, V. Vasechko, Q.L. Ma, J. Malzbender, Thermo-mechanical properties of (Sr,Y)TiO_3 as anode material for solid oxide fuel cells, Journal of Power Sources, 206 (2012) 204-209.
[133] Z. Chen, X. Wang, V. Bhakhri, F. Giuliani, A. Atkinson, Nanoindentation of porous bulk and thin films of $La_{0.6}Sr_{0.4}Co_{0.2}Fe_{0.8}O_{3-\delta}$, Acta Materialia, 61 (2013) 5720-5734.
[134] A. Atkinson, P. Bastid, Q.Y. Liu, Mechanical properties of magnesia-spinel composites, Journal of the American Ceramic Society, 90 (2007) 2489-2496.
[135] A. Chanda, B.X. Huang, J. Malzbender, R.W. Steinbrech, Micro- and macro-indentation behaviour of $Ba_{0.5}Sr_{0.5}Co_{0.8}Fe_{0.2}O_{3-d}$ perovskite, Journal of the European Ceramic Society, 31 (2011) 401-408.
[136] J. Malzbender, Y.L. Zhao, Micromechanical testing of glass-ceramic sealants for solid oxide fuel cells, J Mater Sci, 47 (2012) 4342-4347.

[137] M. Radovic, E. Lara-Curzio, Mechanical properties of tape cast nickel-based anode materials for solid oxide fuel cells before and after reduction in hydrogen, Acta Materialia, 52 (2004) 5747-5756.

[138] S. Goutianos, H.L. Frandsen, B.F. Sørensen, Fracture properties of nickel-based anodes for solid oxide fuel cells, Journal of the European Ceramic Society, 30 (2010) 3173-3179.

[139] L.J. Vandeperre, X. Wang, A. Atkinson, Measurement of mechanical properties using slender cantilever beams, Journal of the European Ceramic Society, 36 (2016) 2003-2007.

[140] J. Laurencin, G. Delette, F. Usseglio-Viretta, S. Di Iorio, Creep behaviour of porous SOFC electrodes: Measurement and application to Ni-8YSZ cermets, Journal of the European Ceramic Society, 31 (2011) 1741-1752.

[141] Creep deformation in: U.o. Cambridge (Ed.), University of Cambridge, TLP Library, 2004-2015.

[142] G. Pećanac, S. Baumann, J. Malzbender, Mechanical properties and lifetime predictions for $Ba_{0.5}Sr_{0.5}Co_{0.8}Fe_{0.2}O_{3-\delta}$ membrane material, Journal of Membrane Science, 385-386 (2011) 263-268.

[143] D.J. Green, An introduction to the mechanical properties of ceramics, Cambridge University Press, 1998.

[144] C. Herring, Diffusional viscosity of a polycrystalline solid, Journal of Applied Physics, 21 (1950) 437-445.

[145] R.L. Coble, A model for boundary diffusion controlled creep in polycrystalline materials, Journal of Applied Physics, 34 (1963) 1679-1682.

[146] D.S. Wilkinson, Creep mechanisms in multiphase ceramic materials, Journal of the American Ceramic Society, 81 (1998) 275-299.

[147] M.W. Barsoum, Fundamentals of ceramics, McGraw-Hill Inc.,US, 1997, 1997.

[148] H.J. Frost, M.F. Ashby, Deformation-mechanism maps : the plasticity and creep of metals and ceramics, Pergamon Press, Oxford; New York, 1982.

[149] F.H. Norton, The creep of steel at high temperature, New York [etc.] McGraw-Hill book company, inc., 1929.

[150] A.H. Chokshi, Diffusion creep in oxide ceramics, Journal of the European Ceramic Society, 22 (2002) 2469-2478.

[151] J.X. Yi, H.L. Lein, T. Grande, S. Yakovlev, H.J.M. Bouwmeester, High-temperature compressive creep behaviour of the perovskite-type oxide $Ba_{0.5}Sr_{0.5}Co_{0.8}Fe_{0.2}O_{3-d}$, Solid State Ionics, 180 (2009) 1564-1568.

[152] B. Rutkowski, J. Malzbender, T. Beck, R.W. Steinbrech, L. Singheiser, Creep behaviour of tubular $Ba_{0.5}Sr_{0.5}Co_{0.8}Fe_{0.2}O_{3-\delta}$ gas separation membranes, Journal of the European Ceramic Society, 31 (2011) 493-499.

[153] K. Jakus, S.M. Wiederhorn, Creep deformation of ceramics in four-point bending, Journal of the American Ceramic Society, 71 (1988) 832-836.

[154] G.W. Hollenberg, G.R. Terwilliger, R.S. Gordon, Calculation of Stresses and Strains in Four-Point Bending Creep Tests, Journal of the American Ceramic Society, 54 (1971) 196-199.

[155] K.U. Snowden, E.G. Mehrtens, The calculation of the relaxed creep strain in four-point bending tests, Journal of Materials Science Letters, 16 (1997) 278-280.

[156] K.U. Snowden, E.G. Mehrtens, The calculation of the relaxed creep strain in four-point bending tests, Journal of Materials Science Letters, 16 (1997) 278-280.

[157] P.K. Talty, R.A. Dirks, Determination of tensile and compressive creep behavior of ceramic materials from bend tests, J Mater Sci, 13 (1978) 580-586.

[158] F.F. Lange, Non-elastic deformation of polycrystals with a liquid boundary phase, in: R.C. Bradt, R.E. Tressler (Eds.) Deformation of Ceramic Materials, Springer US, 1975, pp. 361-381.

[159] J.D. French, J.H. Zhao, M.P. Harmer, H.M. Chan, G.A. Miller, Creep of duplex microstructures, Journal of the American Ceramic Society, 77 (1994) 2857-2865.

[160] R.W. Rice, Evaluation and extension of physical property-porosity models based on minimum solid area, J Mater Sci, 31 (1996) 102-118.

[161] E.W. Andrews, L.J. Gibson, M.F. Ashby, The creep of cellular solids, Acta Materialia, 47 (1999) 2853-2863.

[162] R. Mueller, S. Soubielle, R. Goodall, F. Diologent, A. Mortensen, On the steady-state creep of microcellular metals, Scripta Materialia, 57 (2007) 33-36.

[163] K. Kwok, D. Boccaccini, A.H. Persson, H.L. Frandsen, Homogenization of steady-state creep of porous metals using three-dimensional microstructural reconstructions, International Journal of Solids and Structures, 78-79 (2016) 38-46.

[164] A. Atkinson, A. Selçuk, Mechanical behaviour of ceramic oxygen ion-conducting membranes, Solid State Ionics, 134 (2000) 59-66.

[165] S. Giraud, J. Canel, Young's modulus of some SOFCs materials as a function of temperature, Journal of the European Ceramic Society, 28 (2008) 77-83.

[166] M. Shimada, K.i. Matsushita, S. Kuratani, T. Okamoto, M. Koizumi, K. Tsukuma, T. Tsukidate, Temperature dependence of young's modulus and internal friction in alumina, silicon nitride, and partially stabilized zirconia ceramics, Journal of the American Ceramic Society, 67 (1984) 23-24.

[167] X. Zhao, F. Wang, Elastoplastic properties of solid oxide fuel cell before and after reduction, Acta Metallurgica Sinica (English Letters), 26 (2013) 137-142.

[168] M. Pihlatie, A. Kaiser, M. Mogensen, Mechanical properties of NiO/Ni–YSZ composites depending on temperature, porosity and redox cycling, Journal of the European Ceramic Society, 29 (2009) 1657-1664.

[169] M. Radovic, E. Lara-Curzio, Elastic properties of nickel-based anodes for solid oxide fuel cells as a function of the fraction of reduced NiO, Journal of the American Ceramic Society, 87 (2004) 2242-2246.

[170] J.J. Roa, M.A. Laguna-Bercero, A. Larrea, V.M. Orera, M. Segarra, Mechanical properties of highly textured porous Ni–YSZ and Co–YSZ cermets produced from directionally solidified eutectics, Ceramics International, 37 (2011) 3123-3131.

[171] Z. Chen, X. Wang, F. Giuliani, A. Atkinson, Microstructural characteristics and elastic modulus of porous solids, Acta Materialia, 89 (2015) 268-277.

[172] Z. Xiang, W. Fenghui, H. Jianye, L. Tiejun, Determining the mechanical properties of solid oxide fuel cell by an improved work of indentation approach, Journal of Power Sources, 201 (2012) 231-235.

[173] A. Selcuk, A. Atkinson, Strength and toughness of tape-cast yttria-stabilized zirconia, Journal of the American Ceramic Society, 83 (2000) 2029-2035.

[174] T.W. Duangmanee, S; , Electrical property of thick film electrolyte for solid oxide fuel cell Journal of Metals, Materials and Minerals, 18 (2008) 7-11.

[175] J. Chevalier, L. Gremillard, A.V. Virkar, D.R. Clarke, The tetragonal-monoclinic transformation in zirconia: lessons learned and future trends, Journal of the American Ceramic Society, 92 (2009) 1901-1920.

[176] N. Christiansen, S. Primdahl, M. Wandel, S. Ramousse, A. Hagen, Status of the solid oxide fuel cell development at Topsoe Fuel Cell A/S and DTU energy conversion, Solid Oxide Fuel Cells 13 (Sofc-Xiii), 57 (2013) 43-52.
[177] A.H. Heuer, Transformation toughening in ZrO_2-containing ceramics, Journal of the American Ceramic Society, 70 (1987) 689-698.
[178] R.H.J. Hannink, P.M. Kelly, B.C. Muddle, Transformation toughening in zirconia-containing ceramics, Journal of the American Ceramic Society, 83 (2000) 461-487.
[179] J. Alcalá, M. Anglada, High-temperature crack growth in Y-TZP, Materials Science and Engineering: A, 232 (1997) 103-109.
[180] A. Morales-Rodríguez, A. Bravo-León, A. Domínguez-Rodríguez, S. López-Esteban, J.S. Moya, M. Jiménez-Melendo, High-temperature mechanical properties of zirconia/nickel composites, Journal of the European Ceramic Society, 23 (2003) 2849-2856.
[181] T.G. Langdon, Dependence of creep rate on porosity, Journal of the American Ceramic Society, 55 (1972) 630-631.
[182] R. MacCrone, Properties and microstructure: Treatise on materials science and technology, Elsevier, 2013.
[183] H.-T. Chang, C.-K. Lin, C.-K. Liu, S.-H. Wu, High-temperature mechanical properties of a solid oxide fuel cell glass sealant in sintered forms, Journal of Power Sources, 196 (2011) 3583-3591.
[184] H.-T. Chang, C.-K. Lin, C.-K. Liu, Effects of crystallization on the high-temperature mechanical properties of a glass sealant for solid oxide fuel cell, Journal of Power Sources, 195 (2010) 3159-3165.
[185] E.V. Stephens, J.S. Vetrano, B.J. Koeppel, Y. Chou, X. Sun, M.A. Khaleel, Experimental characterization of glass–ceramic seal properties and their constitutive implementation in solid oxide fuel cell stack models, Journal of Power Sources, 193 (2009) 625-631.
[186] K.A. Nielsen, M. Solvang, S.B.L. Nielsen, D. Beeaff, Mechanical behaviour of glassy composite seals for IT-SOFC application, in: Ceramic Engineering and Science Proceedings, 2007, pp. 315-323.
[187] K. Schneider, B. Lauke, W. Beckert, Compression shear test (CST) - A convenient apparatus for the estimation of apparent sheer strength of composite materials, Applied Composite Materials, 8 (2001) 43-62.
[188] M.R. Ayatollahi, M.R.M. Aliha, Fracture analysis of some ceramics under mixed mode loading, Journal of the American Ceramic Society, 94 (2011) 561-569.
[189] F. Smeacetto, A. De Miranda, A. Ventrella, M. Salvo, M. Ferraris, Shear strength tests of glass ceramic sealant for solid oxide fuel cells applications, Advances in Applied Ceramics, 114 (2015) S70-S75.
[190] C.-K. Lin, J.-Y. Chen, J.-W. Tian, L.-K. Chiang, S.-H. Wu, Joint strength of a solid oxide fuel cell glass–ceramic sealant with metallic interconnect, Journal of Power Sources, 205 (2012) 307-317.
[191] N. Christiansen, S. Primdahl, M. Wandel, S. Ramousse, A. Hagen, Status of the solid oxide fuel cell development at Topsoe fuel cell A/S and DTU energy conversion, in: ECS Transactions, 2013, pp. 43-52.
[192] S.M. Gross, T. Koppitz, J. Remmel, U. Reisgen, Glass-ceramic materials of the system $BaO\text{-}CaO\text{-}SiO_2$ as sealants for SOFC applications, in: Advances in Solid Oxide Fuel Cells: Ceramic Engineering and Science Proceedings, John Wiley & Sons, Inc., 2008, pp. 239-245.

[193] A. Shyam, E. Lara-Curzio, The double-torsion testing technique for determination of fracture toughness and slow crack growth behavior of materials: A review, J Mater Sci, 41 (2006) 4093-4104.
[194] S.M. Wiederhorn, B.J. Hockey, J.D. French, Mechanisms of deformation of silicon nitride and silicon carbide at high temperatures, Journal of the European Ceramic Society, 19 (1999) 2273-2284.
[195] F. Fleischhauer, R. Bermejo, R. Danzer, A. Mai, T. Graule, J. Kuebler, Strength of an electrolyte supported solid oxide fuel cell, Journal of Power Sources, 297 (2015) 158-167.
[196] P.M. Delaforce, J.A. Yeomans, N.C. Filkin, G.J. Wright, R.C. Thomson, Effect of NiO on the phase stability and microstructure of yttria-stabilized zirconia, Journal of the American Ceramic Society, 90 (2007) 918-924.
[197] M. Radovic, E. Lara-Curzio, G. Nelson, Fracture toughness and slow crack growth behavior of Ni-YSZ and YSZ as a function of porosity and temperature, in: Advances in Solid Oxide Fuel Cells II: Ceramic Engineering and Science Proceedings, John Wiley & Sons, Inc., 2008, pp. 373-381.
[198] K.S. Chan, A Grain Boundary Fracture Model for Predicting Dynamic Embrittlement and Oxidation-Induced Cracking in Superalloys, Metall Mater Trans A, 46 (2015) 2491-2505.
[199] L.J. Liang, K. Li, D. Yan, B. Ma, J.J. Yang, J. Pu, B. Chi, J. Li, Mechanical Property and Deformation Behavior of SOFCs, Journal of Inorganic Materials, 30 (2015) 633-638.
[200] J.P. Malzbender, G; Baumann, S;, Slow crack growth and creep rupture of $Ba_{0.5}Sr_{0.5}Co_{0.8}Fe_{0.2}O_{3-\delta}$, Key Engineering Materials, 488-489 (2011) 303-306
[201] R.W. Rice, Porosity of Ceramics: Properties and Applications, CRC Press, 1998.
[202] A.H. Chokshi, Diffusion creep in oxide ceramics, Journal of the European Ceramic Society, 22 (2002) 2469-2478.
[203] R. Soltani, T.W. Coyle, J. Mostaghimi, Creep Behavior of Plasma-Sprayed Zirconia Thermal Barrier Coatings, Journal of the American Ceramic Society, 90 (2007) 2873-2878.
[204] S. Kats, S. Ordan'yan, A. Gorin, L. Kudryasheva, Effect of porosity on the creep of niobium carbide and other materials during monoaxial loading, Strength of Materials, 5 (1973) 858-862.
[205] E. Withey, C. Petorak, R. Trice, G. Dickinson, T. Taylor, Design of 7 wt.% Y2O3–ZrO2/mullite plasma-sprayed composite coatings for increased creep resistance, Journal of the European Ceramic Society, 27 (2007) 4675-4683.
[206] R.M. Spriggs, T. Vasilos, Functional relation between creep rate and porosity for polycrystalline ceramics, Journal of the American Ceramic Society, 47 (1964) 47-48.

Acknowledgement

I would like to thank Univ.-Prof. Dr.-Ing. L. Singheiser for providing the great conditions and opportunity to work at the IEK-2 Institute at Forschungszentrum Jülich GmbH. I am also very grateful to his supervision and support of my thesis. Also many thanks for Univ.-Prof. Dr.-Ing. T. Beck for the support on the thesis.

The deep and sincere appreciation goes to Dr. J. Malzbender for his excellent scientific support during the whole PhD work, who has been invaluable on academic level. My honest gratitude and special thanks are for Dr. G. Pećanac, who kindly provides the excellent support and help all the time. It was very nice to work with him.

Furthermore, I would like to thank all partners from the PROSOFC project for an encouraging project work, especially Dr. M. Hauth for the excellent project management, and Dr. H. L. Frandsen and Dr. K. Kwok for the scientific discussion, and Prof. A. Atkinson for the research stay at Imperial College London, which is a valuable chance for me to get insight into the novel micromechanical analysis methods.

Many thanks to the colleges at IEK-1 for the supply of anode materials, in particular for Dr. N.H. Menzler and Dr. W. Herzhof as well as Mr. S. Primdahl from TOFC for supplying their anode materials. For sealant development and specimen preparation, I would like to specially thank to Dr. S. M. Groß-Barsnick and Dr. D. Federmann.

T. Osipova, J. Mönch and R. Küppers are kindly acknowledged for their experimental support, Dr. E. Wessel and Dr. D. Grüner for SEM studies, J. Bartsch and V. Gutzeit for their assistance in metallographic preparations, and Mrs. M. Offermann and P. Joecken for their technical support. Also special thanks for the all partners from PROSOFC. I would like also to pass the thanks to my colleagues from the working group.

Above all, very special thanks to my parents, who always support and love me.

Appendix

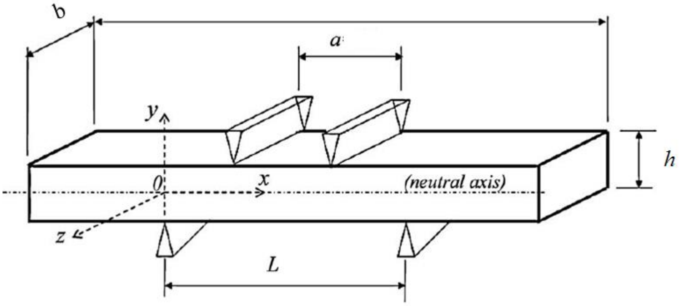

Figure 0-1: The schematic of 4-point bending test for creep.

When applied for the bending creep test, the power law model leads to the following expression for the stress σ_x at a distance ξ of the neutral axis ($\xi = -y$ in ***Figure 0-1***)

$$\sigma_x(\xi) = \frac{\xi^{1/n} \times M_f}{I_n} \qquad (A1)$$

With

$$I = 2b \times \frac{n}{2n+1} \times \left(\frac{h}{2}\right)^{(2n+1)/n} \qquad (A2)$$

where M_f is the bending moment and I_n is the complex moment of inertia that depends on the beam width *b*, thickness *h* and stress exponent *n*.

For the stationary regime, the shape of the deflected beam depends of the applied loading *F=2P* could be expressed to the following equations:

$$y(x) = -J(t) \times \left(\frac{P}{I_n}\right) \times \Gamma(x) \quad for\ x \in \left[\frac{L-a}{2}, \frac{L+a}{2}\right] \qquad (A3)$$

Where the Γ is a function which depends on the stress exponent n and the spacing between the inner and outer bearings a and L:

$$\Gamma(x) = \left(\frac{L-a}{2}\right)^n \times \left[\left(-\frac{x^2}{2} + \frac{L}{2}x\right) + \frac{L-a}{2} \times \left(\frac{n(a-L)}{4(n+2)}\right)\right] \qquad (A4)$$

The term $J(t)$ contains the time-dependence on strain and is expressed from the power law creep model:

$$J(t) = A \times t + constant\ C \qquad \text{For plane stress} \qquad (A5a)$$

$$J(t) = A \times \left(\frac{3}{4}\right)^{(n+1)/2} t + constant\ C \qquad \text{For plane strain} \qquad (A5b)$$

where $A = B \times e^{-Q/RT}$

Consider the maximum deflection point ($\boldsymbol{x = \frac{L}{2}, y = -\frac{h}{2}}$),

Insert equations ***(A4) (A5)*** into equation ***(A3)***, the equation at maximum deflection point turns into

$$y = [A \cdot t + C] \cdot \left[\frac{P}{I_n}\right]^n \cdot \Gamma\left(\frac{L}{2}\right) \qquad (A6a)$$

$$y = \left[A \cdot \left(\frac{3}{4}\right)^{(n+1)/2} \cdot t + C\right] \cdot \left[\frac{P}{I_n}\right]^n \cdot \Gamma\left(\frac{L}{2}\right) \qquad (A6b)$$

With

$$\Gamma\left(\frac{L}{2}\right) = \left(\frac{L-a}{2}\right)^n \cdot \left[\frac{L^2}{8} + \frac{L-a}{2} \cdot \left(\frac{n(a-L)}{4(n+2)}\right)\right] \qquad (A7)$$

Deflection rate can be derived from equation ***(A6)***:

$$\frac{\partial y}{\partial t} = A \cdot \left[\frac{P}{I_n}\right]^n \cdot \Gamma\left(\frac{L}{2}\right) = P^n \cdot H \qquad (A8a)$$

$$\frac{\partial y}{\partial t} = A \cdot \left(\frac{3}{4}\right)^{(n+1)/2} \cdot \left[\frac{P}{I_n}\right]^n \cdot \Gamma\left(\frac{L}{2}\right) = P^n \cdot H \qquad (A8b)$$

With

$$H = A \cdot \frac{\Gamma\left(\frac{L}{2}\right)}{I_n} \qquad (A9a)$$

$$H = A \cdot \frac{\Gamma\left(\frac{L}{2}\right)}{I_n} \left(\frac{3}{4}\right)^{(n+1)/2} \qquad (A9b)$$

Make the equation ***(A8)*** into logarithmic expression:

$$\ln \frac{\partial y}{\partial t} = n \cdot \ln P + \ln H \qquad (A10)$$

List of figures

List of tables

Band / Volume 378
Dissolution Behaviour of Innovative Inert Matrix Fuels for Recycling of Minor Actinides
E. L. Mühr-Ebert (2017), xii, 164 pp
ISBN: 978-3-95806-238-2

Band / Volume 379
Charakterisierung und Modifizierung von Kupferoxid- und Kupfersulfid-Nanopartikeln für Dünnschichtsolarzellen
J. Flohre (2017), 141, iii pp
ISBN: 978-3-95806-241-2

Band / Volume 380
Einzelfaserkomposite aus Pulvermetallurgischem Wolfram-faserverstärktem Wolfram
B. Jasper (2017), v, 92, XVIII pp
ISBN: 978-3-95806-248-1

Band / Volume 381
Untersuchungen zur Deckschichtbildung auf $LiNi_{0,5}Mn_{1,5}O_4$-Hochvoltkathoden
Die Kathoden/Elektrolyt-Grenzfläche in Hochvolt-Lithium-Ionen-Batterien
K. Wedlich (2017), xvi, 157, xvii-xxvi pp
ISBN: 978-3-95806-249-8

Band / Volume 382
Charakterisierung gradierter Eisen/Wolfram-Schichten für die erste Wand von Fusionsreaktoren
S. Heuer (2017), x, 234 pp
ISBN: 978-3-95806-252-8

Band / Volume 383
High resolution imaging and modeling of aquifer structure
N. Güting (2017), viii, 107 pp
ISBN: 978-3-95806-253-5

Band / Volume 384
IEK-3 Report 2017
Sektorkopplung –
Forschung für ein integriertes Energiesystem
(2017), 182 pp
ISBN: 978-3-95806-256-6

Band / Volume 385
Bestimmung der Wolframerosion mittels optischer Spektroskopie unter ITER-relevanten Plasmabedingungen
M. Laengner (2017), vi, 184, XI pp
ISBN: 978-3-95806-257-3

Band / Volume 386
IEK-3 Report 2017
Sector Coupling –
Research for an Integrated Energy System
(2017), 175 pp
ISBN: 978-3-95806-258-0

Band / Volume 387
Photochemistry of Highly Oxidized Multifunctional Organic Molecules: a Chamber Study
L. I. M. Pullinen (2017), II, 96, xviii pp
ISBN: 978-3-95806-260-3

Band / Volume 388
Poröse Transportschichten für die Polymerelektrolytmembran-Wasserelektrolyse
M. Höh (2017), VI, 186 pp
ISBN: 978-3-95806-262-7

Band / Volume 389
Modelling of High Temperature Polymer Electrolyte Fuel Cells
Q. Cao (2017), 173 pp
ISBN: 978-3-95806-263-4

Band / Volume 390
Potential use of nitrification inhibitors for mitigating N_2O emission from soils
D. Wu (2017), 206 pp
ISBN: 978-3-95806-264-1

Band / Volume 391
Mechanical Characterization of Solid Oxide Fuel Cells and Sealants
J. Wei (2017), II, 151 pp
ISBN: 978-3-95806-266-5

Weitere ***Schriften des Verlags im Forschungszentrum Jülich*** unter
http://wwwzb1.fz-juelich.de/verlagextern1/index.asp

Energie & Umwelt / Energy & Environment
Band / Volume 391
ISBN 978-3-95806-266-5